Head Office: Università degli Studi di Padova

Department of: Agronomy, Food, Natural Resources, Animals and Environment (DAFNAE)

Ph.D. course in: Crop Science

Series: XXXVI

Remote sensing for the assessment of spatio-temporal variability of grassland cover and phenology

Coordinator: Prof. Massimo Faccoli

Supervisor: Prof. Michele Scotton

Co-Supervisor: Dott. Damiano Gianelle

Ph.D. student: Davide Andreatta

Declaration

I hereby declare that this submission is my own work and that, to the best of my knowledge and belief, it contains no material previously published or written by another person nor material which to a substantial extent has been accepted for the award of any other degree or diploma of the University or other institute of higher learning, except where due acknowledgment has been made in the text.

Padua, January 10th 2024

Davide Andreatta

A copy of the thesis will be available at http://paduaresearch.cab.unipd.it/

Dichiarazione

Con la presente affermo che questa tesi è frutto del mio lavoro e che, per quanto io ne sia a conoscenza, non contiene materiale precedentemente pubblicato o scritto da un'altra persona né materiale che è stato utilizzato per l'ottenimento di qualunque altro titolo o diploma dell'Università o altro istituto di apprendimento, a eccezione del caso in cui ciò venga riconosciuto nel testo.

Padova, 10 gennaio 2024

Davide Andreatta

Una copia della tesi sarà disponibile presso http://paduaresearch.cab.unipd.it/

Table of contents

Summary

Global change is impacting grasslands through multiple processes and is driving severe consequences to their structure and functioning, and to the ecosystem services they provide. The recent advancements in remote sensing imagery availability offer new opportunities to tackle the challenge of grasslands monitoring, providing unprecedented revisiting frequency on wide areas at fine spatial resolution. Unfortunately, there are still few standardized indicators available to track grassland processes, and many processes still lack a thorough understanding.

During my Ph.D., I focused on four main goals: i) assessing the grassland fractional vegetation cover prediction capability of newly available remote sensing products; ii) developing a easy to use, free, and cloud-based tool for grassland management intensity monitoring; iii) developing a workflow for grassland flowering phenology extraction using time-lapse cameras; iv) better understanding how plant phenological trends are shifting in climatically heterogenous mountain landscapes, and how this is affecting ecosystem productivity.

Our findings demonstrated that the raw spectral signature of grasslands does not exhibit a linear variation across the fractional vegetation cover gradient, and that Sentinel-2 and PlanetScope have a higher fractional vegetation cover prediction capability compared to previously available imagery, especially in areas under patchy degradation and restoration processes. We introduced a model for estimating grassland mowing frequency, which can effectively be used under different management and environmental conditions. It was validated on small and fragmented parcels compared to previous studies, and it can be run using a provided ready to use code working on a cloud platform. We presented a new workflow for grassland flowering phenology extraction of single (or group of) species from time-lapse cameras. The workflow opened new possibilities for phenological studies, overcoming laborious and time-consuming ground-based vegetation observations. In the fourth study, we revealed substantial differences in the phenological response among vegetation types and across elevations in the European mountains over the last two decades. In grasslands, spring phenology was advanced at high altitudes and delayed at low altitudes, thus becoming more uniform along the elevational gradient, while in deciduous forests we observed the opposite trend. Remote sensing data indicated that growing season length has not been the primary factor limiting productivity over the last two decades. Therefore, it is crucial to incorporate the decoupling between phenology and productivity when simulating the potential carbon uptake of terrestrial ecosystems in future climate change scenarios.

Overall, these four studies showed that remote sensing images and processing workflows can greatly contribute to a better understanding of human- and climate-induced processes impacting grassland and forest ecosystems.

Riassunto

Il cambiamento globale sta impattando le praterie attraverso molteplici processi, alterandone la struttura, il funzionamento e la capacità di erogare servizi ecosistemici. Negli ultimi decenni la disponibilità di immagini telerilevate è notevolmente aumentata, offrendo nuove opportunità per il loro monitoraggio. Le attuali immagini telerilevate, infatti, offrono una risoluzione spaziale elevata ed un tempo di rivisitazione senza precedenti su vaste aree. Nonostante ciò, sono ancora pochi gli indicatori standardizzati per il monitoraggio dei processi delle praterie e molti processi non sono ancora stati compresi a fondo.

Nel mio dottorato mi sono concentrato su quattro obiettivi principali: i) valutare la capacità di stima della copertura erbacea da parte dei nuovi prodotti satellitari; ii) sviluppare uno strumento di facile utilizzo, gratuito e in cloud per il monitoraggio dell'intensità di gestione delle praterie; iii) sviluppare un metodo per estrarre la fenologia fiorale delle praterie utilizzando immagini ricavate da fotocamere fisse; iv) comprendere meglio come cambiano le tendenze fenologiche delle piante in paesaggi montani climaticamente eterogenei e come ciò influisce sulla produttività degli ecosistemi.

Le analisi realizzate indicano che la firma spettrale delle praterie non varia linearmente lungo il gradiente di copertura erbacea e che Sentinel-2 e PlanetScope hanno una maggiore capacità di stima della copertura erbacea rispetto ai prodotti satellitari precedentemente disponibili, soprattutto nelle aree sottoposte a processi di degrado e di rivegetazione spazialmente eterogenei. Il modello per la stima della frequenza di sfalcio dei prati sviluppato ha dimostrato un'elevata accuratezza in diverse condizioni gestionali e ambientali. Il modello è stato validato su parcelle piccole e frammentate rispetto agli studi precedenti e può essere eseguito utilizzando un codice pronto all'uso su una piattaforma in cloud. È stato realizzato un nuovo flusso di lavoro per l'estrazione della fenologia fiorale di singole (o gruppi di) specie di prateria utilizzando immagini acquisite da fotocamere fisse. Il metodo proposto apre a nuove possibilità per gli studi fenologici, in quanto richiede quantità di manodopera decisamente inferiori rispetto alle osservazioni di campo. Nell'ultimo capitolo, ho presentato le differenze individuate nella risposta fenologica di praterie e foreste di latifoglie a diverse altitudini negli ultimi due decenni nelle montagne europee. Nelle praterie, la fenologia primaverile è stata anticipata ad alta quota e ritardata a bassa quota, risultando quindi più omogenea lungo il gradiente altitudinale, mentre nelle foreste di latifoglie ha mostrato una tendenza opposta. I dati satellitari analizzati indicano che la lunghezza del periodo vegetativo non è stata il principale fattore limitante per la produttività negli ultimi due decenni. È dunque necessario considerare il disaccoppiamento tra fenologia e produttività nella simulazione del potenziale assorbimento di carbonio degli ecosistemi terrestri nei futuri scenari di cambiamento climatico.

Nel complesso, questi quattro studi hanno dimostrato che le immagini satellitari e adeguati sistemi di processamento possono contribuire notevolmente a migliorare la comprensione dei processi indotti dall'uomo e dal clima sulle praterie e sulle foreste.

Introduction

Grasslands and the global change

Global change is impacting grasslands through multiple processes and is driving severe consequences for the ecosystem services they provide (Bardgett et al., 2021; Wang et al., 2019). Monitoring ongoing changes in grasslands is crucial since grasslands cover one-third of the earth's terrestrial surface and 70% of the global agricultural area (Reynolds & Frame, 2005). Over 49% of grassland area experienced degradation, defined as a persistent decline or loss in biodiversity, ecosystem functions, or ecosystem services (Gang et al., 2014; IPBES, 2018). Some of the drivers of grassland degradation are directly induced by human activities, some others are related to gradual changes in temperature and precipitation attributed to climate change (Bardgett et al., 2021). Human-induced drivers include overgrazing, eutrophication, land conversion to forest and crops, land abandonment, invasive species, and altered fire regimes (Kipling et al., 2016; Wang et al., 2019; Zarei et al., 2020). The urgency of grassland degradation monitoring and combatting stems from the fact that degraded grasslands not only contribute less to provisioning services, but also to erosion control, water purification, biodiversity conservation, cultural services, and carbon storage (Li et al., 2022). Responses of grassland carbon fluxes to climate warming can play a large role in driving changes in global carbon cycling since they store approximately one-third of the terrestrial carbon stock and their degradation can lead to significant carbon losses (Ahlström et al., 2015; Bai & Cotrufo, 2022). Changes in growing season length can be an additional driver of changes in grassland productivity (Peñuelas et al., 2009; Piao et al., 2019; Richardson et al., 2013). Since the observed phenological change affects also managed grasslands, agricultural practice timing must be adjusted (Chang et al., 2017).

Remote sensing for grassland monitoring

The recent advancements in remote sensing (RS) imagery availability offer new opportunities to monitor grasslands with unprecedented revisiting frequency on wide areas at fine spatial resolution (Reinermann et al., 2020; Ustin & Middleton, 2021; Wachendorf et al., 2018). This is crucial since standardized indicators of grassland processes are needed to monitor grassland global change (Bardgett et al., 2021). RS has been used to monitor changes in grassland structural properties like biomass and fractional vegetation cover (FVC) (Guerini Filho et al., 2020; Kim et al., 2020), in composition (Wachendorf et al., 2018), in management intensity (Reinermann et al., 2020; Schwieder et al., 2021; Weber et al., 2023), and in phenology (Dronova & Taddeo, 2022; Xie et al., 2021). The Copernicus program, managed

by the European Commission, is delivering a huge quantity of freely available RS data with the aim of helping service providers, public authorities, and other international organizations improve the quality of life for the citizens of Europe. In particular, the Sentinels missions deliver radar and multispectral imaging for land monitoring at unprecedented spatial, temporal, and spectral resolution (Schiavon et al., 2021). Furthermore, a recent development involves private entities entering the RS sector, such as PlanetScope (PS), thereby enhancing the accessibility of timely and accurate imagery for vegetation monitoring.

Knowledge gaps and research objectives

We identified four knowledge gaps in previous literature regarding grassland monitoring using RS. With respect to grassland structural properties, the grassland FVC prediction capability of newly available RS products (PS and Sentinel-2 (S2)) has never been assessed and compared to previously available imagery at lower spatial and temporal resolution like Landsat-8. Regarding grassland management intensity, despite the existence of algorithms that can estimate mowing frequency using S2 data, there is a lack of freely accessible tools that utilize the computing capabilities offered by Google Earth Engine (GEE, Gorelick et al., 2017). Moreover, there is no available method leveraging the improved S2 cloud masking and specifically designed for fragmented landscape typical of mountain regions. Although a wide literature and tools for grassland vegetative phenology monitoring using RS are available, only a few studies tried to monitor grassland flowering phenology. PhenoCams (PCs), i.e., digital cameras configured to capture timelapse images, are relatively cheap and can provide low-cost information at the proper temporal and spatial resolution, but no method to extract grassland flowering phenology using PCs has been proposed. Lastly, we lack a clear picture of how plant phenological trends are shifting in climatically heterogenous mountain landscapes, and how this is affecting ecosystem productivity. In the following four paragraphs, we will provide an overview of the current state of the art in relation to the four knowledge gaps, as well as outline the objectives of the studies conducted to address these gaps.

Grassland fractional vegetation cover monitoring

Grassland FVC changes have widely been used as indicators of grassland degradation, since they well reflect changes in grasslands functioning caused by global change (Liang & Wang, 2020; Wiesmair et al., 2016). There are two primary methods for estimating FVC: field measurement and RS retrieval. Under the first approach, FVC has initially been estimated using subjective methods like visual estimation, but later more objective methods like the grid method and the point count sampling method emerged as new standards (Liang & Wang, 2020). In the last three decades, thanks to the easier access to digital photographic

equipment, image classification became the privileged method for FVC estimation (Booth et al., 2005). Empirical models linking grassland spectral properties detected by satellites to FVC have been used for a long time, since Graetz et al. (1988) predicted FVC using Landsat imagery. MODIS imagery has also proved to accurately monitor grassland degradation at coarse spatial resolution (500 m) (Guerschman et al., 2009; Kim et al., 2020; Liu et al., 2021; Yang et al., 2016). Long time series derived from images at medium spatial resolution are necessary to monitor gradual changes across large areas. Vegetation index time series derived from Landsat images during 1984-2021, for example, were used to assess the "greening" of two-thirds of the area above tree line in the Alps (Rumpf et al., 2022). The recent advent of S2 and PS imagery has the potential to revolutionize FVC global monitoring capabilities. They offer the ability to estimate FVC on a weekly to daily basis and provide near-real-time monitoring at spatial resolutions ranging from 10 to 3 meters (Ustin & Middleton, 2021). However, to our knowledge, no previous study assessed the capability of these imageries in grassland FVC estimation. In the first study we tackle this challenge, and we specifically aim to i) shed light on the sensitivity of spectral regions to changes in FVC and ii) compare the FVC prediction capability of models developed using different optical imagery. The developed models could be used to estimate grassland FVC in areas where it changes at a very fine scale. The developed models can be used for a variety of purposes, such as monitoring the recovery of grasslands following extreme weather events or ecological restoration, or monitoring the degradation of grasslands in overgrazed areas and steep slopes that are frequently affected by droughts or extreme precipitation events..

Grassland management intensity monitoring

Since World War II, there has been a significant change in the management of grasslands, which has resulted in the intensification of their use in lowland areas and the abandonment of marginal areas (Cocca et al., 2012; Streifeneder et al., 2007). Grassland structure and composition are largely determined by these dynamics. Grassland management affects not only fodder production and quality, but also water purification, carbon storage, plant and animal diversity conservation, cultural and aesthetic value (Assandri et al., 2019; Benoit & Simon, 2004; Hilpold et al., 2018; Klaus et al., 2021; Xiaojun et al., 2010). For these reasons, policy makers need management intensity data to develop more targeted conservation and management measures. For example, targeted subsidies can specifically be assigned to farmers managing extensive biodiversity rich grasslands. This would prevent untargeted subsidies to cause further intensification and abandonment (Herzon et al., 2018; Pe'er et al., 2017). Therefore, the importance of spatially aware data of grassland management intensity extends far beyond the mere update of productivity statistics. Grassland mowing frequency is the main factor determining grassland management intensity, and RS is emerging as a

promising method for mowing frequency estimation. Revisiting frequency, sometimes referred to as temporal resolution, is the frequency at which a satellite constellation revisits a particular location. This is a significant attribute of satellite constellations since it directly impacts their ability to effectively capture and describe vegetation processes as they unfold over time. The revisiting frequency of Landsat imagery (16 days) was high enough to monitor changes in natural grassland FVC over seasons or years on wide areas, but not to monitor sudden changes in vegetation caused by agricultural practices such as mowing events. European hay meadows are subjected to various management regimes depending on climatic, pedological, and socio-economic conditions. Mowing events are typically spaced at intervals of at least 20 days to ensure the necessary time for the grassland to regrow, and their number per year ranges from 0 to 6. The revisiting frequency of S2 imagery spans from 2 to 5 days depending on the number of S2 orbits surveying each area, so that at least a few clear-sky observations are usually available for each regrowth period. The improved revisiting frequency and the higher spatial resolution (10 m) compared to previous imageries made S2 a good candidate for grassland mowing frequency detection using time series of vegetation indices. Several studies already explored the potential of S2 for mowing frequency monitoring (Griffiths et al., 2020; Kolecka et al., 2018), but they did not include the new S2 product with improved cloud masking released by the European Space Agency after these studies started (Frantz et al., 2018). Moreover, no freely available tool with open code that can be run on cloud computing platform is currently available. In the second study we aim to develop such a tool, an algorithm fully developed in GEE and including image processing, time series smoothing, mowing event detection and spatial majority analysis. To increase the usability of our work, we release the reference mowing frequency dataset, challenging other researchers to further improve our model. Our work aims at providing a more accurate estimation model that can easily be used by researchers and agencies to analyse spatial and temporal patterns at unprecedented spatial resolution.

Grassland flowering phenology monitoring

Dense vegetation index time series derived from RS products can be used to investigate grassland phenological development and track its trends in response to climate change. Plant phenology is defined as the study of recurring life cycle stages, especially their timing and relationships with weather and climate (Schwartz, 2013). Many researchers developed approaches to process digital images acquired from a variety of sources for phenological studies. They defined routines for data filtering, curve fitting and smoothing and phenological dates extraction (Filippa et al., 2016). Flowering is a key phenological stage, since its change may influence interactions across trophic levels (Thackeray et al., 2016) and may indicate adaptation of plant reproductive strategies to the warmer climate (Jentsch et al., 2009).

Warming induced phenological changes in flowering may differ from changes in vegetative phenology, as observed by Collins et al. (2021). In addition to warming, flowering phenology shift may be determined by other global change processes like biodiversity loss (Wolf et al., 2017). The small size of grassland flowers currently limits flowering monitoring using RS to massive flowering of monospecific vegetations like eucalypt species (Dixon et al., 2021), oil seed rape fields (d'Andrimont et al., 2020), almond (Chen et al., 2019) and pear plantations (Wouters et al., 2013). The use of images for grassland flowering monitoring has been explored through repeated drone flights (Gallmann et al., 2022), but this approach is far too expensive to be extensively applied for agricultural and ecological phenological studies, and other technologies are therefore needed. In this context near-surface RS emerges as a potential candidate, since it is a relatively cheap and already well recognized method for phenology monitoring of vegetative development (Richardson, 2019). Despite the widespread use of PhenoCams (PC) in phenological studies and the frequent use of grasslands as model ecosystems in ecological studies, automated routines, and analysis processes to monitor grassland flowering phenology using PC still need to be developed. Many challenges currently limit the use of PC, including light conditions variability, low spectral detail, high number of species and grassland structure itself. Flowers have relatively small size compared to pixels and are often occluded by vegetative plant parts. In the third study we present a workflow to extract single (or group of) species flowering phenology from grassland species mixtures using time-lapse cameras. The workflow we developed addresses these challenges in PC imagery processing by leveraging the high temporal resolution of PC imagery, increasing the spectral separability through vegetation indices computation, and improving discrimination among flower species by their shapes through texture features calculation. We present an example application on experimental grassland plots of different diversity levels. Such a workflow may be used in basic and applied ecological research in both experimental as well as observational settings.

Recent phenological trends in climatically heterogeneous mountain landscapes

The advantage of satellite RS compared to direct human observations and to near-surface RS in tracking discrete phenological events such as budburst, flowering, autumn decolouring, and leaf-fall, relies in its capability of delivering data on regional to global scales (Dronova & Taddeo, 2022). RS was used to describe the phenological response to the extension of the potential thermal growing season, and consistent discrepancies were identified (Fu et al., 2023; Menzel et al., 2006). These discrepancies were attributed to the lack of the necessary winter chilling requirement for leaf unfolding in a warmer climate (Fu et al., 2015, 2023; Menzel et al., 2020) and to the photoperiod control on spring phenology (Meng et al., 2021). Moreover, it was recently observed that the increased growing-season productivity may limit or

counteract the delaying trend in autumn leaf senescence led by warming, especially in years with warmer springs (Zani et al., 2020; Zohner et al., 2023). The aforementioned changes strongly interact with the climate system through complex feedbacks determined by changes in albedo, surface roughness, canopy conductance, water and energy flows, soil carbon decomposition, and emissions of biogenic volatile organic compounds (Peñuelas et al., 2009; Piao et al., 2008, 2019; Richardson et al., 2013). Even though some papers underline that the extended growing seasons determined a higher net carbon uptake from atmosphere in temperature-limited ecosystems (Dragoni et al., 2011; Keenan et al., 2014; Richardson et al., 2009, 2010, 2013), the overall response of the carbon budget to current and future changes in phenology is not fully understood (Piao et al., 2019). Moreover, phenological trends show high spatial variability, with local trends not always reflecting regional and continental trends. This is a crucial aspect since studies over wide regions are usually performed using coarse spatial resolution which may not be sufficient to detect processes happening along elevational gradients and in fragmented landscape (Vitasse et al., 2018; Zhang et al., 2017). However, elevational patterns in phenology and the coupling between phenology and productivity across major mountain chains remain unclear, hindering our understanding of the future functioning of mountain vegetation in a warming world. In the fourth study we aim to contribute to fill this existing knowledge gap by exploring the variability of trends in phenology at finer scale along elevational gradients in fragmented landscapes. Specifically, we aim to verify the entity and variability of the phenological trends across elevational gradients, mountain regions and vegetation types, the uniformization of phenology along elevational gradients and the concurrent change of growing season length and productivity. Such advancement in the knowledge is needed to update simulations of potential carbon uptake of terrestrial ecosystems in the future climate change scenarios and for the adaptation of grassland management practices timing.

Research objective summary

The four conducted studies aim to tackle fundamental methodological and ecological knowledge gaps in the field of grassland global change research. The preceding paragraphs provided a detailed definition of the research objectives, which are presented here in a more condensed manner. The objectives of this Ph.D. thesis are as follows: i) to assess the grassland fractional vegetation cover prediction capability of newly available remote sensing products; ii) to develop a easy to use, free, and cloud-based tool for grassland management intensity monitoring; iii) to develop a workflow for grassland flowering phenology extraction using time-lapse cameras; iv) to better understand how plant phenological trends are shifting in climatically heterogeneous mountain landscapes, and how this is affecting ecosystem productivity.

Study summaries

Study I. Estimating grassland vegetation cover with remote sensing: A comparison between Landsat-8, Sentinel-2 and PlanetScope imagery

Grassland fractional vegetation cover (FVC) accurate mapping on a large scale is crucial, since degraded grasslands contribute less to provisioning services, carbon storage, water purification, erosion control and biodiversity conservation. The spatial and temporal resolution of Sentinel-2 (S2) and PlanetScope (PS) data has never been explored for grassland FVC estimation so far and will enable researchers and agencies to quantify and map timelier and more precisely grassland processes. In this paper we compare FVC estimation models developed from Landsat-8 (L8), S2 and PS imagery. The reference grassland FVC dataset was obtained on the Paganella ski runs (46.15°N, 11.01°E, Italy) applying unsupervised classification to nadir grassland RGB photographs taken from 1.35 m above the soil. Fractional Response Models between reference FVC and 18 vegetation indices (VIs) extracted from satellite imagery were fitted and analysed. Then, leave-one-out cross validation and spatiotemporal change analysis were also performed. Our study confirms the robustness of the commonly used VIs based on the difference between NIR and the red wavelength region (R^2 = 0.91 for EVI using S2 imagery) and indicate that VIs based on the red-edge spectral region are the best performing for PS imagery (R^2 = 0.89 for RECI). Only medium to high spatial resolution imagery (S2 and PS) precisely mapped spatial patterns at the study site, since grasslands FVC varies at a fine scale. Previously available imagery at medium to low spatial and temporal resolution (e.g., L8) may still be interesting for analysis requiring long time-series of data.

Study II. Detection of grassland mowing frequency using time series of vegetation indices from Sentinel-2 imagery

Management intensity deeply influences meadow structure and functioning, therefore affecting grassland ecosystem services. Conservation and management measures, including European Common Agricultural Policy subsidies, should therefore be based on updated and publicly available data about management intensity. The mowing frequency is a crucial trait to describe meadows management intensity, but the potential of using vegetation indices from Sentinel-2 imagery for its retrieval has not been fully exploited. In this work we developed on

the Google Earth Engine platform a four-phases algorithm to identify mowing frequency, including i) vegetation index time-series computing, ii) smoothing and resampling, iii) mowing detection, and iv) majority analysis. Mowing frequency during 2020 of 240 ha of grassland fields in the Italian Alps was used for algorithm optimization and evaluation. Six vegetation indexes (EVI, GVMI, MTCI, NDII, NDVI, RENDVI$_{783.740}$) were tested as input to the proposed algorithm. The Normalized Difference Infrared Index (NDII) showed the best performance, resulting in mean absolute error of 0.07 and 93% overall accuracy on average at the four sites used for optimization, at pixel resolution. A slightly lower accuracy (mean absolute error = 0.10, overall accuracy = 90%) was obtained aggregating the maps to management parcels. The algorithm showed a good generalization ability, with a similar performance between global and local optimization and an average mean absolute error of 0.12 and an overall accuracy of 89% on average on the sites not used for parameters optimization. The lowest accuracies occurred in intensively managed grasslands surveyed by one satellite orbit only. This study demonstrates the suitability of the proposed algorithm to monitor very fragmented grasslands in complex mountain ecosystems. Google Earth Engine was used to develop the model and will enable researchers, agencies and practitioners to easily and quickly apply the code to map grassland mowing frequency for extensive grasslands protection and conservation, for mowing event verification, or for forage system characterization.

Study III. Extracting flowering phenology from grassland species mixtures using time-lapse cameras

Understanding the impacts of climate change on plant phenology is crucial for predicting ecosystem responses. However, accurately tracking the flowering phenology of individual plant species in grassland species mixtures is challenging, hindering our ability to study the impacts of biotic and abiotic factors on plant reproduction and plant-pollinator interactions. Here, we present a workflow for extracting flowering phenology from grassland species mixtures using near-surface time-lapse cameras. We used 89 image series acquired in plots with known species composition at the Jena trait-based experiment (Germany) to develop random forest classifiers, which were used to classify images and compute time series of flower cover for each species. The high temporal resolution of time-lapse cameras allowed to select images in proper light conditions, and to extract vegetation indices and texture metrics to improve discrimination among flowering species. The random forest classifiers showed a high accuracy in predicting the cover of *Leucanthemum vulgare*, *Ranunculus acris*, and *Knautia arvensis* flowers, whereas graminoid flowers were harder to predict due to their green-to-brownish colours. The proposed workflow can be applied in climate change studies,

ecosystem functioning, plant community ecology, and biodiversity change research, including the investigation of effects of species richness on individual species' flowering phenology. Our method could be a valuable tool for understanding the impacts of climate change on plant reproduction and ecosystem dynamics.

Study IV. Diverging trends in plant phenology across European mountains in a warming world

Global warming is affecting both the phenology and productivity of plant ecosystems, with big implications for carbon cycling on land. However, we continue to lack a clear picture of how plant phenological trends are shifting in climatically heterogeneous mountain landscapes, and how this is affecting ecosystem productivity. Using satellite data, our study reveals substantial differences in the phenological response among vegetation types and across elevations in the European mountains from 2001 to 2021. These divergent trends led to a more uniform spring phenology across elevations in natural grasslands, while broadleaved forests exhibited the opposite trend. Despite global warming increasing both the growing season length and gross primary productivity, we only found a weak correlation between the two ($R^2 < 0.02$), indicating that phenology has not been the primary factor limiting productivity over the past two decades.

Conclusions and further perspectives

In the four studies of the thesis, we provided significant advancements in the field of grassland monitoring using remote sensing (RS) and indicated paths for further investigation. Specifically, we developed user-friendly and extensively documented tools for monitoring grassland changes in response to global change and analysed the phenological response of European grasslands to global warming and its coupling with productivity.

We developed tools for grassland Fractional Vegetation Cover (FVC), mowing frequency, and flowering phenology monitoring. The three models successfully estimated the key grassland parameters under investigation. Regarding FVC, our findings demonstrated that the raw spectral signature of grasslands does not exhibit a linear variation across the FVC gradient, and that vegetation indices computation can greatly improve the spectral separability of FVC levels. We confirmed the prediction capability of widely used vegetation indices based on the difference between near-infrared and red wavelength regions (Rouse et al., 1974), and indices including the red-edge wavelength region, available for Sentinel-2 and PlanetScope imageries (Gao et al., 2020). The spatio-temporal change analysis assessed the success of Sentinel-2 and PlanetScope imageries for FVC monitoring. These two imageries showed a higher FVC prediction capability compared to previously available Landsat-8 imagery, especially in areas where FVC changes at a very fine scale in response to patchy degradation and restoration processes. Previously available imagery at medium to low spatial and temporal resolution may still be interesting for analysis requiring long time series. We suggest the following promising paths for further investigation: i) the comparison of multispectral images to hyperspectral images and radar images for FVC prediction, ii) the application of the developed models to analyse spatio-temporal patterns of grassland degradation and restoration.

We introduced a model for estimating grassland mowing frequency, which can effectively be utilized under different management and environmental conditions. Thanks to the improved cloud masking (Frantz et al., 2018), time series pre-processing, and extensive calibration, the model's mean absolute error at validation sites is very low (0.12), while the overall accuracy is 89%. The major novel aspects of the presented algorithm are that it was validated on very small and fragmented parcels compared to previous studies, it works at pixel level allowing mowing frequency estimation in areas where management parcels are not available (Inglada et al., 2012), and it can be run using a provided ready to use code working on a planetary-scale cloud platform (Gorelick et al., 2017). Paths for further improvement could be the inclusion of a classification algorithm for detecting management parcel geometries, a classification algorithm for detecting the type of grassland management, and the automatic definition of the start and the end of growing season at a pixel-size resolution (Jönsson &

Eklundh, 2004). Moreover, we identified Planetscope imagery as the best candidate for future mowing detection algorithms, even though the cost of this imagery currently limits the potential application on wide areas.

We presented the first workflow for flowering phenology extraction of single (or group of) species from time-lapse cameras. We proposed an automated selection of vegetation indices and texture metric features to enhance the accuracy and processing time of a random forest classifier. Additional proposed phases were image selection, time series processing, and phenometric extraction. The workflow opened new possibilities for phenological studies, overcoming laborious and time-consuming ground-based vegetation observations in both experimental as well as observational settings (Szigeti et al., 2016). Fields of application span from climate change studies over ecosystem functioning to plant community ecology and biodiversity change research. For example, the workflow can be used to assess the effects of increased carbon dioxide concentrations and higher temperatures, heat and drought stress on reproductive phenology, and the mismatches between phenological responses to warming across trophic levels (Collins et al., 2021; Dorji et al., 2020). Paths for further improvement of the method are the use of active learning to reduce labelling effort and the application of computer vision methods (Tuia et al., 2009). Computer vision techniques require a much higher labelling effort, but the increasing availability of pre-trained models that can be fine-tuned suggests that, in some cases, they could be applied to estimate species flower cover in grassland mixtures (Gallmann et al., 2022; Mann et al., 2022; Wäldchen & Mäder, 2017).

The three presented models were published together with the necessary equations, codes, and reference materials according to FAIR (Findable, Accessible, Interoperable, and Reusable) principles. By following the FAIR principles, we aimed to maximize reproducibility, data reuse and facilitate the rapid advancement of scientific knowledge. For example, to our knowledge there was no previously available reference dataset of grassland mowing frequency. Our dataset is now uploaded in GitHub (https://github.com/andreattad/S2_mowing_detection) and may be used to improve the method we proposed (https://code.earthengine.google.com/5509a44086d9cc7b81fa00dc484a6dcf) or to develop new models with different imageries. The labelled dataset of flower images (9000 labelled pixels) uploaded on the ETH Zurich repository (https://www.research-collection.ethz.ch/handle/20.500.11850/634004) can be used together with the tutorial provided in GitHub (https://github.com/andreattad/Flower_covers_phenocams) or to challenge the accuracy of our model, for example, by creating new models using computer vision algorithms.

We used well established RS products to analyse the phenological response of natural grasslands and broadleaved forests to global warming across elevations and its coupling with productivity over the past two decades. Compared to previous studies we investigated phenological trends at finer spatial resolution along elevational gradients in fragmented landscapes, minimizing the mixed-pixel challenge of moderate-resolution satellite imagery, better accounting for vegetation type change and investigating a more recent period We observed a great spatial variability of phenological trends across altitudes and geographic regions. In contrast to previous studies (Piao et al., 2019), we observed a bigger change in autumn phenology (delay) than in spring phenology (advancement). Our study reveals substantial differences in the phenological response among vegetation types and across elevations. These divergent trends led to a more uniform spring phenology across elevations in natural grasslands, while broadleaved forests exhibited the opposite trend. Interestingly, we identified some vast areas where contiguous grasslands and broadleaved forests showed opposite trends, raising questions about the different physiological regulatory mechanisms and about the implications for vegetations interactions. Despite global warming increasing both the growing season length and gross primary productivity, we only found a weak correlation between the two ($R^2<0.02$). This unexpected result (Keenan et al., 2014) suggests that in the last two decades phenology has not been the main factor limiting productivity. The patterns revealed in our analysis should be considered in simulations of the potential carbon uptake of terrestrial ecosystems in the future climate change scenarios (Bayar et al., 2023; Lovato et al., 2022).

Our findings can support grassland management and its adaptation to the current climatic conditions by providing valuable insights into ongoing grassland processes. The FVC estimation model can be used to timely monitor grassland degradation and recovery at farm to regional scale to ensure fast interventions, whereas the mowing frequency estimation model can be used at regional scale to promote more targeted conservation and management measures. Lastly, the recent trends in grassland phenology and productivity in the European mountains suggest that alpine pastures grazing should start earlier, especially at higher elevations, and that the carrying capacity of natural grassland has recently increased. In these four studies, we aimed to address important issues in grassland global change research by providing methodological and ecological advancements. Overall, this thesis showed that remote sensing images and processing workflows can greatly contribute to a better understanding of human- and climate-induced processes impacting grassland and forest ecosystems.

Acknowledgments

Bibliography

Ahlström, A., Raupach, M. R., Schurgers, G., Smith, B., Arneth, A., Jung, M., Reichstein, M., Canadell, J. G., Friedlingstein, P., Jain, A. K., Kato, E., Poulter, B., Sitch, S., Stocker, B. D., Viovy, N., Wang, Y. P., Wiltshire, A., Zaehle, S., & Zeng, N. (2015). The dominant role of semi-arid ecosystems in the trend and variability of the land CO2 sink. *Science*, *348*(6237). https://doi.org/10.1126/science.aaa1668

Assandri, G., Bogliani, G., Pedrini, P., & Brambilla, M. (2019). Toward the next Common Agricultural Policy reform: Determinants of avian communities in hay meadows reveal current policy's inadequacy for biodiversity conservation in grassland ecosystems. *Journal of Applied Ecology*, *56*(3), 604–617. https://doi.org/10.1111/1365-2664.13332

Bai, Y., & Cotrufo, M. F. (2022). Grassland soil carbon sequestration: Current understanding, challenges, and solutions. *Science*, *377*(6606), 603–608. https://doi.org/10.1126/science.abo2380

Bardgett, R. D., Bullock, J. M., Lavorel, S., Manning, P., Schaffner, U., Ostle, N., Chomel, M., Durigan, G., L. Fry, E., Johnson, D., Lavallee, J. M., Le Provost, G., Luo, S., Png, K., Sankaran, M., Hou, X., Zhou, H., Ma, L., Ren, W., … Shi, H. (2021). Combatting global grassland degradation. *Nature Reviews Earth and Environment*, *2*(10), 720–735. https://doi.org/10.1038/s43017-021-00207-2

Bayar, A. S., Yılmaz, M. T., Yücel, İ., & Dirmeyer, P. (2023). CMIP6 Earth System Models Project Greater Acceleration of Climate Zone Change Due To Stronger Warming Rates. *Earth's Future*, *11*(4). https://doi.org/10.1029/2022EF002972

Benoit, M., & Simon, J. C. (2004). Grassland and water resources: recent findings and challenges in Europe. *Proceedings of the 20 Th General Meeting, Land Use System in Grassland Dominated Regions, 21-24 June, 2004, Luzern, Switzerland*, 117–118.

Booth, T. D., Cox, S. E., Fifield, C., Phillips, M., Williamson, N., Booth, D. T., Cox, S. E., Fifield, C., Phillips, M., & Willamson, N. (2005). Image Analysis Compared with Other Methods for Measuring Ground Cover. *Arid Land Research and Management*, *19*(2), 91–100. https://doi.org/10.1080/15324980590916486

Chang, J., Ciais, P., Viovy, N., Soussana, J. F., Klumpp, K., & Sultan, B. (2017). Future productivity and phenology changes in European grasslands for different warming levels: Implications for grassland management and carbon balance. *Carbon Balance and Management*, *12*(1). https://doi.org/10.1186/s13021-017-0079-8

Chen, B., Jin, Y., & Brown, P. (2019). An enhanced bloom index for quantifying floral phenology using multi-scale remote sensing observations. *ISPRS Journal of Photogrammetry and Remote Sensing*, *156*, 108–120. https://doi.org/10.1016/j.isprsjprs.2019.08.006

Cocca, G., Sturaro, E., Gallo, L., & Ramanzin, M. (2012). Is the abandonment of traditional livestock farming systems the main driver of mountain landscape change in Alpine areas? *Land Use Policy*, *29*(4), 878–886. https://doi.org/10.1016/j.landusepol.2012.01.005

Collins, C. G., Elmendorf, S. C., Hollister, R. D., Henry, G. H. R., Clark, K., Bjorkman, A. D., Myers-Smith, I. H., Prevéy, J. S., Ashton, I. W., Assmann, J. J., Alatalo, J. M., Carbognani, M., Chisholm, C., Cooper, E. J., Forrester, C., Jónsdóttir, I. S., Klanderud, K., Kopp, C. W., Livensperger, C., … Suding, K. N. (2021). Experimental warming differentially affects vegetative and reproductive phenology of tundra plants. *Nature Communications 2021 12:1*, *12*(1), 1–12. https://doi.org/10.1038/s41467-021-23841-2

d'Andrimont, R., Taymans, M., Lemoine, G., Ceglar, A., Yordanov, M., & van der Velde, M. (2020). Detecting flowering phenology in oil seed rape parcels with Sentinel-1 and -2 time

series. *Remote Sensing of Environment*, *239*, 111660. https://doi.org/10.1016/J.RSE.2020.111660

Dixon, D. J., Callow, J. N., Duncan, J. M. A., Setterfield, S. A., & Pauli, N. (2021). Satellite prediction of forest flowering phenology. *Remote Sensing of Environment*, *255*, 112197. https://doi.org/10.1016/J.RSE.2020.112197

Dorji, T., Hopping, K. A., Meng, F., Wang, S., Jiang, L., & Klein, J. A. (2020). Impacts of climate change on flowering phenology and production in alpine plants: The importance of end of flowering. *Agriculture, Ecosystems & Environment*, *291*, 106795. https://doi.org/10.1016/J.AGEE.2019.106795

Dragoni, D., Schmid, H. P., Wayson, C. A., Potter, H., Grimmond, C. S. B., & Randolph, J. C. (2011). Evidence of increased net ecosystem productivity associated with a longer vegetated season in a deciduous forest in south-central Indiana, USA. *Global Change Biology*, *17*(2), 886–897. https://doi.org/10.1111/J.1365-2486.2010.02281.X

Dronova, I., & Taddeo, S. (2022). Remote sensing of phenology: Towards the comprehensive indicators of plant community dynamics from species to regional scales. *Journal of Ecology*, *110*(7), 1460–1484. https://doi.org/10.1111/1365-2745.13897

Filippa, G., Cremonese, E., Migliavacca, M., Richardson, A., Galvagno, M., & Forkel, M. (2016). *Phenopix: pixel based phenology*. *September*.

Frantz, D., Haß, E., Uhl, A., Stoffels, J., & Hill, J. (2018). Improvement of the Fmask algorithm for Sentinel-2 images: Separating clouds from bright surfaces based on parallax effects. *Remote Sensing of Environment*, *215*, 471–481. https://doi.org/10.1016/j.rse.2018.04.046

Fu, Y. H., Geng, X., Chen, S., Wu, H., Hao, F., Zhang, X., Wu, Z., Zhang, J., Tang, J., Vitasse, Y., Zohner, C. M., Janssens, I., Stenseth, N. Chr., & Peñuelas, J. (2023). Global warming is increasing the discrepancy between green (actual) and thermal (potential) seasons of temperate trees. *Global Change Biology*, *29*(5), 1377–1389. https://doi.org/10.1111/gcb.16545

Fu, Y. H., Zhao, H., Piao, S., Peaucelle, M., Peng, S., Zhou, G., Ciais, P., Huang, M., Menzel, A., Peñuelas, J., Song, Y., Vitasse, Y., Zeng, Z., & Janssens, I. A. (2015). Declining global warming effects on the phenology of spring leaf unfolding. *Nature 2015 526:7571*, *526*(7571), 104–107. https://doi.org/10.1038/nature15402

Gallmann, J., Schüpbach, B., Jacot, K., Albrecht, M., Winizki, J., Kirchgessner, N., & Aasen, H. (2022). Flower Mapping in Grasslands With Drones and Deep Learning. *Frontiers in Plant Science*, *12*. https://doi.org/10.3389/fpls.2021.774965

Gang, C., Zhou, W., Chen, Y., Wang, Z., Sun, Z., Li, J., Qi, J., & Odeh, I. (2014). Quantitative assessment of the contributions of climate change and human activities on global grassland degradation. *Environmental Earth Sciences*, *72*(11), 4273–4282. https://doi.org/10.1007/S12665-014-3322-6/FIGURES/5

Gao, L., Wang, X., Johnson, B. A., Tian, Q., Wang, Y., Verrelst, J., Mu, X., & Gu, X. (2020). Remote sensing algorithms for estimation of fractional vegetation cover using pure vegetation index values: A review. *ISPRS Journal of Photogrammetry and Remote Sensing*, *159*, 364–377. https://doi.org/10.1016/j.isprsjprs.2019.11.018

Gorelick, N., Hancher, M., Dixon, M., Ilyushchenko, S., Thau, D., & Moore, R. (2017). Google Earth Engine: Planetary-scale geospatial analysis for everyone. *Remote Sensing of Environment*, *202*, 18–27. https://doi.org/10.1016/j.rse.2017.06.031

Graetz, R. D., Pech, R. P., & Davis, A. W. (1988). The assessment and monitoring of sparsely vegetated rangelands using calibrated Landsat data. *International Journal of Remote Sensing*, *9*(7), 1201–1222. https://doi.org/10.1080/01431168808954929

Griffiths, P., Nendel, C., Pickert, J., & Hostert, P. (2020). Towards national-scale characterization of grassland use intensity from integrated Sentinel-2 and Landsat time series. *Remote Sensing of Environment*, *238*, 111124. https://doi.org/10.1016/j.rse.2019.03.017

Guerini Filho, M., Kuplich, T. M., & Quadros, F. L. F. D. (2020). Estimating natural grassland biomass by vegetation indices using Sentinel 2 remote sensing data. *International Journal of Remote Sensing*, *41*(8). https://doi.org/10.1080/01431161.2019.1697004

Guerschman, J. P., Hill, M. J., Renzullo, L. J., Barrett, D. J., Marks, A. S., & Botha, E. J. (2009). Estimating fractional cover of photosynthetic vegetation, non-photosynthetic vegetation and bare soil in the Australian tropical savanna region upscaling the EO-1 Hyperion and MODIS sensors. *Remote Sensing of Environment*, *113*(5), 928–945. https://doi.org/10.1016/J.RSE.2009.01.006

Herzon, I., Birge, T., Allen, B., Povellato, A., Vanni, F., Hart, K., Radley, G., Tucker, G., Keenleyside, C., Oppermann, R., Underwood, E., Poux, X., Beaufoy, G., & Pražan, J. (2018). Time to look for evidence: Results-based approach to biodiversity conservation on farmland in Europe. *Land Use Policy*, *71*, 347–354. https://doi.org/10.1016/j.landusepol.2017.12.011

Hilpold, A., Seeber, J., Fontana, V., Niedrist, G., Rief, A., Steinwandter, M., Tasser, E., & Tappeiner, U. (2018). Decline of rare and specialist species across multiple taxonomic groups after grassland intensification and abandonment. *Biodiversity and Conservation*, *27*(14), 3729–3744. https://doi.org/10.1007/s10531-018-1623-x

Inglada, J., Dejoux, J.-F., Hagolle, O., & Dedieu, G. (2012). Multi-temporal remote sensing image segmentation of croplands constrained by a topographical database. *2012 IEEE International Geoscience and Remote Sensing Symposium*, 6781–6784. https://doi.org/10.1109/IGARSS.2012.6352607

IPBES. (2018). Assessment report on land degradation and restoration assessment - summary for policymakers. In *Ipbes*.

Jentsch, A., Kreyling, J., Boettcher-Treschkow, J., & Beierkuhlein, C. (2009). Beyond gradual warming: extreme weather events alter flower phenology of European grassland and heath species. *Global Change Biology*, *15*(4), 837–849. https://doi.org/10.1111/j.1365-2486.2008.01690.x

Jönsson, P., & Eklundh, L. (2004). TIMESAT - A program for analyzing time-series of satellite sensor data. *Computers and Geosciences*, *30*(8), 833–845. https://doi.org/10.1016/j.cageo.2004.05.006

Keenan, T. F., Gray, J., Friedl, M. A., Toomey, M., Bohrer, G., Hollinger, D. Y., Munger, J. W., O'Keefe, J., Schmid, H. P., Wing, I. S., Yang, B., & Richardson, A. D. (2014). Net carbon uptake has increased through warming-induced changes in temperate forest phenology. *Nature Climate Change*, *4*(7), 598–604. https://doi.org/10.1038/nclimate2253

Kim, J., Kang, S., Seo, B., Narantsetseg, A., & Han, Y. (2020). Estimating fractional green vegetation cover of Mongolian grasslands using digital camera images and MODIS satellite vegetation indices. *GIScience & Remote Sensing*, *57*(1), 49–59. https://doi.org/10.1080/15481603.2019.1662166

Kipling, R. P., Virkajärvi, P., Breitsameter, L., Curnel, Y., De Swaef, T., Gustavsson, A. M., Hennart, S., Höglind, M., Järvenranta, K., Minet, J., Nendel, C., Persson, T., Picon-Cochard, C., Rolinski, S., Sandars, D. L., Scollan, N. D., Sebek, L., Seddaiu, G., Topp, C. F. E., … Bellocchi, G. (2016). Key challenges and priorities for modelling European grasslands under climate change. In *Science of the Total Environment* (Vols. 566–567). https://doi.org/10.1016/j.scitotenv.2016.05.144

Klaus, F., Tscharntke, T., Uhler, J., & Grass, I. (2021). Calcareous grassland fragments as sources of bee pollinators for the surrounding agricultural landscape. *Global Ecology and Conservation*, *26*, e01474. https://doi.org/10.1016/j.gecco.2021.e01474

Kolecka, N., Ginzler, C., Pazur, R., Price, B., & Verburg, P. H. (2018). Regional scale mapping of grassland mowing frequency with Sentinel-2 time series. *Remote Sensing*, *10*(8), 1221. https://doi.org/10.3390/rs10081221

Li, T., Cui, L., Scotton, M., Dong, J., Xu, Z., Che, R., Tang, L., Cai, S., Wu, W., Andreatta, D., Wang, Y., Song, X., Hao, Y., & Cui, X. (2022). Characteristics and trends of grassland degradation research. *Journal of Soils and Sediments*. https://doi.org/10.1007/s11368-022-03209-9

Liang, S., & Wang, J. (2020). Fractional vegetation cover. In Academic Press (Ed.), *Advanced Remote Sensing* (Second edi, pp. 477–510). Elsevier. https://doi.org/10.1016/B978-0-12-815826-5.00012-X

Liu, D., Jia, K., Xia, M., Wei, X., Yao, Y., Zhang, X., & Tao, G. (2021). Fractional Vegetation Cover Estimation Algorithm Based on Recurrent Neural Network for MODIS 250 m Reflectance Data. *IEEE Journal of Selected Topics in Applied Earth Observations and Remote Sensing*, *14*, 6532–6543. https://doi.org/10.1109/JSTARS.2021.3075624

Lovato, T., Peano, D., Butenschön, M., Materia, S., Iovino, D., Scoccimarro, E., Fogli, P. G., Cherchi, A., Bellucci, A., Gualdi, S., Masina, S., & Navarra, A. (2022). CMIP6 Simulations With the CMCC Earth System Model (CMCC-ESM2). *Journal of Advances in Modeling Earth Systems*, *14*(3), e2021MS002814. https://doi.org/10.1029/2021MS002814

Mann, H. M. R., Iosifidis, A., Jepsen, J. U., Welker, J. M., Loonen, M. J. J. E., & Høye, T. T. (2022). Automatic flower detection and phenology monitoring using time-lapse cameras and deep learning. *Remote Sensing in Ecology and Conservation*. https://doi.org/10.1002/rse2.275

Meng, L., Zhou, Y., Gu, L., Richardson, A. D., Peñuelas, J., Fu, Y., Wang, Y., Asrar, G. R., De Boeck, H. J., Mao, J., Zhang, Y., & Wang, Z. (2021). Photoperiod decelerates the advance of spring phenology of six deciduous tree species under climate warming. *Global Change Biology*, *27*(12), 2914–2927. https://doi.org/10.1111/GCB.15575

Menzel, A., Sparks, T. H., Estrella, N., Koch, E., Aasa, A., Ahas, R., Alm-Kübler, K., Bissolli, P., Braslavská, O., Briede, A., CHMIELEWSKI, F. M., CREPINSEK, Z., CURNEL, Y., DAHL, Å., DEFILA, C., DONNELLY, A., FILELLA, Y., JATCZAK, K., MÅGE, F., … ZUST, A. (2006). European phenological response to climate change matches the warming pattern. *Global Change Biology*, *12*(10), 1969–1976. https://doi.org/10.1111/j.1365-2486.2006.01193.x

Menzel, A., Yuan, Y., Matiu, M., Sparks, T., Scheifinger, H., Gehrig, R., & Estrella, N. (2020). Climate change fingerprints in recent European plant phenology. *Global Change Biology*, *26*(4), 2599–2612. https://doi.org/10.1111/gcb.15000

Pe'er, G., Lakner, S., Müller, R., Passoni, G., Bontzorlos, V., Clough, D., Moreira, F., Azam, C., Berger, J., Bezak, P., Bonn, A., Hansjürgens, B., Hartmann, L., Kleemann, J., Lomba, A., Sahrbacher, A., Schindler, S., Schleyer, C., Schmidt, J., … Von Cramon-Taubadel, S. (2017). *Is the CAP Fit for purpose? An evidence-based fitness-check assessment*.

Peñuelas, J., Rutishauser, T., & Filella, I. (2009). Phenology Feedbacks on Climate Change. *Science*, *324*(5929), 887–888. https://doi.org/10.1126/science.1173004

Piao, S., Ciais, P., Friedlingstein, P., Peylin, P., Reichstein, M., Luyssaert, S., Margolis, H., Fang, J., Barr, A., Chen, A., Grelle, A., Hollinger, D. Y., Laurila, T., Lindroth, A., Richardson, A. D., & Vesala, T. (2008). Net carbon dioxide losses of northern ecosystems in response to autumn warming. *Nature*, *451*(7174), 49–52. https://doi.org/10.1038/nature06444

Piao, S., Liu, Q., Chen, A., Janssens, I. A., Fu, Y., Dai, J., Liu, L., Lian, X., Shen, M., & Zhu, X. (2019). Plant phenology and global climate change: Current progresses and challenges. *Global Change Biology*, *25*(6), 1922–1940. https://doi.org/10.1111/GCB.14619

Reinermann, S., Asam, S., & Kuenzer, C. (2020). Remote sensing of grassland production and management-A review. In *Remote Sensing* (Vol. 12, Issue 12). https://doi.org/10.3390/rs12121949

Reynolds, S., & Frame, J. (2005). *Grasslands: developments, opportunities, perspectives*. Publishers, Science.

Richardson, A. D. (2019). Tracking seasonal rhythms of plants in diverse ecosystems with digital camera imagery. *New Phytologist*, *222*(4), 1742–1750. https://doi.org/10.1111/nph.15591

Richardson, A. D., Andy Black, T., Ciais, P., Delbart, N., Friedl, M. A., Gobron, N., Hollinger, D. Y., Kutsch, W. L., Longdoz, B., Luyssaert, S., Migliavacca, M., Montagnani, L., William Munger, J., Moors, E., Piao, S., Rebmann, C., Reichstein, M., Saigusa, N., Tomelleri, E., … Varlagin, A. (2010). Influence of spring and autumn phenological transitions on forest ecosystem productivity. *Philosophical Transactions of the Royal Society B: Biological Sciences*, *365*(1555), 3227–3246. https://doi.org/10.1098/rstb.2010.0102

Richardson, A. D., Braswell, B. H., Hollinger, D. Y., Jenkins, J. P., & Ollinger, S. V. (2009). Near-surface remote sensing of spatial and temporal variation in canopy phenology. *Ecological Applications : A Publication of the Ecological Society of America*, *19*(6), 1417–1428. https://doi.org/10.1890/08-2022.1

Richardson, A. D., Keenan, T. F., Migliavacca, M., Ryu, Y., Sonnentag, O., & Toomey, M. (2013). Climate change, phenology, and phenological control of vegetation feedbacks to the climate system. *Agricultural and Forest Meteorology*, *169*, 156–173. https://doi.org/10.1016/j.agrformet.2012.09.012

Rouse, J. W., Haas, R., Schell, J., & Deering, D. (1974). Monitoring vegetation systems in the Great Plains with ERTS. *NASA Special Publication*, *351*(1974), 309.

Rumpf, S. B., Gravey, M., Brönnimann, O., Luoto, M., Cianfrani, C., Mariethoz, G., & Guisan, A. (2022). From white to green: Snow cover loss and increased vegetation productivity in the European Alps. *Science*, *376*(6597), 1119–1122. https://doi.org/10.1126/science.abn6697

Schiavon, E., Taramelli, A., Tornato, A., & Pierangeli, F. (2021). Monitoring environmental and climate goals for European agriculture: User perspectives on the optimization of the Copernicus evolution offer. *Journal of Environmental Management*, *296*, 113121. https://doi.org/10.1016/j.jenvman.2021.113121

Schwartz, M. (2013). *Phenology: An Integrative Environmental Science* (M. D. Schwartz, Ed.). Springer Netherlands. https://doi.org/10.1007/978-94-007-6925-0

Schwieder, M., Wesemeyer, M., Frantz, D., Pfoch, K., Erasmi, S., Pickert, J., Nendel, C., & Hostert, P. (2021). Mapping grassland mowing events across Germany based on combined Sentinel-2 and Landsat 8 time series. *Remote Sensing of Environment*, 112795. https://doi.org/10.1016/J.RSE.2021.112795

Streifeneder, T., Tappeiner, U., Ruffini, F. V., Tappeiner, G., & Hoffmann, C. (2007). Selected Aspects of Agro-structural Change within the Alps. *Revue de Géographie Alpine*, *95–3*, 41–52. https://doi.org/10.4000/rga.295

Szigeti, V., Kőrösi, , Ádam, Haros, A., Nagy, J., & Kis, J. (2016). Measuring floral resource availability for insect pollinators in temperate grasslands - a review. *Ecological Entomology*, *41*(3), 231–240. https://doi.org/10.1111/een.12298

Thackeray, S. J., Henrys, P. A., Hemming, D., Bell, J. R., Botham, M. S., Burthe, S., Helaouet, P., Johns, D. G., Jones, I. D., Leech, D. I., Mackay, E. B., Massimino, D., Atkinson, S., Bacon, P. J., Brereton, T. M., Carvalho, L., Clutton-Brock, T. H., Duck, C., Edwards, M., … Wanless, S. (2016). Phenological sensitivity to climate across taxa and trophic levels. *Nature*, *535*(7611), 241–245. https://doi.org/10.1038/nature18608

Tuia, D., Ratle, F., Pacifici, F., Kanevski, M. F., & Emery, W. J. (2009). Active learning methods for remote sensing image classification. *IEEE Transactions on Geoscience and Remote Sensing*, *47*(7), 2218–2232. https://doi.org/10.1109/TGRS.2008.2010404

Ustin, S. L., & Middleton, E. M. (2021). Current and near-term advances in Earth observation for ecological applications. In *Ecological Processes* (Vol. 10, Issue 1). https://doi.org/10.1186/s13717-020-00255-4

Vitasse, Y., Signarbieux, C., & Fu, Y. H. (2018). Global warming leads to more uniform spring phenology across elevations. *Proceedings of the National Academy of Sciences*, *115*(5), 1004–1008. https://doi.org/10.1073/pnas.1717342115

Wachendorf, M., Fricke, T., & Möckel, T. (2018). Remote sensing as a tool to assess botanical composition, structure, quantity and quality of temperate grasslands. *Grass and Forage Science*, *73*(1), 1–14. https://doi.org/10.1111/gfs.12312

Wäldchen, J., & Mäder, P. (2017). Plant Species Identification Using Computer Vision Techniques: A Systematic Literature Review. *Archives of Computational Methods in Engineering 2017 25:2*, *25*(2), 507–543. https://doi.org/10.1007/S11831-016-9206-Z

Wang, N., Quesada, B., Xia, L., Butterbach-Bahl, K., Goodale, C. L., & Kiese, R. (2019). Effects of climate warming on carbon fluxes in grasslands— A global meta-analysis. *Global Change Biology*, *25*(5). https://doi.org/10.1111/gcb.14603

Weber, D., Schwieder, M., Ritter, L., Koch, T., Psomas, A., Huber, N., Ginzler, C., & Boch, S. (2023). Grassland-use intensity maps for Switzerland based on satellite time series: Challenges and opportunities for ecological applications. *Remote Sensing in Ecology and Conservation*. https://doi.org/10.1002/rse2.372

Wiesmair, M., Feilhauer, H., Magiera, A., Otte, A., & Waldhardt, R. (2016). Estimating Vegetation Cover from High-Resolution Satellite Data to Assess Grassland Degradation in the Georgian Caucasus. *Mountain Research and Development*, *36*(1), 56–65. https://doi.org/10.1659/MRD-JOURNAL-D-15-00064.1

Wolf, A. A., Zavaleta, E. S., & Selmants, P. C. (2017). Flowering phenology shifts in response to biodiversity loss. *Proceedings of the National Academy of Sciences*, *114*(13), 3463–3468. https://doi.org/10.1073/pnas.1608357114

Wouters, N., De Ketelaere, B., De Baerdemaeker, J., & Saeys, W. (2013). Hyperspectral waveband selection for automatic detection of floral pear buds. *Precision Agriculture*, *14*(1), 86–98. https://doi.org/10.1007/S11119-012-9279-0/TABLES/3

Xiaojun, N., Xiaodan, W., Suzhen, L., Shixian, G., & Haijun, L. (2010). 137Cs tracing dynamics of soil erosion, organic carbon and nitrogen in sloping farmland converted from original grassland in Tibetan plateau. *Applied Radiation and Isotopes*, *68*(9), 1650–1655. https://doi.org/10.1016/j.apradiso.2010.04.017

Xie, J., Hüsler, F., de Jong, R., Chimani, B., Asam, S., Sun, Y., Schaepman, M. E., & Kneubühler, M. (2021). Spring Temperature and Snow Cover Climatology Drive the Advanced Springtime Phenology (1991–2014) in the European Alps. *Journal of Geophysical Research: Biogeosciences*, *126*(3). https://doi.org/10.1029/2020JG006150

Yang, L., Jia, K., Liang, S., Liu, J., & Wang, X. (2016). Comparison of Four Machine Learning Methods for Generating the GLASS Fractional Vegetation Cover Product from MODIS Data. *Remote Sensing*, *8*(8), 682. https://doi.org/10.3390/RS8080682

Zani, D., Crowther, T. W., Mo, L., Renner, S. S., & Zohner, C. M. (2020). Increased growing-season productivity drives earlier autumn leaf senescence in temperate trees. *Science*, *370*(6520), 1066–1071. https://doi.org/10.1126/science.abd8911

Zarei, A., Asadi, E., Ebrahimi, A., Jafari, M., Malekian, A., Mohammadi Nasrabadi, H., Chemura, A., & Maskell, G. (2020). Prediction of future grassland vegetation cover fluctuation under climate change scenarios. *Ecological Indicators*, *119*, 106858. https://doi.org/10.1016/J.ECOLIND.2020.106858

Zhang, X., Wang, J., Gao, F., Liu, Y., Schaaf, C., Friedl, M., Yu, Y., Jayavelu, S., Gray, J., Liu, L., Yan, D., & Henebry, G. M. (2017). Exploration of scaling effects on coarse resolution land surface phenology. *Remote Sensing of Environment*, *190*, 318–330. https://doi.org/10.1016/j.rse.2017.01.001

Zohner, C. M., Mirzagholi, L., Renner, S. S., Mo, L., Rebindaine, D., Bucher, R., Palouš, D., Vitasse, Y., Fu, Y. H., Stocker, B. D., & Crowther, T. W. (2023). Effect of climate warming on the timing of autumn leaf senescence reverses after the summer solstice. *Science*, *381*(6653). https://doi.org/10.1126/science.adf5098
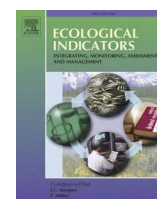
Appendix: Studies I-IV

Estimating grassland vegetation cover with remote sensing: A comparison between Landsat-8, Sentinel-2 and PlanetScope imagery

Davide Andreatta, Damiano Gianelle, Michele Scotton, Michele Dalponte

Please refer to the online version for the supplementary materials

Original Articles

Estimating grassland vegetation cover with remote sensing: A comparison between Landsat-8, Sentinel-2 and PlanetScope imagery

Davide Andreatta [a,b,*,1], Damiano Gianelle [b,2], Michele Scotton [a,3], Michele Dalponte [b,4]

[a] Department of Agronomy, Food, Natural Resources, Animals and Environment, University of Padova, Legnaro, Padova, Italy
[b] Research and Innovation Centre, Fondazione Edmund Mach, San Michele all'Adige, Trento, Italy

A R T I C L E   I N F O

A B S T R A C T

Grassland fractional vegetation cover (FVC) accurate mapping on a large scale is crucial, since degraded grasslands contribute less to provisioning services, carbon storage, water purification, erosion control and biodiversity conservation. The spatial and temporal resolution of Sentinel-2 (S2) and PlanetScope (PS) data has never been explored for grassland FVC estimation so far and will enable researchers and agencies to quantify and map timelier and more precisely grassland processes. In this paper we compare FVC estimation models developed from Landsat-8 (L8), S2 and PS imagery. The reference grassland FVC dataset was obtained on the Paganella ski runs (46.15°N, 11.01°E, Italy) applying unsupervised classification to nadir grassland RGB photographs taken from 1.35 m above the soil. Fractional Response Models between reference FVC and 18 vegetation indices (VIs) extracted from satellite imagery were fitted and analysed. Then, leave-one-out cross validation and spatiotemporal change analysis were also performed. Our study confirms the robustness of the commonly used VIs based on the difference between NIR and the red wavelength region ($R^2 = 0.91$ for EVI using S2 imagery) and indicate that VIs based on the red-edge spectral region are the best performing for PS imagery ($R^2 = 0.89$ for RECI). Only medium to high spatial resolution imagery (S2 and PS) precisely mapped spatial patterns at the study site, since grasslands FVC varies at a fine scale. Previously available imagery at medium to low spatial and temporal resolution (e.g., L8) may still be interesting for analysis requiring long time-series of data.

1. Introduction

Grassland degradation is a crucial issue, as degraded grasslands not only contribute less to provisioning services, but also to carbon storage, water purification, erosion control, biodiversity conservation, and recreation (Li et al., 2022). Grasslands cover one-third of the earth's terrestrial surface, which represent 70% of the global agricultural area (Reynolds and Frame, 2005), and over 49% of grassland area is experiencing these processes (Gang et al., 2014).

Grassland Fractional Vegetation Cover (FVC), defined as the ratio of the vertical projection area of above-ground vegetation organs on the ground to the total vegetation area, is a very informative trait in grassland monitoring (Liang and Wang, 2020). Spatiotemporal changes in FVC reflect changes in grasslands functioning caused by environmental

drivers such as erosion, revegetation, alteration of disturbance regimes, precipitation and temperature patterns.

FVC estimation is mainly performed using two approaches: field measurements and remote sensing retrieval. In the field, FVC measurement has been traditionally carried out using subjective methods like visual estimation, or more standardized sampling methods like the grid method and the point count sampling method (Liang and Wang, 2020). Thanks to the improvements in image quality, digital photography classification became a much more efficient way of FVC estimation in the field, because it is fast, replicable and objective (Booth et al., 2005; Li et al., 2005). Supervised methods (also known as manual pixel classification) and unsupervised methods (also known as automatic colour threshold) have been developed to classify each pixel (Booth et al., 2006; McCallum, 2000; Patrignani and Ochsner, 2015; Zhou et al., 1998).

Field methods are still fundamental as they provide accurate ground reference measurement for remote sensing algorithm development, which has become the most used approach in FVC estimation for large scale applications (Liang and Wang, 2020; White et al., 2000).

The most common methods proposed for FVC estimation using RS data are i) empirical model methods (also called *regression models*), ii) pixel decomposition model methods (also called *linear unmixing model*), iii) physical based methods, and iv) machine learning methods. Empirical models are constructed through the regression of remote sensing data, which can be waveband values or derived VIs, to reference FVC values. Empirical models have been successfully explored since the experience of Graetz et al. (1988) who predicted FVC using the fifth channel of Landsat MSS at a spatial resolution of 183 m reaching an accuracy of $R^2 = 0.68$. The major drawback of regression models is they are locally calibrated, and they do not necessarily generalize well. The theoretical basis of the second approach, pixel decomposition models, is that each pixel in an image is composed of several components and pixel reflectance to the sensors is assumed to result from the linear synthesis of the information of each component. The pixel decomposition methods having just two endmembers, i.e. soil and vegetation, are also called pixel dichotomy models, dimidiate pixel models, or two-endmember models and compute the FVC considering the contribution of the vegetation component (maximum VI value) and of the bare soil (minimum VI value) (Gao et al., 2020; van der Meer, 1999). The physical-based methods simulate the physical relationships between vegetation canopy spectral reflectance and FVC, and the estimation is applied by inverting a canopy radiative transfer model (CRTM). One frequent issue using these algorithms is that the input parameters are often more than the observations, thus the equation is underdetermined (Atzberger, 2004; Darvishzadeh et al., 2008). For this reason, Machine Learning algorithms are often employed to constrain and simplify the inversion process (Baret et al., 2007; Roujean and Lacaze, 2002).

The spatial resolution of images used in FVC estimation are mainly from medium to coarse, with dominant values of 30 m, 250 m, 1 km (Gao et al., 2020). The most frequently used satellite imageries are, respectively, Landsat, MODIS, and AVHRR. Most of VIs used for FVC estimation are computed based on reflectances in the red and near-infrared (NIR) wavelength region, like the SAVI used by McGwire et al. (2000), MSAVI used by Chen et al. (2016), the EVI used by Jia et al. (2017), the WDRVI used by Gitelson (2013). Also the short-wave-infrared (SWIR) wavelength region showed correlation with FVC according to Guerschman et al. (2009) and to Baret et al. (2007). High correlations were found also with the red-edge, as reported by Gitelson (2013) and Liu et al. (2007) and with the green band (Zarei et al., 2020). Only a few studies explored the use of Sentinel-2 (S2) imagery for crop FVC estimation and to our knowledge grassland FVC estimation using S2 imagery has never been tested. Verrelst et al. (2012) simulated Sentinel-2 Multi spectral Instrument band settings on the basis of Compact High Resolution Imaging Spectrometry data to estimate the FVC of 8 crops, whereas Wang et al. (2018) applied a machine learning approach to estimate FVC of maize and wheat fields using S2 imagery. S2 imagery compared to previous imagery like Landsat-8 (L8) series benefits from improved spatial and spectral resolution, with RGB and NIR bands at 10 m, 4 red-edge bands (which were not available in the L8 series) and 2 shortwave infrared bands at 20 m. One last constellation that to our knowledge has never been tested for FVC estimation is PlanetScope (PS) constellation. The last instrument generation, PSB.SD, is capable of measuring reflectances in 8 bands at the high spatial resolution of about 3 m and with a nearly daily revisiting time.

Although the possibility to use spaceborne optical imagery at coarse resolution to estimate grassland FVC have already been explored in previous works, newly available imagery with finer spatial and spectral resolution could give much more detailed information, necessary to monitor patchy processes like grassland degradation and restoration that the global change is causing (Jia et al., 2017). Especially, S2 and PS imagery has never been applied to grassland FVC estimation, even though the higher spectral, spatial and temporal resolution may lead to breakthrough innovation in FVC estimation algorithms, especially in environments where vegetation mosaic changes at a fine scale (Gao et al., 2020). The output models could be used to monitor grassland degradation and recovery and to estimate grassland density changes in response to climate change.

In this work we aim to i) shed light on the sensitivity of spectral regions to changes in FVC and ii) to compare the FVC prediction capability of models developed using different optical imagery.

2. Materials and methods

2.1. Study area

The study was conducted at the southern border of the Italian Alps, in the Province of Trento, on the Paganella ski runs (46.15°N, 11.01°E, Fig. 1A). The climate of the study site is classified as temperate oceanic supratemperate humid according to the Worldwide Bioclimatic Classification System (Sboarina and Cescatti, 2004). The rains are concentrated in summer and autumn and annual precipitation is 1508 mm. The study area altitude ranges from 1055 m a.s.l. to 1615 m a.s.l. and the temperatures registered at the nearest (Fig. 1C) weather station (1790 m a.s.l.) reach their maximum in August (average of daily maximum = 18.1 °C) and their minimum in January (average of daily minimum = -7.3 °C) (Fig. 1B). The dominant plant communities in the study area are montane and subalpine spruce forests, interrupted by ski runs revegetated from more than 70 year to one year before our field survey. Commercial seed mixtures used for revegetation were mainly composed of *Festuca rubra, Dactylis glomerata, Lolium perenne, Trifolium repens, Trifolium pratense.* Based on the age of the revegetation and on soil conditions the FVC ranges from very low to complete in the surveyed grasslands.

2.2. Ground measurements of reference FVC

To construct our FVC ground measurement reference dataset, the digital photography approach was chosen (Liang and Wang, 2020). First, we identified 46 vegetationally homogeneous areas inside the grassland areas and we defined 10 m × 10 m plots with north orientation. The plots were georeferenced with a total station. Then, in each plot we took one Nadir photograph at the plot centre and one at each corner. The photographs were taken using a RGB digital camera mounted on a tripod 1.35 m above ground level. The camera was oriented vertically downwards resulting in a field view of approximately 120 cm × 100 cm, varying based on the slope. All images were obtained in a 4608 × 3456 pixels spatial resolution with flash always off and without optical or digital zoom. The field work was conducted between June 23 and 24, 2021 and resulted in 230 photographs.

To limit image edge distortion, image edges were removed (20% of height and 20% of width) before classification. We chose the unsupervised image classification method proposed by Patrignani and Ochsner (2015). This method detects the green pixels based on colour ratios of red to green (R/G) and blue to green (B/G) and on the excess green index (2G-R-B). The green pixels can be detected by the following criteria:

$$\frac{R}{G} < P_1 \ and \ \frac{B}{G} < P_2 \ and \ 2G - R - B < P_3 \tag{1}$$

where R is the red band, G is the green band, B is the blue band and P1, P2, and P3 are three parameters set to 0.95, 0.95, 20 by default. The method was chosen because it has been already successfully used to estimate grassland FVC (Jáuregui et al., 2019; Lollato et al., 2019). The parameters were set to the default values and the classification was performed using *R* (RStudio Team, 2020) (Fig. S1). Plot FVC was computed as the average FVC of the 5 photographs. Digital images classification provided a reference dataset composed of 15 plots in the
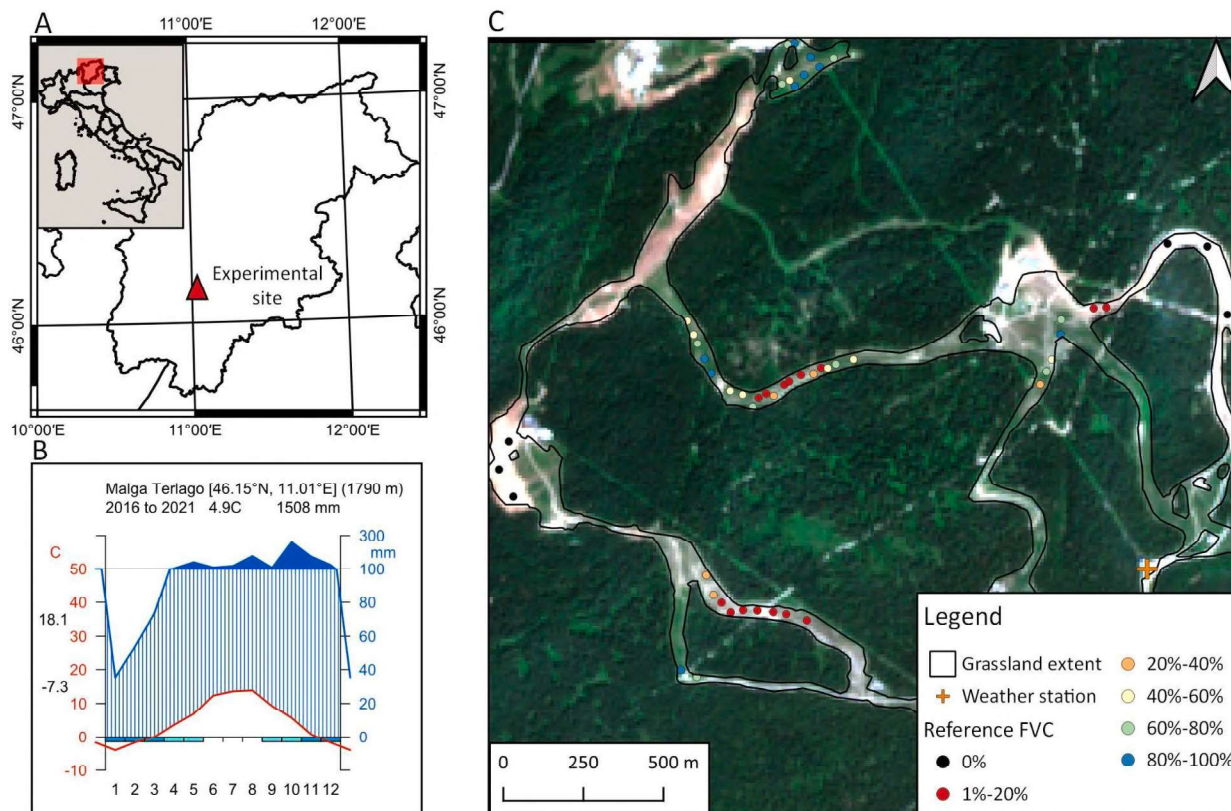
Fig. 1. A) Location of the experimental site. B) Walter & Lieth climatic diagram of the Malga Terlago weather station. Data downloaded from the weather service of the Province of Trento (www.meteotrentino.it). C) Plot Location inside the study site coloured based on their reference Fractional Vegetation Cover. Sentinel-2 Level 2A image of June 27th 2021 used as a background.

FVC range between 1% and 20%, 5 plots between 20% and 40%, 8 plots between 40% and 60%, 9 plots between 60% and 80% and 9 plots between 80% and 100%. The average standard deviations of reference FVC among subplots of each plot is 8.8 % (min = 1%, max 25%). Seven bare soil plots were also added to the dataset. In those plots the vegetation, most of the organic soil and rocks had been removed, and soil levelled for new ski runs preparation. Bare soil plots were included in the dataset to represent eroded grasslands rich in mineral soil, and to represent restored grasslands in their first stages after soil preparation.

2.3. Remote sensing imagery

For each imagery we identified the uncloudy image closest to the field survey dates (23rd and 24th June 2021), and product specification can be found in Table S1. Imagery from L8 constellation (13th of June 2021, Level 2) and S2 constellation (27th of June 2021, Level-2A) were accessed through the Earth Engine Data Catalog (https://developers.google.com/earth-engine/datasets) (Gorelick et al., 2017), whereas the PS image (23rd of June 2021, Level 3A, PSB.SD instrument) was download from the Planet API and then uploaded to the Earth Engine Code Editor for the sampling. Values of all the pixels that intersect the plots, weighted on the plot fraction intersected, were extracted for each band for the 53 plots (10 m × 10 m squares) using the *ee.Image.reduceRegions* function in Google Earth Engine. To produce the estimated FVC maps used for spatiotemporal change analysis (Fig. 5 and Fig. 6), the PS images at full resolution (3 m × 3 m) were spatially smoothed using 3 × 3 pixels moving window and assigning the mean values of the neighbourhood to the focal cell to match the calibration resolution (10 m × 10 m) without losing the fine scale detail. The *focal* function of the *raster* package in R was used to apply the spatial smoothing (Hijmans, 2021).

For the temporal change analysis described in subsection 2.7 and 3.3,

four clear-sky images taken from summer to autumn 2021, were acquired for each imagery (dates reported in Fig. 6).

2.4. Vegetation index computing

The VIs included in this study were chosen based on previous literature. We included indices which analyse the NIR wavelength region (Chen et al., 2016; Jia et al., 2017; Jiménez-Muñoz et al., 2009), the SWIR (Baret et al., 2007; Guerschman et al., 2009) and the red-edge (Gao et al., 2020). Two indices exploring the green wavelength were also included, as they were successfully used for approximating gross primary productivity of grasslands (Zhou et al., 2014). The VIs were computed for each imagery in *R* using the formulas described in Table 1. It was not possible to compute all the VIs for all the imageries, since red-edge bands are not available in L8 imagery and SWIR wavelength region is not available for PS imagery.

2.5. Grasslands FVC spectral signature analysis

To have a first understanding of the spectral signature of grasslands with various FVC, plots were grouped based on their reference FVC in six categories. The first category contains bare soils with no vegetational cover, the other five categories gather the plots based on their FVC from 1 to 100% FVC with a step of 20%. Then, for each imagery and for each band we built a boxplot graphical representation of the reflectances, grouped according to their FVC category. FVC categories were used only to display FVC levels in Figs. 2 and 3 and not to define the classes for a classification predictive model. Instead, FVC prediction was performed through Fractional Response Models, as described in the following paragraph.

Table 1
Description of vegetation indices evaluated in this study[1].

Index name	Formula	L8 bands	S2 bands	PS bands	Reference
EVI[2] (Enhanced Vegetation Index)	$G * \dfrac{NIR - RED}{(NIR + C_1 RED - C_2 BLUE) + L}$	2,4,5	2,4,8	2,6,8	(Huete et al., 2002)
GNDVI (Green Normalized Difference Vegetation Index)	$\dfrac{NIR - GREEN}{NIR + GREEN}$	3,5	3, 8A	4,8	(Gitelson et al., 1996)
GVMI (Global Vegetation Moisture Index)	$\dfrac{(NIR + 0.1) - (SWIR + 0.02)}{(NIR + 0.1) + (SWIR + 0.02)}$	5,7	8,12	–	(Ceccato et al., 2002)
MSAVI (Modified Soil Adjusted Vegetation Index)	$0.5 * (2NIR + 1 - \sqrt{(2*NIR + 1)^2 - 8(NIR - RED)})$	4,5	4,8	6,8	(Qi et al., 1994)
NBR (Normalized Burn Ratio)	$\dfrac{NIR - SWIR}{NIR + SWIR}$	5,7	8A,12	–	(García & Caselles, 1991)
NDGI (Normalized Difference Greenness Index)	$\dfrac{GREEN - RED}{GREEN + RED}$	3,4	3,4	4,6	(Courel et al., 1991)
NDMI (Normalized Difference Moisture Index)	$\dfrac{NIR - SWIR}{NIR + SWIR}$	5,6	–	–	(Hardisky et al., 1983)
NDII (Normalized Difference Infrared Index)	$\dfrac{NIR - SWIR}{NIR + SWIR}$	–	8,11	–	(Hardisky et al., 1983)
NDRE1 (Normalized Difference RE1)	$\dfrac{REDEDGE_{740} - REDEDGE_{705}}{REDEDGE_{740} + REDEDGE_{705}}$	–	5,6	–	(Gitelson & Merzlyak, 1994)
NDVI (Normalized Difference Vegetation Index)	$\dfrac{NIR - RED}{NIR + RED}$	4,5	4,8	6,8	(Rouse et al., 1974)
PSRI (Plant Senescence Reflectance Index)	$\dfrac{RED - BLUE}{REDEDGE_{705}}$	–	2,4,5	2,6,7	(Merzlyak et al., 1999)
RECI (Red- Edge Chlorophyll Index)	$\left(\dfrac{NIR}{REDEDGE_{705}}\right) - 1$	–	5,8A	7,8	(Gitelson et al., 2003)
RENDVI (Red-Edge Normalized Difference Vegetation Index)	$\dfrac{NIR - REDEDGE_{705}}{NIR + REDEDGE_{705}}$	–	5,8A	7,8	(Gitelson & Merzlyak, 1994)
RESI (Red-Edge Spectral indices)	$\dfrac{REDEDGE_{780} + REDEDGE_{740} - REDEDGE_{705}}{REDEDGE_{780} + REDEDGE_{740} + REDEDGE_{705}}$		5,6,7		(Xiao et al., 2020)
RVI (Ratio Vegetation Index)	NIR/RED	4,5	4,8	6,8	(Jordan, 1969)
SAVI[3] (Soil adjusted Vegetation Index)	$\dfrac{NIR - RED}{NIR + RED + L} * (1 + L)$	4,5	4,8	6,8	(Huete, 1988)
VARI (Visible Atmospherically Resistant Index)	$\dfrac{GREEN - RED}{GREEN + RED - BLUE}$	2,3,4	2,3,4	2,4,6	(Gitelson, 2001)
WDRVI (Wide Dynamic Range Vegetation Index	$\dfrac{0.1 * NIR - RED}{0.1 * NIR + RED}$	4,5	4,8A	6,8	(Gitelson, 2004)

[1] NIR indicates near infrared; RED, red band; BLUE, blue band; GREEN, green band; SWIR, shortwave infrared band; REDEDGE, red-edge band.
[2] G indicates Gain factor, was set to 2.5; C_1 and C_2 are coefficients of the aerosol resistance term, were set to 6 and 7.5, respectively; L indicates canopy background adjustment, was set to 1.
[3] L indicates soil brightness correction factor, was set to 0.5.

2.6. Relationship between fractional vegetation cover and vegetation indices

First, for each imagery and for each VI we explored the indices variability inside and among FVC categories. Since the dependent variable (FVC) has a fractional nature, being bounded in the unit interval, the relationships between VIs and FVC were examined through Fractional Response Models using the *frm* function of the *frm* R package (Ramalho, 2019) (see Fig. S2 for the workflow diagram). We used *logit* as a link function and quasi-likelihood method to determine parameters (eq.2). The standard fractional regression model used is defined by the following conditional expectation:

$$E(y_i|x_i) = \frac{e^{x_i\theta}}{1 - e^{x_i\theta}} \qquad (2)$$

where y_i denote the fractional response variable, defined on the interval [0,1], to be explained for individual i, $i = 1, …, N$. x_i denote the explanatory variable and θ the vector of parameters of interest. R-squared (R^2), calculated as the square of the correlation coefficient between the actual and fitted values of the dependent variable, was used for model comparison. Selected models' residuals were checked for normality and homoscedasticity by visual inspection of the residuals plot.

The residuals of the selected models were regressed against all the other indices to find eventual promising predictors for multiple VIs models. To identify possible causes of error, we tested if there were correlations between selected models' residuals and some terrain indices that may affect plot spectral signature. Altitude, aspect, slope,

topographic position index (TPI), terrain ruggedness index (TRI) and roughness were computed using the *terrain* function of the *raster* package in R. The terrain indices were computed according to Wilson et al. (2007). TRI is the mean of the absolute differences between the altitude value of a cell and the value of its eight surrounding cells. TPI is the difference between the altitude value of a cell and the mean value of its eight surrounding cells. Roughness is the difference between the maximum and the minimum value of a cell and its eight surrounding cells. To derive the terrain indices, we used a digital terrain model distributed by the Provincia Autonoma di Trento (PAT, 2016) with 10 m spatial resolution. Correlations were tested using the *cor.test* function in R, which tests for association between paired samples, using Pearson's product moment correlation coefficient (level of significance p-value < 0.05). We also tested if within plot FVC heterogeneity (standard deviation of FVC across subplots) was correlated to the residuals.

2.7. Model validation

Cross validated statistics (R^2_{CV}) with leave-one-out procedure were computed to estimate the generalization capability of the selected models. The selected models for the L8, S2 and PS imagery were applied to estimate the FVC of all the grasslands of the study site and maps were analysed. The models were also applied on consecutive clear-sky images from summer 2021 to autumn 2021 on an area of recent grassland revegetation. The estimated FVC maps were plotted and compared to RGB visualization to assess if they show coherent spatial and temporal patterns.
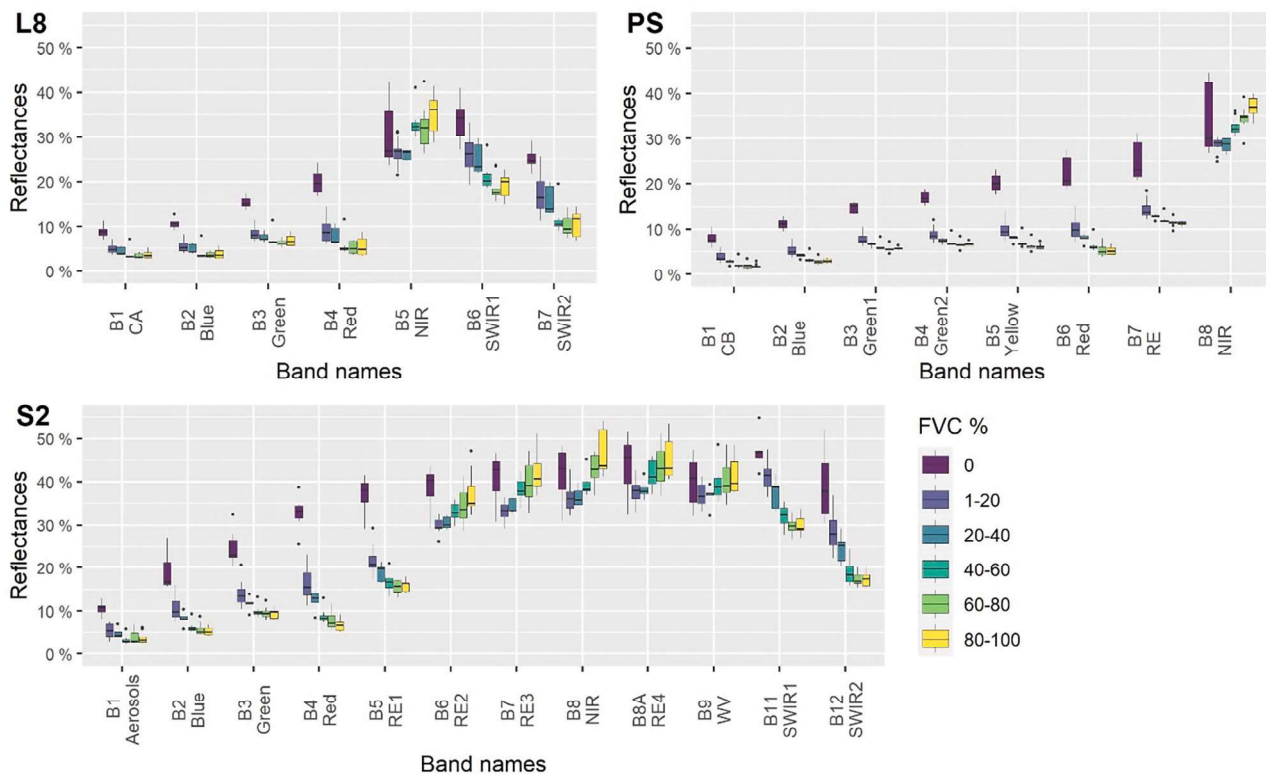
Fig. 2. Boxplot of the spectral values of the plots divided according to FVC% using L8, S2 and PS imagery. See Table S1 for band names abbreviations.
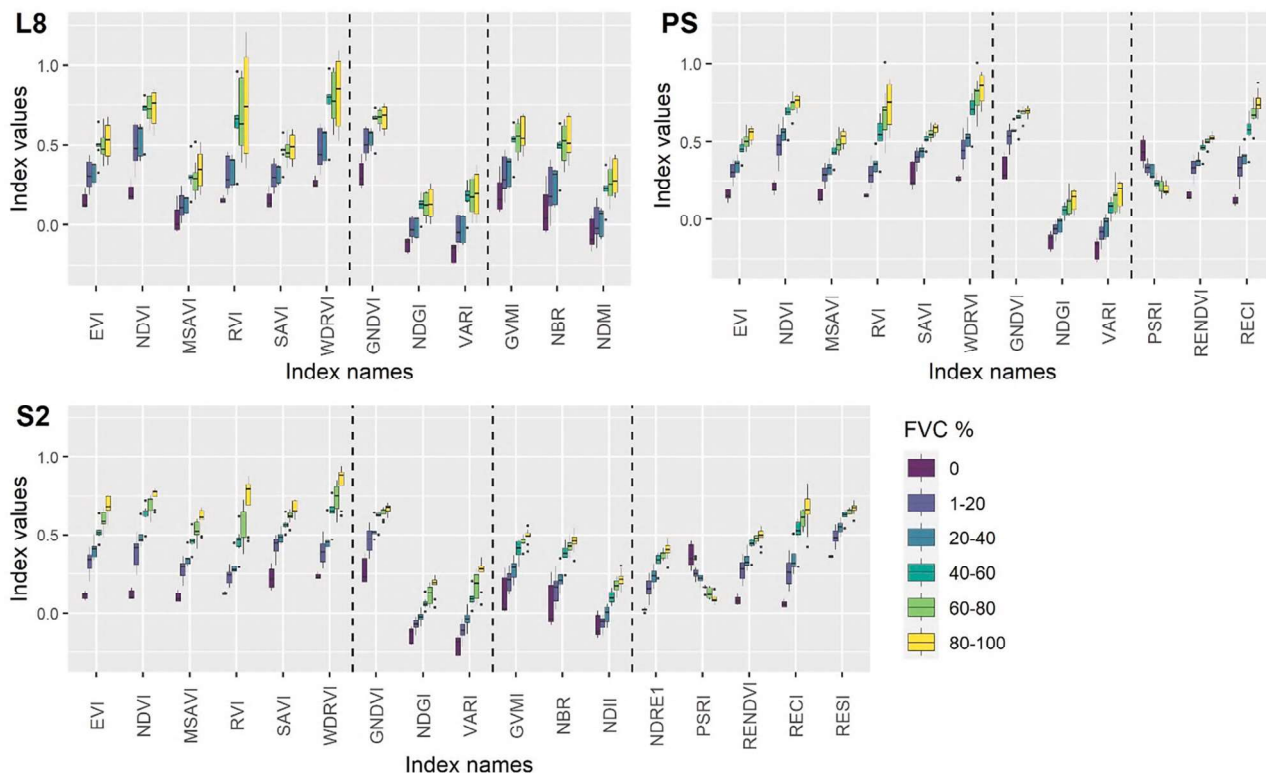

Fig. 3. Vegetation indices values of plots with various FVC. From left to right VIs based on NIR and red wavelength regions (EVI, NDVI, MSAVI, RVI, SAVI, WDRVI), including the green wavelength region (GNDVI, NDGI, VARI), based on SWIR and NIR wavelength regions (GVMI, NBR, NDII, NDMI) and indices based on Red Edge wavelengths (NDRE1, PSRI, RENDVI, RECI, RESI) were presented. RECI values were divided by 10, RENDVI by 3 and 1 was added to WDRVI to fit the figure y axis.

3. Results

3.1. Grasslands FVC spectral signature

Grasslands spectral signature is clearly affected by FVC level and there is great consistency between different satellites (Fig. 2). There is a linear relationship between FVC and reflectance values in the visible and SWIR domain. On the contrary, the NIR wavelength region (~865 nm: SR_B5, B8, b8) and the S2 Red-Edge2 and Red-Edge3 bands (B6 and B7) do not show a linear relationship with FVC along all the FVC gradient: reflectances show a positive correlation with FVC in vegetated plots, but bare soil plots have higher reflectance values and show a much higher variability. The SWIR bands are available only on L8 and S2 imagery (~1610 nm: SR_B6, B11) and are quite informative for low FVC, but tend to saturate at high FVC levels, similarly to red bands imagery (~665 nm: B4, b6).

3.2. Relationship between fractional vegetation cover and vegetation indices

VIs provided a higher separability of FVC categories than bands' reflectances. In addition, VIs relationship with FVC was coherent on the whole FVC gradient, whereas bare soils showed a different pattern from vegetated areas looking at bands' reflectances. The spectral separability of the FVC categories varies among different VIs and imageries, as presented in Fig. 3. Indices based on NIR and red wavelength regions (EVI, NDVI, MSAVI, RVI, SAVI, WDRVI) and on the visible wavelength region (GNDVI, NDGI, VARI) showed a clear relationship to FVC values. Indices based on SWIR and NIR wavelength regions (GVMI, NBR, NDII, NDMI) showed overlapping index values for low FVC levels, whereas indices based on red-edge wavelengths showed a promising identification of bare soils and low-density grassland but tends to saturate at higher FVC (NDRE1, PSRI, RENDVI, RECI, RESI).

In Table 2 the accuracy of FVC prediction models based on VI are presented. VIs derived from S2 and PS imagery showed a higher prediction ability than those based on L8 imagery. The best performing index for S2 imagery was EVI, which showed a strong relationship with FVC ($R^2 = 0.91$). The best performing index using PS imagery was RECI ($R^2 = 0.89$), whereas NDMI gave the highest correlation using L8 imagery ($R^2 = 0.66$) (Fig. 4). L8 model residuals showed a high degree of heteroscedasticity, whereas S2 and PS models residuals were almost homoscedastic (Fig. 4). The residuals of the selected models were regressed against all the other indices and some significant linear or quadratic relationships were found. The addition of a second VI to the selected model, however, led to a very low (<0.01) increase in R^2. No

multiple VI models were therefore selected.

Terrain indices and diversity of FVC across subplots of each plot do not significantly explain the variability of the residuals, as resulting from Pearson's product moment correlation coefficient analysis (level of significance p-value < 0.05).

3.3. Model validation

The relationship between EVI derived from S2 imagery and FVC resulted in an R^2 of 0.911 and in a 0.903 cross validation R^2, whereas the R^2 and cross-validation R^2 for L8 were 0.659 and 0.636 respectively, and 0.895 and 0.886 for PS.

RGB visualization and FVC maps derived from selected S2 and PS models showed coherent spatial patterns, whereas some anomalous values were found in the map derived from the selected L8 model (Fig. 5). In the western and northern areas, the map derived from L8 imagery showed estimated values around 20% FVC, even though the RGB visualization and the estimated map derived from S2 and PS imagery showed bare soils or very low FVC. In addition to this, the great spatial heterogeneity of FVC in the study site is adequately described by S2 and PS spatial resolution, whereas the spatial resolution of L8 imagery (30 m) is not sufficient: in many L8 pixels low- and high-density grasslands are mixed, and forest mixed pixels may occur.

In the temporal change analysis FVC maps derived from S2 and PS imagery showed coherent patterns to RGB visualization and accurately described grassland recovery after soil levelling and sowing for ski runs preparation (Fig. 6). The FVC maps derived from L8 overestimated the grassland cover at the beginning of the season compared to RGB visualization and to maps derived from S2 and PS imageries.

4. Discussion

4.1. Spectral signatures, VIs and their relationship with FVC

Soil and plant spectral signature identification and discrimination may not be straightforward using raw spectral band reflectances, but VIs may accentuate the spectral distinctness. The understanding of soil and plant spectral features is fundamental for FVC prediction, but there is not always a clear linear relationship between reflectances and FVC on the whole FVC gradient. While in vegetated plots FVC seems to play a major role, the spectral signature of bare plots is much more variable and has been attributed to the combined effect of their origin, parental material, structure, mineralogy, water content and organic matter content (Fabre et al., 2015; Lausch et al., 2019; Mulder et al., 2011; Wilson et al., 2017; Xu et al., 2020). In our case study, we observed that the spectral signature changes along the FVC gradient following specific patterns. In the first stages of the revegetation process the high reflectance value of bare soils in the visible and NIR wavelength regions decrease, probably due to plant shadowing effect and plant spectral signature, and partly due to the increase of soil organic matter content and soil water-holding capacity (Bartholomeus et al., 2008; Fabre et al., 2015). In the later stages of the revegetation plants spectral signature plays a major role and soils diversity is almost hidden. At high FVC levels, reflectances in the blue (450 nm) and red (670 nm) regions further strongly decrease due to high plant chlorophyll absorption resulting in higher reflectances than in low covered areas (Govender et al., 2009).

Since raw bands values do not always allow spectral distinctness, researchers identified several band differences and ratios that were found to accentuate spectral distinctness and developed VIs based on these findings (Xue and Su, 2017). One common observation is that the difference between NIR and red reflectance for soil is much less than for live vegetation (Huete, 1988; Rouse et al., 1974). In our case study VIs based on the difference between NIR and red wavelength regions (EVI, NDVI, MSAVI, RVI, SAVI, WDRVI) confirmed their high correlation to FVC and their robustness in the correct identification of bare soils, as
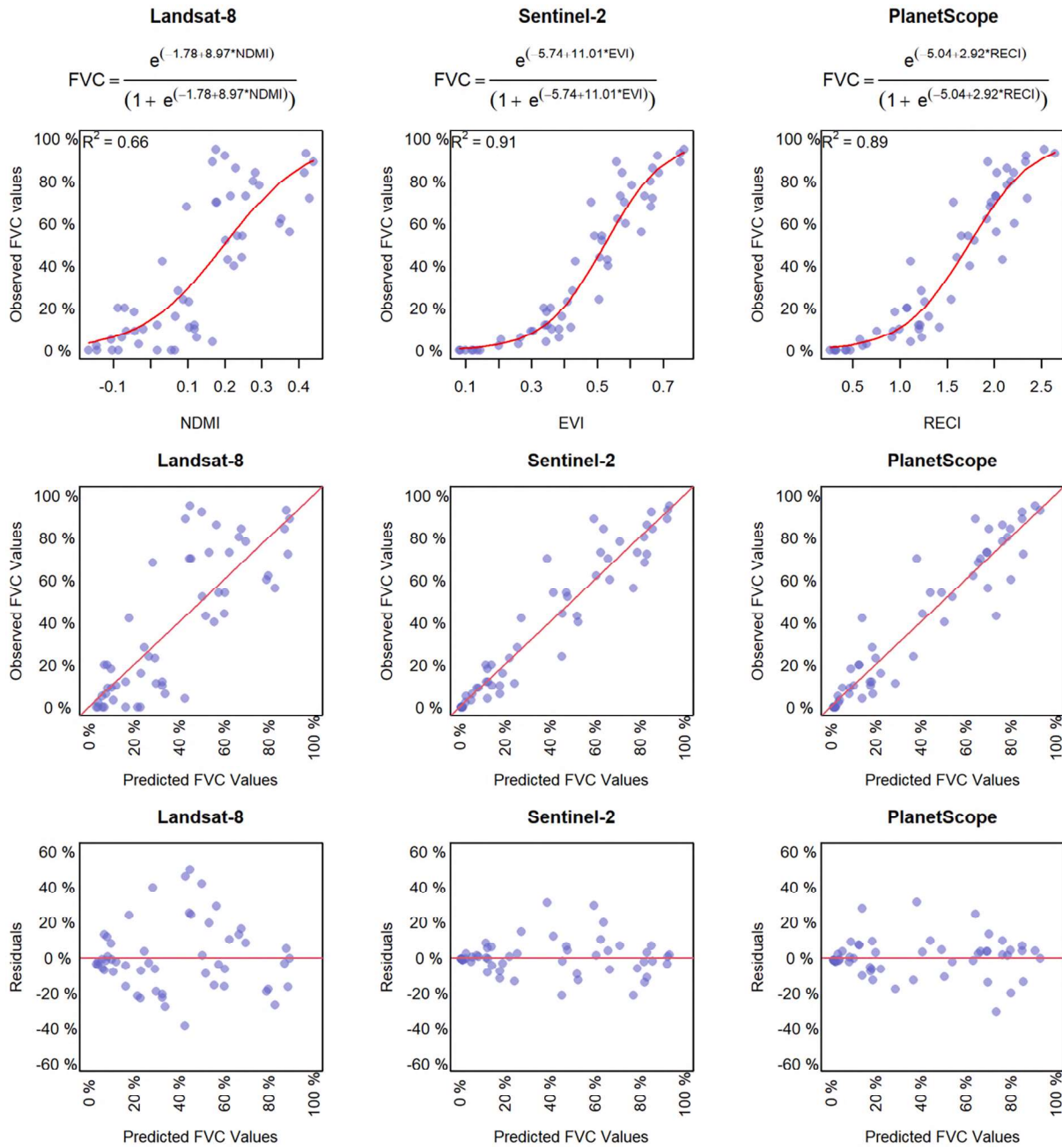
Table 2
Accuracy (R^2) of Fractional Response Models. The best model for each imagery is highlighted in green.

Index	Spectral region of interest	Landsat-8	Sentinel-2	PlanetScope
EVI	NIR and Red included	0.585	0.911	0.881
NDVI		0.556	0.878	0.844
MSAVI		0.558	0.893	0.875
RVI		0.506	0.839	0.822
SAVI		0.589	0.896	0.881
WDRVI		0.536	0.840	0.839
GNDVI	Green included	0.564	0.794	0.823
NDGI		0.516	0.864	0.813
VARI		0.517	0.870	0.821
GVMI	SWIR, NIR	0.606	0.869	–
NBR		0.605	0.819	–
NDII		–	0.902	–
NDMI		0.659	–	–
NDRE1	Red-Edge included	–	0.851	–
PSRI		–	0.895	0.805
RENDVI		–	0.823	0.893
RECI		–	0.821	0.895
RESI		–	0.852	–

Fig. 4. Reference FVC values plotted against values estimated using selected prediction models derived from Landsat-8, Sentinel-2 and PlanetScope imagery and against models' residuals.

reported in previous literature (Chen et al., 2016; Jia et al., 2017; Kim et al., 2020; Mao et al., 2022). EVI was selected as the best performing index for S2 imagery. VARI and NDGI, that are based on the visible spectral domain, were used just twice for FVC estimation (Jiménez-Muñoz et al., 2009; Zhou et al., 2014) and in our case study showed a strong relationship with FVC ($R^2 = 0.864$ for NDGI, and 0.870 for VARI using S2 imagery). The good performance of these indices is promising since the visible domain is the most common wavelength region and may benefit from future further improvements of spatial and temporal resolution (Dubovik et al., 2021; Garzaniti et al., 2021). The red-edge spectral bands are available only for S2 and PS imagery and the derived indices tested (NDRE1, PSRI, RENDVI, RECI and RESI) have been indicated as promising by previous literature (Gao et al., 2020; Gitelson, 2013; Liu et al., 2007). In our case study these indices showed very good performances. Even though they tend to saturate in very

dense grasslands, we obtained high accuracies and RECI was selected as the best performing index for PS imagery. Indices based on SWIR and NIR wavelength regions (GVMI, NBR, NDII, NDMI) are typically used for the analysis of vegetation moisture content, but NDII was found to be strictly correlated to FVC as it outperformed other indices in a mowing detection algorithm (Andreatta et al., 2022). In our case study, however, only using L8 imagery the relationship between NDMI and FVC resulted in the highest R^2, but the model showed heteroscedasticity in the residuals (Fig. 4) and performed badly at the spatial change analysis (Fig. 5, see subsection 4.2 for discussion).

The observed heteroscedasticity of L8 model residuals is caused by high residual standard deviation for FVC predicted values in the mid-range. Three plots which showed very high positive residuals (plot 18, 32 and 4) have high reference FVC, but they are contiguous to areas with very low vegetation cover. The mixed spectral signature of the pixel in
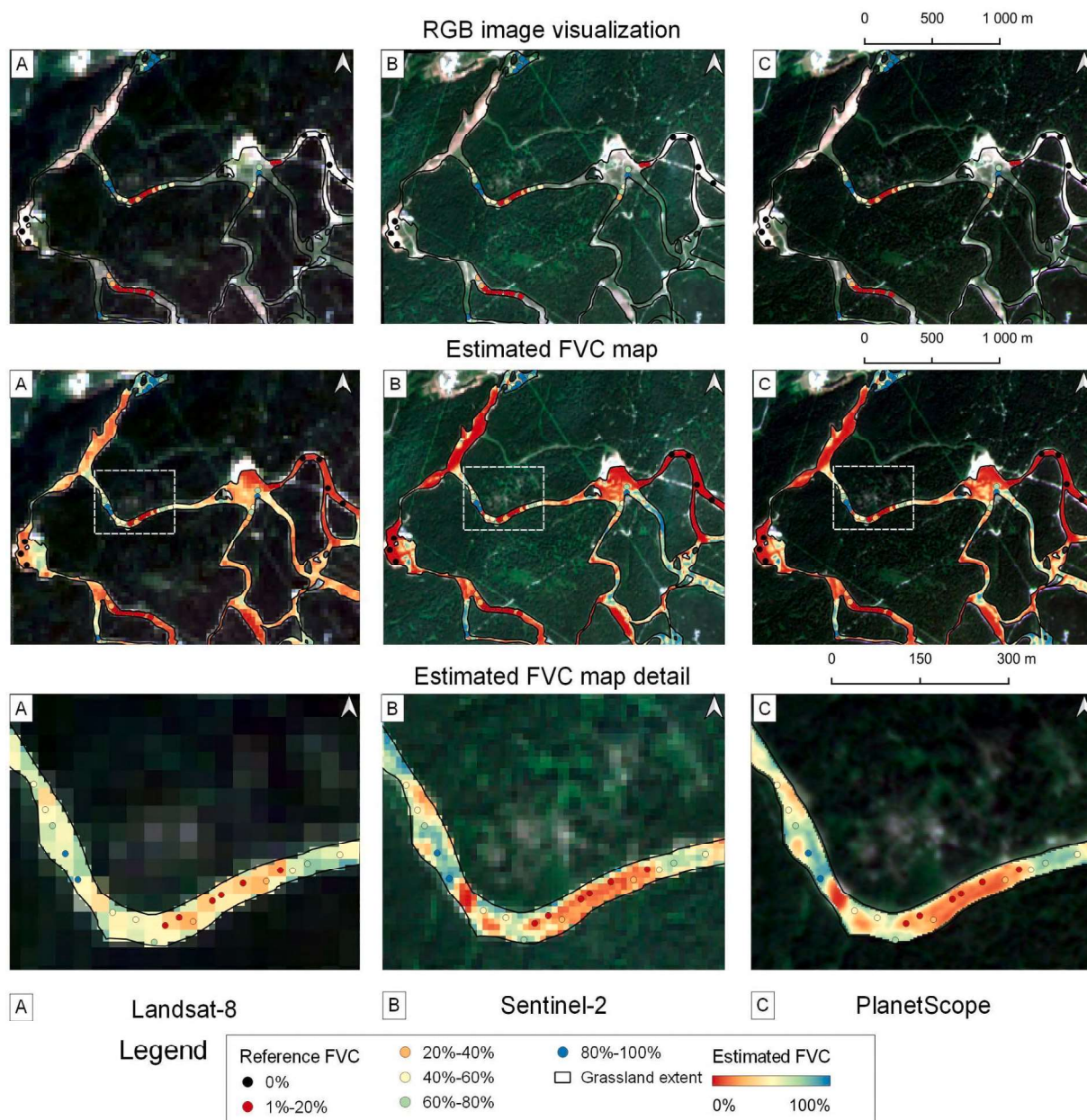
Fig. 5. FVC spatial change analysis. RGB imagery, estimated FVC map and estimated FVC map detail obtained using the best prediction model based on L8, S2, and PS imagery.

which these plots are located results in an estimated FVC in the mid-range. The opposite happens for plots 36, 37, 39, 40 and 41 which show large negative residuals, as the plots are scarcely vegetated, but inside their pixels there are areas covered by bushes and small trees. The mixed spectral signature also in this case results in an estimated FVC in the mid-range, but in large negative residuals. The absence of large residuals for low and high estimated FVC may be explained: their NDMI values are coherent with values attributed to plots located in pure pixels. On the contrary, NDMI values in the mid-range in some cases result as an average of high and low FVC areas inside the pixels. The absence of any significant relationship between residuals of L8 model and variability of FVC across subplots of each plot can be related to L8 imagery resolution: even though some L8 pixels (30 m × 30 m) included heterogeneous vegetations (high model residuals), the plots used to describe them in the field (10 m × 10 m) were vegetationally homogeneous (low standard deviation of FVC across subplot).

In our case study the addition of a second VI to the FVC prediction

model did not increase the accuracy (increase in $R^2 < 0.01$) and was therefore not applied. The addition of several indices to FVC prediction models is not common, but has been explored, for example by Guerschman et al. (2009).

4.2. Model validation

Cross validated statistics and spatiotemporal change analysis of FVC assessed the good generalization capability of the selected S2 and PS models but raised some concerns regarding the L8 model. Cross validated statistics were just slightly lower than accuracy metrics obtained on the whole calibration dataset (Table S2), and the estimated FVC derived from S2 and PS imagery maps and RGB visualization showed coherent spatial patterns. Two factors related to the spatial resolution of the L8 imagery probably affected the L8 model reliability. Firstly, the calibration plot size (10 m × 10 m) was not sufficient to describe the vegetation of the whole L8 pixel, so a not representative reference FVC is
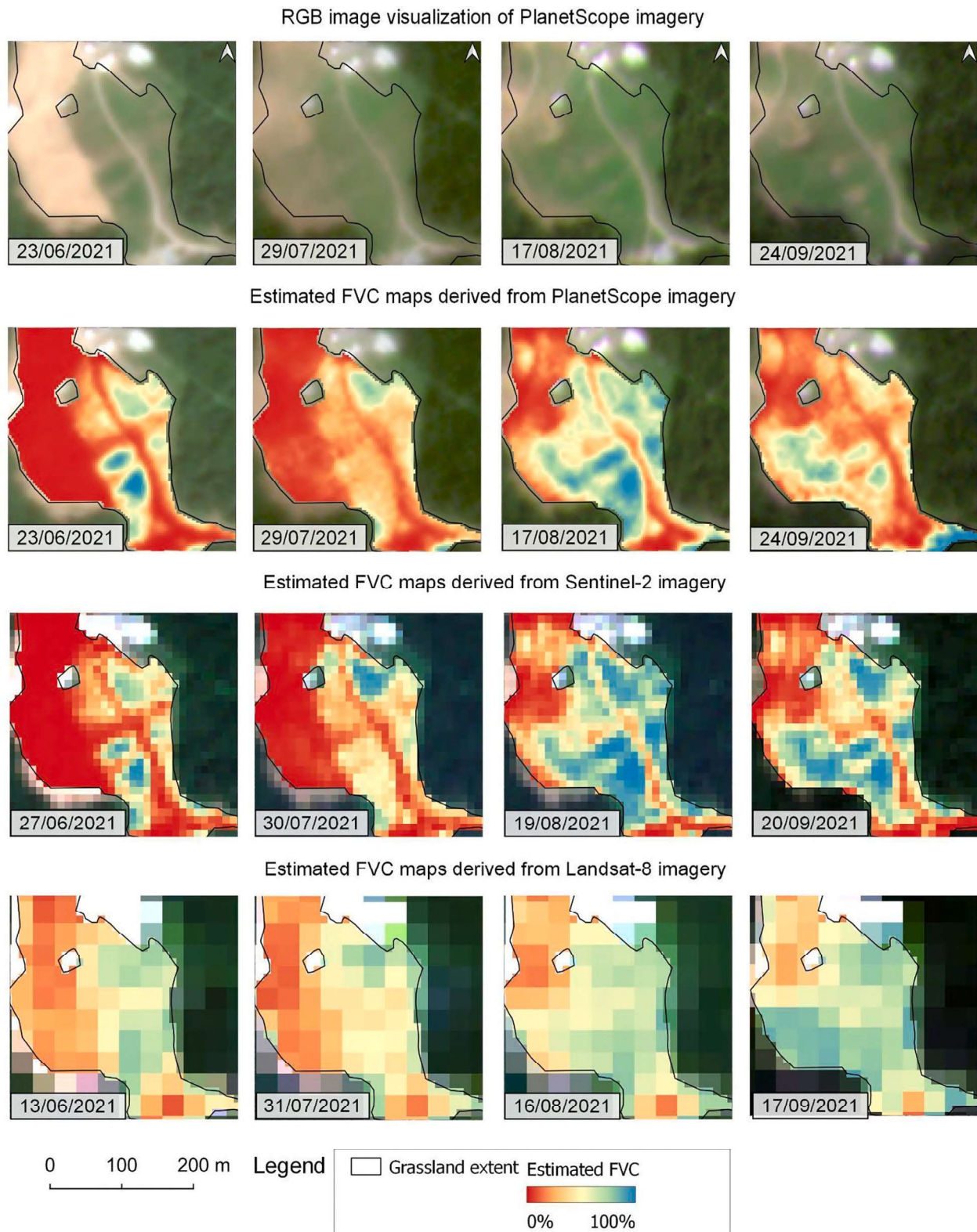
Fig. 6. FVC temporal change analysis. RGB visualization (PS imagery) and estimated FVC map computed using best PS, S2 and L8 prediction models for 4 consequent clear-sky images of grasslands recovering after soil levelling and sowing for ski runs preparation.

assigned to mixed pixels. The L8 model is therefore trained with misleading data, resulting in a heteroscedastic distribution of the residuals, in erroneous prediction of the bare soil areas in the west and north areas of the study site (Fig. 5) and in an overestimation of the frequency of FVC values in the mid-range (Fig. 4). Secondly, in our study

site FVC changes at a very fine spatial scale, so that the coarser spatial resolution of L8 imagery (30 m) is not sufficient at describing it, and even if 30 m × 30 m reference FVC was available, locally extreme FVC would be averaged at pixel scale. While L8 model performance was not satisfying, as already discussed, S2 and PS imagery provided coherent

results and especially PS imagery derived FVC maps provided a much finer description of FVC distribution in space.

The temporal change analysis was used to assess the reliability of the selected models when applied on different images and confirmed their robustness.

5. Conclusions

In this study we assessed that S2 and PS imagery can successfully be used to estimate grassland FVC in areas where it changes at a very fine scale, thanks to their high spatial resolution and to the availability of the red-edge wavelength region. Previously available imagery at medium to low spatial and temporal resolution (e.g. L8) may still be interesting for analysis requiring long time-series, since long-term FVC data is a useful indicator of land degradation and recovery processes, especially for vast agricultural and natural grasslands. However, for local hotspots of degradation and recovery, high-resolution FVC estimated from S2 and PS imagery would be useful to examine the spatial and temporal patterns patches better than the mid- or coarse-resolution satellite data. The selected models should be carefully applied to areas different from the study site since soil reflectance depends on multiple factors and significantly affects the pixel spectral signature in areas with low FVC.

CRediT authorship contribution statement

Davide Andreatta: Conceptualization, Formal analysis, Investigation, Software, Writing – original draft, Writing – review & editing. **Damiano Gianelle:** Conceptualization, Resources, Funding acquisition, Writing – review & editing, Supervision. **Michele Scotton:** Conceptualization, Resources, Funding acquisition, Writing – review & editing, Supervision. **Michele Dalponte:** Conceptualization, Software, Writing – review & editing, Supervision.

Declaration of Competing Interest

The authors declare that they have no known competing financial interests or personal relationships that could have appeared to influence the work reported in this paper.

Data availability

Field fractional vegetation cover data and location are provided in KML format as supplementary materials, imageries can be accessed through the Planet website (https://www.planet.com) and through the Earth Engine Data Catalog (https://developers.google.com/earth-engine/datasets).

Appendix A. Supplementary data

Supplementary data to this article can be found online at https://doi.org/10.1016/j.ecolind.2022.109102. These data include Google maps of the most important areas described in this article.

References

Andreatta, D., Gianelle, D., Scotton, M., Vescovo, L., Dalponte, M., 2022. Detection of grassland mowing frequency using time series of vegetation indices from Sentinel-2 imagery. GIScience Remote Sens. 59 (1), 481–500. https://doi.org/10.1080/15481603.2022.2036055.

Atzberger, C., 2004. Object-based retrieval of biophysical canopy variables using artificial neural nets and radiative transfer models. Remote Sens. Environ. 93 (1–2), 53–67. https://doi.org/10.1016/J.RSE.2004.06.016.

Baret, F., Hagolle, O., Geiger, B., Bicheron, P., Miras, B., Huc, M., Berthelot, B., Niño, F., Weiss, M., Samain, O., Roujean, J.L., Leroy, M., 2007. LAI, fAPAR and fCover CYCLOPES global products derived from VEGETATION. Remote Sens. Environ. 110 (3), 275–286. https://doi.org/10.1016/j.rse.2007.02.018.

Bartholomeus, H.M., Schaepman, M.E., Kooistra, L., Stevens, A., Hoogmoed, W.B., Spaargaren, O.S.P., 2008. Spectral reflectance based indices for soil organic carbon quantification. Geoderma 145 (1–2), 28–36. https://doi.org/10.1016/j.geoderma.2008.01.010.

Booth, D.T., Cox, S.E., Berryman, R.D., 2006. Point sampling digital imagery with 'Samplepoint'. Environ. Monit. Assess. 123 (1–3), 97–108. https://doi.org/10.1007/s10661-005-9164-7.

Booth, T.D., Cox, S.E., Fifield, C., Phillips, M., Williamson, N., Booth, D.T., Cox, S.E., Fifield, C., Phillips, M., Willlamson, N., 2005. Image analysis compared with other methods for measuring ground cover. Arid Land Res. Manage. 19 (2), 91–100. https://doi.org/10.1080/15324980590916486.

Ceccato, P., Gobron, N., Flasse, S., Pinty, B., Tarantola, S., 2002. Designing a spectral index to estimate vegetation water content from remote sensing data: Part 1: Theoretical approach. Remote Sens. Environ. 82 (2-3), 188–197.

Chen, J., Yi, S., Qin, Y., Wang, X., 2016. Improving estimates of fractional vegetation cover based on UAV in alpine grassland on the Qinghai-Tibetan Plateau. Int. J. Remote Sens. 37 (8), 1922–1936. https://doi.org/10.1080/01431161.2016.1165884.

Courel, M.-F., Chamard, P., Guenegou, M., Lerhun, J., Levasseur, J., Togola, M., 1991. Utilisation des bandes spectrales du vert et du rouge pour une meilleure évaluation des formations végétales actives. Télédétection et Cartographie 203–209. https://hal.archives-ouvertes.fr/hal-00327879.

Darvishzadeh, R., Skidmore, A., Schlerf, M., Atzberger, C., 2008. Inversion of a radiative transfer model for estimating vegetation LAI and chlorophyll in a heterogeneous grassland. Remote Sens. Environ. 112 (5), 2592–2604. https://doi.org/10.1016/j.rse.2007.12.003.

Dubovik, O., Schuster, G.L., Xu, F., Hu, Y., Bösch, H., Landgraf, J., Li, Z., 2021. Grand challenges in satellite remote sensing. Front. Remote Sens. 2, 1. https://doi.org/10.3389/frsen.2021.619818.

Fabre, S., Briottet, X., Lesaignoux, A., 2015. Estimation of soil moisture content from the spectral reflectance of bare soils in the 0.4–2.5 µm domain. Sensors 15 (2), 3262–3281. https://doi.org/10.3390/s150203262.

Gang, C., Zhou, W., Chen, Y., Wang, Z., Sun, Z., Li, J., Qi, J., Odeh, I., 2014. Quantitative assessment of the contributions of climate change and human activities on global grassland degradation. Environ. Earth Sci. 72 (11), 4273–4282. https://doi.org/10.1007/S12665-014-3322-6/FIGURES/5.

Gao, L., Wang, X., Johnson, B.A., Tian, Q., Wang, Y., Verrelst, J., Mu, X., Gu, X., 2020. Remote sensing algorithms for estimation of fractional vegetation cover using pure vegetation index values: a review. ISPRS J. Photogramm. Remote Sens. 159, 364–377. https://doi.org/10.1016/j.isprsjprs.2019.11.018.

García, M.J.L., Caselles, V., 1991. Mapping burns and natural reforestation using thematic Mapper data. Geocarto International 6 (1), 31–37. https://doi.org/10.1080/10106049109354290.

Garzaniti, N., Tekic, Z., Kukolj, D., Golkar, A., 2021. Review of technology trends in new space missions using a patent analytics approach. Prog. Aerosp. Sci. 125, 100727 https://doi.org/10.1016/j.paerosci.2021.100727.

Gitelson, A.A., 2001. Non-destructive and remote sensing techniques for estimation of vegetation status. Papers in Natural Resources 273. https://digitalcommons.unl.edu/natrespapers.

Gitelson, A.A., 2004. Wide dynamic range vegetation index for remote quantification of biophysical characteristics of vegetation. J. Plant Physiol. 161 (2), 165–173. https://doi.org/10.1078/0176-1617-01176.

Gitelson, A.A., 2013. Remote estimation of crop fractional vegetation cover: the use of noise equivalent as an indicator of performance of vegetation indices. Int. J. Remote Sens. 34 (17), 6054–6066. https://doi.org/10.1080/01431161.2013.793868.

Gitelson, A.A., Gritz †, Y., Merzlyak, M.N., 2003. Relationships between leaf chlorophyll content and spectral reflectance and algorithms for non-destructive chlorophyll assessment in higher plant leaves. J. Plant Physiol. 160 (3), 271–282.

Gitelson, A.A., Kaufman, Y.J., Merzlyak, M.N., 1996. Use of a green channel in remote sensing of global vegetation from EOS-MODIS. Remote Sens. Environ. 58 (3), 289–298. https://doi.org/10.1016/S0034-4257(96)00072-7.

Gitelson, A., Merzlyak, M.N., 1994. Quantitative estimation of chlorophyll-a using reflectance spectra: experiments with autumn chestnut and maple leaves. J. Photochem. Photobiol., B 22 (3), 247–252. https://doi.org/10.1016/1011-1344(93)06963-4.

Gorelick, N., Hancher, M., Dixon, M., Ilyushchenko, S., Thau, D., Moore, R., 2017. Google Earth Engine: planetary-scale geospatial analysis for everyone. Remote Sens. Environ. 202, 18–27. https://doi.org/10.1016/j.rse.2017.06.031.

Govender, M., Chetty, K., Bulcock, H., 2009. A review of hyperspectral remote sensing and its application in vegetation and water resource studies. Water SA 33 (2), 145–151. https://doi.org/10.4314/wsa.v33i2.49049.

Graetz, R.D., Pech, R.P., Davis, A.W., 1988. The assessment and monitoring of sparsely vegetated rangelands using calibrated Landsat data. Int. J. Remote Sens. 9 (7), 1201–1222. https://doi.org/10.1080/01431168808954929.

Guerschman, J.P., Hill, M.J., Renzullo, L.J., Barrett, D.J., Marks, A.S., Botha, E.J., 2009. Estimating fractional cover of photosynthetic vegetation, non-photosynthetic vegetation and bare soil in the Australian tropical savanna region upscaling the EO-1 Hyperion and MODIS sensors. Remote Sens. Environ. 113 (5), 928–945. https://doi.org/10.1016/J.RSE.2009.01.006.

Hardisky, M., Klemas, V., Smart, M., 1983. The influence of soil salinity, growth form, and leaf moisture on the spectral radiance of Spartina alterniflora canopies. Photogramm. Eng. Remote Sens. 49, 77–83.

Hijmans, R.J., 2021. raster: Geographic Data Analysis and Modeling. https://cran.r-project.org/package=raster.

Huete, A., 1988. A soil-adjusted vegetation index (SAVI). Remote Sens. Environ. 25 (3), 295–309. https://doi.org/10.1016/0034-4257(88)90106-X.

Huete, A., Didan, K., Miura, T., Rodriguez, E., Gao, X., Ferreira, L., 2002. Overview of the radiometric and biophysical performance of the MODIS vegetation indices. Remote Sens. Environ. 83 (1–2), 195–213. https://doi.org/10.1016/S0034-4257(02)00096-2.

Jáuregui, J.M., Delbino, F.G., Brance Bonvini, M.I., Berhongaray, G., 2019. Determining yield of forage crops using the Canopeo mobile phone app. J. New Zealand Grasslands 81, 41–46. https://doi.org/10.33584/JNZG.2019.81.385.

Jia, K., Li, Y., Liang, S., Wei, X., Yao, Y., 2017. Combining estimation of green vegetation fraction in an arid region from Landsat 7 ETM+ data. Remote Sensing 9 (11), 1121. https://doi.org/10.3390/rs9111121.

Jiménez-Muñoz, J., Sobrino, J., Plaza, A., Guanter, L., Moreno, J., Martinez, P., 2009. Comparison between fractional vegetation cover retrievals from vegetation indices and spectral mixture analysis: case study of PROBA/CHRIS data over an agricultural area. Sensors 9 (2), 768–793. https://doi.org/10.3390/s90200768.

Jordan, C.F., 1969. Derivation of leaf-area index from quality of light on the forest floor. Ecology 50 (4), 663–666. https://doi.org/10.2307/1936256.

Kim, J., Kang, S., Seo, B., Narantsetseg, A., Han, Y., 2020. Estimating fractional green vegetation cover of Mongolian grasslands using digital camera images and MODIS satellite vegetation indices. GIScience Remote Sens. 57 (1), 49–59. https://doi.org/10.1080/15481603.2019.1662166.

Lausch, A., Baade, J., Bannehr, L., Borg, E., Bumberger, J., Chabrilliat, S., Dietrich, P., Gerighausen, H., Glässer, C., Hacker, J., Haase, D., Jagdhuber, T., Jany, S., Jung, A., Karnieli, A., Kraemer, R., Makki, M., Mielke, C., Möller, M., Mollenhauer, H., Montzka, C., Pause, M., Rogass, C., Rozenstein, O., Schmullius, C., Schrodt, F., Schrön, M., Schulz, K., Schütze, C., Schweitzer, C., Selsam, P., Skidmore, A., Spengler, D., Thiel, C., Truckenbrodt, S., Vohland, M., Wagner, R., Weber, U., Werban, U., Wollschläger, U., Zacharias, S., Schaepman, M., 2019. Linking remote sensing and geodiversity and their traits relevant to biodiversity—Part I: Soil characteristics. Remote Sensing 11 (20), 2356.

Li, T., Cui, L., Scotton, M., Dong, J., Xu, Z., Che, R., Tang, Li., Cai, S., Wu, W., Andreatta, D., Wang, Y., Song, X., Hao, Y., Cui, X., 2022. Characteristics and trends of grassland degradation research. J. Soils Sediments 22 (7), 1901–1912.

Li, X.-B., Chen, Y.-H., Yang, H., Zhang, Y.-X., 2005. Improvement, comparison, and application of field measurement methods for grassland vegetation fractional coverage. J. Integr. Plant Biol. 47 (9), 1074–1083. https://doi.org/10.1111/j.1744-7909.2005.00134.x.

Liang, S., & Wang, J. (2020). Fractional vegetation cover. In Academic Press (Ed.), Advanced Remote Sensing (Second edi, pp. 477–510). Elsevier. doi: 10.1016/B978-0-12-815826-5.00012-X.

Liu, Z.-Y., Huang, J.-F., Wu, X.-H., Dong, Y.-P., 2007. Comparison of vegetation indices and red-edge parameters for estimating grassland cover from canopy reflectance data. J. Integr. Plant Biol. 49 (3), 299–306.

Lollato, R.P., Ochsner, T.E., Arnall, D.B., Griffin, T.W., Edwards, J.T., 2019. From field experiments to regional forecasts: upscaling wheat grain and forage yield response to acidic soils. Agron. J. 111 (1), 287–302. https://doi.org/10.2134/AGRONJ2018.03.0206.

Mao, P., Zhang, J., Li, M., Liu, Y., Wang, X., Yan, R., Shen, B., Zhang, X., Shen, J., Zhu, X., Xu, D., Xin, X., 2022. Spatial and temporal variations in fractional vegetation cover and its driving factors in the Hulun Lake region. Ecol. Ind. 135, 108490 https://doi.org/10.1016/J.ECOLIND.2021.108490.

McCallum, J. B., 2000. SigmaScan Pro 5.0. Science, 289(5478), 412–412. https://go.gale.com/ps/i.do?p=HRCA&sw=w&issn=00368075&v=2.1&it=r&id=GALE%7CA63940621&sid=googleScholar&linkaccess=fulltext.

McGwire, K., Minor, T., Fenstermaker, L., 2000. Hyperspectral mixture modeling for quantifying sparse vegetation cover in arid environments. Remote Sens. Environ. 72 (3), 360–374. https://doi.org/10.1016/S0034-4257(99)00112-1.

Merzlyak, M.N., Gitelson, A.A., Chivkunova, O.B., Rakitin, V.Y., 1999. Non-destructive optical detection of pigment changes during leaf senescence and fruit ripening. Physiol. Plant. 106 (1), 135–141. https://doi.org/10.1034/J.1399-3054.1999.106119.X.

Mulder, V.L., de Bruin, S., Schaepman, M.E., Mayr, T.R., 2011. The use of remote sensing in soil and terrain mapping – a review. Geoderma 162 (1–2), 1–19. https://doi.org/10.1016/j.geoderma.2010.12.018.

PAT. (2016). Digital terrain model for hydrological applications. Provincia Autonoma di Trento. https://siat.provincia.tn.it/geonetwork/srv/ita/catalog.search;jsessionid=2FC489233B879F0A43023ECDAAFF5286#/metadata/p_TN:d6472d5e-94b7-456e-b633-0bf19daf6cdf.

Patrignani, A., Ochsner, T.E., 2015. Canopeo: a powerful new tool for measuring fractional green canopy cover. Agron. J. 107 (6), 2312–2320. https://doi.org/10.2134/agronj15.0150.

Qi, J., Chehbouni, A., Huete, A.R., Kerr, Y.H., Sorooshian, S., 1994. A modified soil adjusted vegetation index. Remote Sens. Environ. 48 (2), 119–126. https://doi.org/10.1016/0034-4257(94)90134-1.

Ramalho, J. J. S., 2019. Modeling fractional responses using R (pp. 245–279). doi: 10.1016/bs.host.2018.11.008.

Reynolds, S., Frame, J., 2005. Grasslands: Developments, Opportunities, Perspectives. Publishers, Science.

Roujean, J.L., Lacaze, R., 2002. Global mapping of vegetation parameters from POLDER multiangular measurements for studies of surface-atmosphere interactions: a pragmatic method and its validation. J. Geophys. Res.: Atmos. 107 (D12), ACL-6. https://doi.org/10.1029/2001JD000751.

Rouse, J.W., Haas, R., Schell, J., Deering, D., 1974. Monitoring vegetation systems in the Great Plains with ERTS. NASA Special Publication 351 (1974), 309.

RStudio Team. (2020). RStudio: Integrated Development Environment for R. http://www.rstudio.com/.

Sboarina, C., & Cescatti, A. (2004). Il clima del Trentino–distribuzione spaziale delle principali variabili climatiche Report 33. https://www.fmach.it/Servizi-Generali/Editoria/Il-clima-del-Trentino-distribuzione-spaziale-delle-principali-variabili-climatiche.

van der Meer, F., 1999. Image classification through spectral unmixing. In: Spatial Statistics for Remote Sensing. Springer, pp. 185–193.

Verrelst, J., Muñoz, J., Alonso, L., Delegido, J., Rivera, J.P., Camps-Valls, G., Moreno, J., 2012. Machine learning regression algorithms for biophysical parameter retrieval: Opportunities for Sentinel-2 and -3. Remote Sens. Environ. 118, 127–139. https://doi.org/10.1016/j.rse.2011.11.002.

Wang, B., Waters, C., Orgill, S., Cowie, A., Clark, A., Li Liu, D., Simpson, M., McGowen, I., Sides, T., 2018. Estimating soil organic carbon stocks using different modelling techniques in the semi-arid rangelands of eastern Australia. Ecol. Ind. 88, 425–438. https://doi.org/10.1016/J.ECOLIND.2018.01.049.

White, M.A., Asner, G.P., Nemani, R.R., Privette, J.L., Running, S.W., 2000. Measuring fractional cover and leaf area index in arid ecosystems: digital camera, radiation transmittance, and laser altimetry methods. Remote Sens. Environ. 74 (1), 45–57. https://doi.org/10.1016/S0034-4257(00)00119-X.

Wilson, C.H., Caughlin, T.T., Rifai, S.W., Boughton, E.H., Mack, M.C., Flory, A.S.L., 2017. Multi-decadal time series of remotely sensed vegetation improves prediction of soil carbon in a subtropical grassland. Ecol. Appl. 27 (5), 1646–1656. http://www.jstor.org/stable/26294514.

Wilson, M.F.J., O'Connell, B., Brown, C., Guinan, J.C., Grehan, A.J., 2007. Multiscale terrain analysis of multibeam bathymetry data for habitat mapping on the continental slope. Mar. Geod. 30 (1–2), 3–35. https://doi.org/10.1080/01490410701295962.

Xiao, C., Li, P., Feng, Z., Liu, Y., Zhang, X., 2020. Sentinel-2 red-edge spectral indices (RESI) suitability for mapping rubber boom in Luang Namtha Province, northern Lao PDR. Int. J. Appl. Earth Obs. Geoinf. 93, 102176 https://doi.org/10.1016/J.JAG.2020.102176.

Xu, C., Qu, J.J., Hao, X., Wu, D., 2020. Monitoring surface soil moisture content over the vegetated area by integrating optical and SAR satellite observations in the permafrost region of Tibetan Plateau. Remote Sensing 12 (1). https://doi.org/10.3390/RS12010183.

Xue, J., Su, B., 2017. Significant remote sensing vegetation indices: a review of developments and applications. J. Sensors 2017, 1–17.

Zarei, A., Asadi, E., Ebrahimi, A., Jafari, M., Malekian, A., Mohammadi Nasrabadi, H., Chemura, A., Maskell, G., 2020. Prediction of future grassland vegetation cover fluctuation under climate change scenarios. Ecol. Ind. 119, 106858. https://linkinghub.elsevier.com/retrieve/pii/S1470160X20307962.

Zhou, Q., Robson, M., Pilesjo, P., 1998. On the ground estimation of vegetation cover in Australian rangelands. Int. J. Remote Sens. 19 (9), 1815–1820. https://doi.org/10.1080/014311698215261.

Zhou, Y., Zhang, L., Xiao, J., Chen, S., Kato, T., Zhou, G., 2014. A comparison of satellite-derived vegetation indices for approximating gross primary productivity of grasslands. Rangeland Ecol. Manage. 67, 9–18. https://doi.org/10.2111/REM-D-13-00059.1.

Study II

Detection of grassland mowing frequency using time series of vegetation indices from Sentinel-2 imagery

Davide Andreatta, Damiano Gianelle, Michele Scotton, Loris Vescovo, Michele Dalponte

Taylor & Francis
Taylor & Francis Group

RESEARCH ARTICLE

Detection of grassland mowing frequency using time series of vegetation indices from Sentinel-2 imagery

Davide Andreatta [ID][a,b], Damiano Gianelle [ID][b], Michele Scotton [ID][a], Loris Vescovo [ID][b] and Michele Dalponte [ID][b]

[a]Department of Agronomy, Food, Natural Resources, Animals and Environment, University of Padova, Legnaro, Padova, Italy; [b]Department of Sustainable Agro-Ecosystems and Bioresources, Research and Innovation Centre, Fondazione Edmund Mach, San Michele all'Adige, Trento, Italy

ABSTRACT

Management intensity deeply influences meadow structure and functioning, therefore affecting grassland ecosystem services. Conservation and management measures, including European Common Agricultural Policy subsidies, should therefore be based on updated and publicly available data about management intensity. The mowing frequency is a crucial trait to describe meadows management intensity, but the potential of using vegetation indices from Sentinel-2 imagery for its retrieval has not been fully exploited. In this work we developed on the Google Earth Engine platform a four-phases algorithm to identify mowing frequency, including i) vegetation index time-series computing, ii) smoothing and resampling, iii) mowing detection, and iv) majority analysis. Mowing frequency during 2020 of 240 ha of grassland fields in the Italian Alps was used for algorithm optimization and evaluation. Six vegetation indexes (EVI, GVMI, MTCI, NDII, NDVI, RENDVI$_{783.740}$) were tested as input to the proposed algorithm. The Normalized Difference Infrared Index (NDII) showed the best performance, resulting in mean absolute error of 0.07 and 93% overall accuracy on average at the four sites used for optimization, at pixel resolution. A slightly lower accuracy (mean absolute error = 0.10, overall accuracy = 90%) was obtained aggregating the maps to management parcels. The algorithm showed a good generalization ability, with a similar performance between global and local optimization and an average mean absolute error of 0.12 and an overall accuracy of 89% on average on the sites not used for parameters optimization. The lowest accuracies occurred in intensively managed grasslands surveyed by one satellite orbit only. This study demonstrates the suitability of the proposed algorithm to monitor very fragmented grasslands in complex mountain ecosystems. Google Earth Engine was used to develop the model and will enable researchers, agencies and practitioners to easily and quickly apply the code to map grassland mowing frequency for extensive grasslands protection and conservation, for mowing event verification, or for forage system characterization.

1. Introduction

Grasslands are one of the most widespread ecosystems and they are rapidly changing in extent, structure, and functioning (Zarei et al. 2020; Tasser et al. 2007; Scotton, Sicher, and Kasal 2014). Grasslands functioning and stability are crucial as grasslands cover one-third of the earth's terrestrial surface and 70% of the global agricultural area: they are the basis of many livestock production systems, and provide carbon storage, water purification, erosion control, biodiversity, and recreation (Reynolds and Frame 2005).

Meadow ecosystem services can strongly be affected by management intensity, commonly described using some parameters such as volume of cut grass, number of cuts per year, and nitrogen input levels as fertilizer or manure (Velthof et al. 2014). Among meadow regulating services, carbon storage is often under-considered despite grasslands globally store about 50% more carbon than forests due to their very wide geographic distribution (Conant 2010). Management intensity can affect this trait as intensively managed grasslands are plowed every few years, a practice that releases carbon into the atmosphere (Xiaojun et al. 2010). Many authors found that cut grasslands have a better impact on water quality and water resources than crops, but sewage fertilization can cause an abrupt increase in nitrate leaching (Benoit and Claude Simon 2004). Intensively managed meadows host a limited number of wild bee species

(Johan et al. 2020; Klaus et al. 2021) and few rare and specialist plant species (Hilpold et al. 2018). Bird species richness is also negatively correlated with the abundance of intensive meadows, which host mostly generalist species (Assandri et al. 2019). Transformations in grassland management intensity have different drivers and severities in different regions (Oenema, De Klein, and Alfaro 2014).

Changes in the socio-economic drivers on the Alps and other mountain region are exposing meadows to an intensification of their use in lowland areas and an abandonment in marginal areas. In addition, the availability of cheaper feed and forages from lowlands opened the nutrient cycles in many mountain farming systems. Nitrogen loads increased in many areas, despite a decrease of Livestock Units (e.g. −17% between 1980 and 2000 in Europe (Streifeneder et al. 2007; Cocca et al. 2012)). Consequently, the amount of ecosystem services provided by grasslands is decreasing, so that several policies and measures were introduced in many countries to support grassland management and conservation.

Among these, the 2013 EU Common Agricultural Policy (CAP) measure aiming at the conservation of permanent grasslands subsidizes meadow mowing but does not distinguish among grassland management intensities. Many authors warn those untargeted subsidies may lead to further intensification and abandonment (Herzon et al. 2018; Pe'er et al. 2014, 2017). However, more targeted policy measures would require updated information about meadow management intensity that was almost unavailable until the last few years as field surveys are very expensive and management intensity data were not required to the farmers by the EU.

In the last decades, remote Sensing (RS) has increasingly been used for ecosystem monitoring, as it provides accessible and reliable data at a very high spatial and temporal resolution. RS has been used for land-use classification, biomass estimation, disturbance detection, to monitor seasonal changes, and many other fundamental applications which enable an improved global change impact assessment and comprehension (Drusch et al. 2012). In grassland studies, the number of RS applications significantly increased in the last two decades (Reinermann, Asam, and Kuenzer 2020), spanning from botanical composition, structure and phenology to fodder quality and quantity and management regimes (Wachendorf, Fricke, and Möckel 2018; Kim et al. 2020;

Hua, Sirguey, and Ohlemüller 2021; Yan et al. 2020). By finding significant relationships with proper spectral vegetation indices (VIs), researchers were able to create models to assess fundamental grasslands traits. Mowing detection using remote sensing is a very new research field as the first algorithm was developed only in 2010 by Courault et al. (2010) and was based on LAI and NDVI time series derived from FORMO-SAT2 imagery. Other continuous monitoring optical sensors like MODIS (Halabuk et al. 2015; Estel et al. 2018) have been used, although their temporal and spatial resolution limited the application in intensively managed landscapes and in relatively large grasslands parcels (larger than 1 ha). The high temporal resolution and the continuity of synthetic aperture radar (SAR) backscatter data contributed to the adoption of this technology in many studies (Taravat, Wagner, and Oppelt 2019; Siegmund et al. 2019; Grant et al. 2015; Tamm et al. 2016; Zalite et al. 2016; Kaupo et al. 2013; Voormansik et al. 2016), but slope orientation and roughness of the parcels demonstrated to still hinder the detection of mowing events (Mathilde De, Radoux, and Defourny 2021; Wachendorf, Fricke, and Möckel 2018).

Thanks to its higher temporal and spatial resolution, Sentinel-2 (S2) imagery can overcome some of the limitations imposed by the previous optical sensors and has already been used for mowing detection at both regional (Kolecka et al. 2018) and national scales, in combination with Landsat images (Griffiths et al. 2020; Schwieder et al. 2021) and with active sensors (Lobert et al. 2021). The algorithm developed by Kolecka et al. (2018) allowed the correct detection of 77% of mowing events and is based on the detection of drops in the NDVI time series. Cloudy pixels dates are one of the major issues in VI time series (VITS) analysis and can be tackled by cloud masking and by VITS smoothing (Halabuk et al. 2015; Jin and Bing 2013; Garioud et al. 2019). Since Griffiths et al. (2020) and Kolecka et al. (2018) developed their models, S2 cloud masking improved (Frantz et al. 2018) leaving space to further algorithms development and increased efficiency of smoothing processes that perform better on less noisy time series.

Grasslands are changing rapidly and enhanced tools to monitor their management intensity are urgently needed to target conservation measures and actions. Despite the recent improvements in cloud masking of S2 images which provide more reliable high-resolution data, there are still few newly developed algorithms estimating grasslands mowing frequency. A more

accurate estimation model could be used to analyze grassland systems in terms of management intensity and to monitor extensively managed grasslands, which are typically associated with high conservation value and high abandonment risk, and therefore in compelling need of targeted subsidies.

Our study aims to develop a model for mowing frequency detection based on VITS analysis and integrating masking, smoothing, resampling, and drop detection processes. Since prior knowledge of management parcel geometries is often unavailable, mowing frequency should be estimated at both pixel and parcel resolution. To make the model affordable to agencies also in mountain areas the model is based on free S2 imagery, does not need local calibration and has been tested with reference data from fragmented and steep grassland areas. The algorithm was developed and can be run on Google Earth Engine platform (GEE) (Gorelick et al. 2017). This platform gives the possibility to build and optimize models testing various VIs with a high computational capacity and to provide local agencies with models which are replicable and easily applicable in different areas.

2. Materials and methods

2.1 Study sites

The algorithm was developed and tested on 240 ha of grassland fields located in the Province of Trento (northeast Italy), at the southern border of the European Alps

(Figure 1). The local climate depends primarily on elevation, which ranges from 60 to 3769 m a. s. l., and only secondarily on latitude. The province is classified as temperate oceanic according to the Worldwide Bioclimatic Classification System (Sboarina et al. 2004). Average yearly snow cover duration is between 20 and 40 days at altitudes lower than 1350 m a.s.l., between 50 and 65 days at altitudes between 1350 m a.s.l. and 1600 m a.s.l. (Marcolini et al. 2017).

Grasslands represent one of the main land covers in the province as they occupy 17% of the total area and 81% of the utilized agricultural area. Over 80% of grassland area is managed as pasture and only less than 20% of them are mowed (ISTAT 2010). Pastures are mainly located on the steeper slopes and on high altitude sites and are grazed by cattle in the period between June and September. Mown meadows are distributed at the valley's bottoms (where three or four cuts are carried out per vegetative season), on valley sides (one or two cuts) and on high-altitude plateaus (only one cut). Due to a fragmented property structure, the management is very patchy. Mowing-parcels are usually smaller than one hectare and the width of the parcels is often less than 30 m.

2.2 Field data

The reference data of mowing frequency used to optimize and validate the algorithm cover 240 grassland hectares at four sites (i.e. Lusia, Predazzo, Viote, Vigolana) and store information about the number of
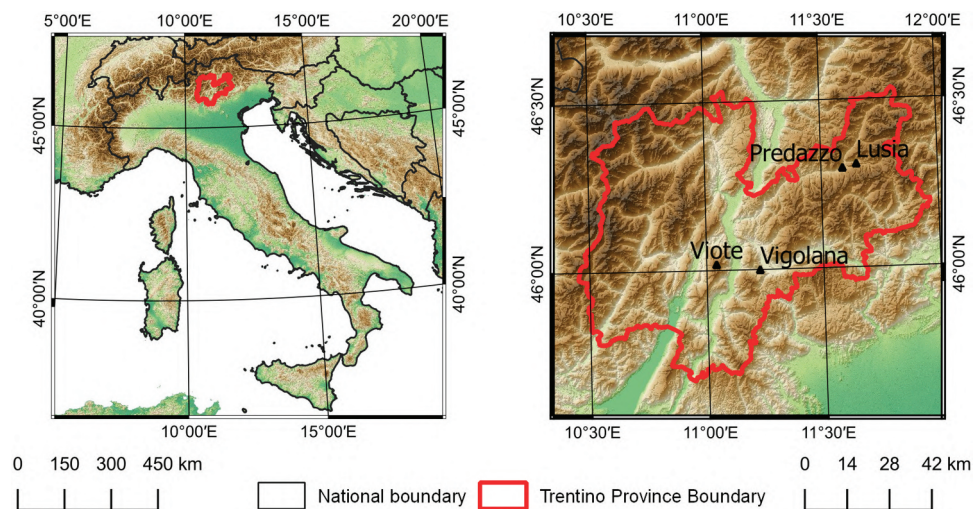

Figure 1. Location of the study areas in the Trento province inside Italy (left panel) and of the four study areas inside the Trento province (right panel).

mowing events occurred in each meadow parcel during 2020 (Table 1). For the sites of Vigolana, and part of Lusia and Predazzo the information was acquired through farmers interviews. Farmers were asked to point on a map the exact location of the meadow they manage, to draw the parcels on a very high resolution RGB image (Bing Maps) and to indicate the number of mowing events they performed during 2020 on each management parcel. Dates of mowing were not asked because we were interested only in mowing frequency and not in temporal accuracy, which is anyway at least partially lost during smoothing and resampling processes. For the site of Viote and part of Lusia and Predazzo photo interpretation on RGB daily Planet imagery (Planet Team 2018) at 3 m spatial resolution and visual inspection of a break in the NDVI curve were used to manually define the mows. All Planet images covering at least partially the study areas during the growing season were downloaded, resulting in an observed day every 1.39 days, 1.43 days and 1.64 days at the Lusia, Predazzo and Viote sites, respectively. To limit the edge effect, we selected only parcels large enough to contain a square of side 20 m which is twice the highest spatial resolution of S2 NIR and visible spectral bands. The parts of the parcels polygons narrower than 10 m were also removed from the dataset. To avoid mixed pixels all the parcels were shrunk by 5 m using the buffer tool in Qgis (QGIS Development Team 2021). Pastures and grazed meadows were identified through farmers' and local experts' interviews and were not included in the dataset. The average size of the (unshrunken) parcels ranges from 3689 m^2 at the Vigolana site to 15,000 m^2 at the Viote site.

The Lusia and Viote sites are located at altitudes higher than 1200 m a. s. l. and are therefore managed very extensively, with zero to two mowing per year with uncut corresponding to meadows not mown in last few years and still not colonized by woody vegetation. The Predazzo and Vigolana sites, on the other hand, are located at lower altitudes and managed more intensively, with one to four mowings per year. The slopes in the four considered sites are quite shallow, with average parcels slope of 10°, 4°,9°,12° at the Lusia, Predazzo, Viote, Vigolana site, respectively.

2.3 Imagery data

Level 2A multispectral satellite data acquired by the Sentinel-2 (S2) constellation accessed through Earth Engine Data Catalog were used in this study. The S2 images are characterized by 13 bands distributed in the visible, near infrared and shortwave infrared parts of the spectrum. Four bands are characterized by a 10 m spatial resolution (bands 2, 3, 4, 8), six by a 20 m spatial resolution (bands 5, 6, 7, 8A, 11 and 12) and three by 60 m spatial resolution (bands 1, 9 and 10). The S2 mission manages two identical polar orbiting satellites which survey earth from an altitude of 786 km. Their revisiting time is five days at the equator but nearer to the poles the orbits overlaps and therefore the revisiting time is shorter in overlapping areas. The sites of Lusia and Predazzo are surveyed by one orbit (i.e. orbit 22) and their revisiting time is five days. The sites of Vigolana and Viote, instead, are surveyed by two orbits (22 and 65) and their revisiting time is between two and three days.

Table 1. Topographical and management data about the study sites. Pixel counts are referred to shrunken parcels.

		Lusia	Predazzo	Viote	Vigolana
Altitude range m a. s. l.		1260–1990	950–1095	1520–1705	450–1095
Mean altitude m a. s. l.		1543	990	1570	740
Area of parcels (ha)		44.7	49.5	118.5	28.4
Number of pixels of reference data	From farmer/	1588	235	0	1888
	From photo interpretation	1646	3411	9413	0
Number of parcels of reference data	From farmer/	31	9	0	77
	From photo interpretation	39	66	79	0
Average parcel size (m^2)		6385	6601	14,998	3689
Number of mowings (area percentage)		1 (75%)	2 (42%)	0 (11%)	1 (37%)
		2 (25%)	3 (50%)	1 (89%)	2 (63%)
			4 (7%)		

Only images acquired during the 2020 growing season were considered. To set the start and end of growing season we followed the references proposed by Gensler (1946). The start of grassland growing season can be set when the daily mean temperature determined on multiple year time series reaches 7.5 C° and the end of the growing season can be set at 5 C°. In our study we divided grassland parcels -according to their altitude- in low altitude grasslands (<1200 m a. s. l.) and high-altitude grasslands (>1200 m a. s. l.). We set the start of the growing season respectively on April 15th and on May 15th and the end of the growing season on November 15th and on October 15th.

2.4 Methods

In Figure 2 a scheme of the proposed mowing detection algorithm is shown. In the following subsections every step is described in detail. The entire workflow was implemented in GEE (Gorelick et al. 2017).

In summary, the algorithm is based on the analysis of the VITS. Between the beginning and the end of the vegetative period, there are one or more growth periods and mowings of the grass. During the grass growth, the value of the VI increases until the farmer performs the cut which causes a sudden decrease in the index value. The number of sudden decreases in the index value followed by the slow increase in the index value represents the mowing frequency that
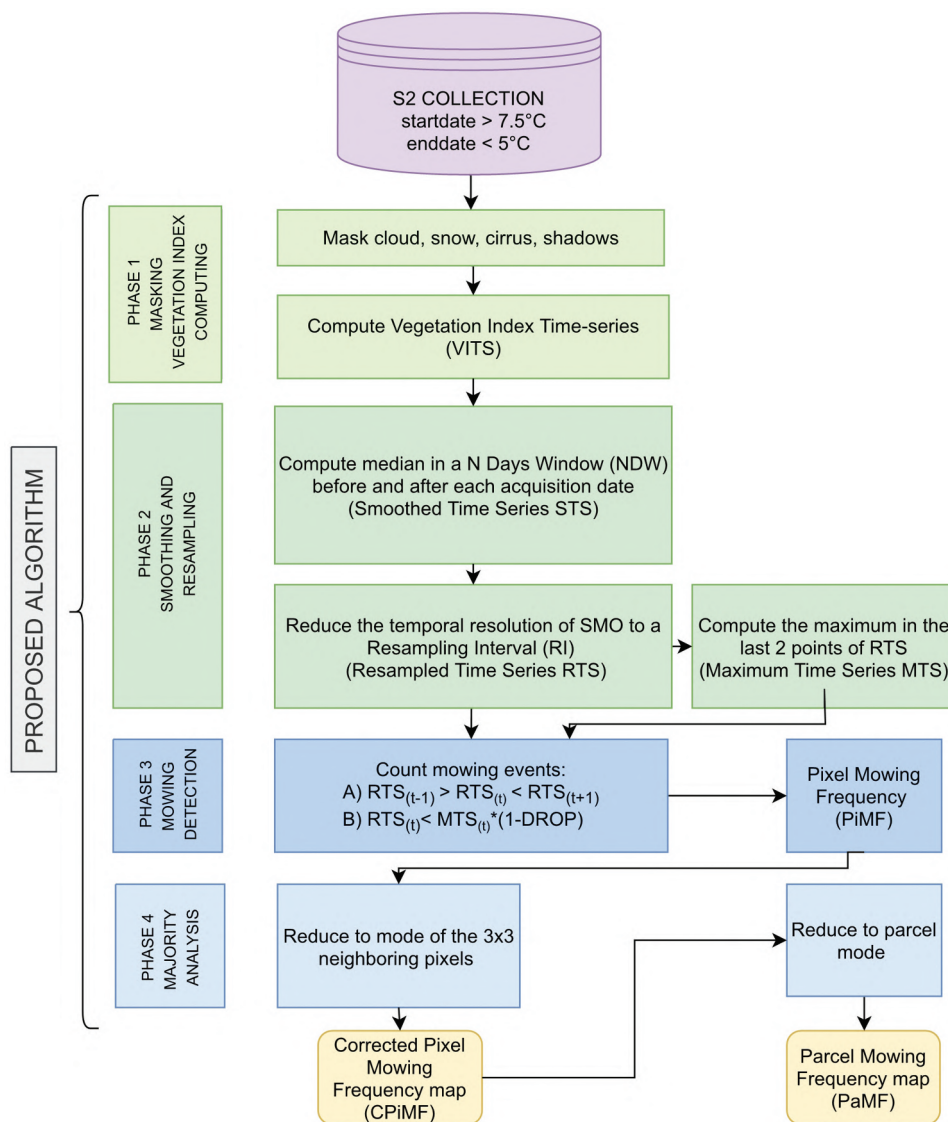

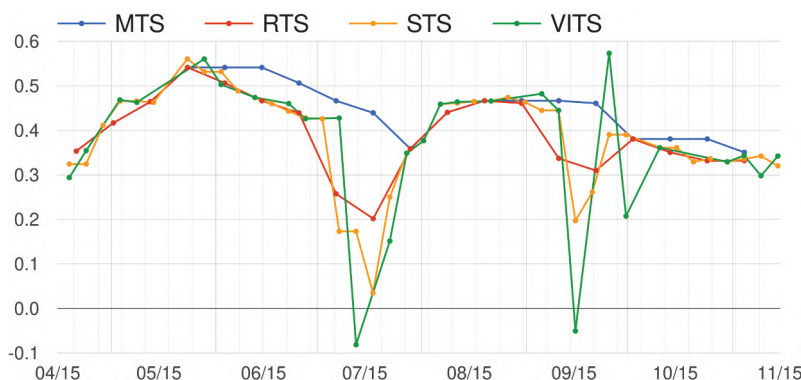**Figure 2.** Architecture of the proposed algorithm.

Figure 3. Annual curve of the raw (VITS) and derived (STS, RTS, MTS) vegetation index time-series of a grassland pixel at the Predazzo site mowed twice in 2020.

the algorithm is expected to determine. The algorithm development was carried out at the pixel level. In a final step, the best model developed at the pixel level was tested for accuracy at the parcel level.

2.4.1 Masking and vegetation index computing (phase 1)

S2 image pixels with cloud probability higher than 5% were discarded as cloudy pixels provide erroneous index values, which the algorithm could erroneously interpret as a mowing event. The adopted cloud probability was the one created with the S2-cloud-detector library and was provided as pixel property for each image in GEE. We masked out pixels with snow probability higher than 5% using MSK_SNWPRB band, distributed by ESA, and pixels identified as cirrus clouds and as shadows by the SCL band, distributed by ESA. Six VITS (EVI, GVMI, MTCI, NDII, NDVI, RENDVI$_{783.740}$) were computed in GEE based on the formulas described in Table 2. VIs were chosen based on recommendation proposed by Davidson, Wang, and Wilmshurst (2006), Imran et al. (2020) and

Reinermann, Asam, and Kuenzer (2020) and are presented in Table 2. All the S2 bands used for VI computation were resampled in GEE using nearest neighbor method to the resolution of the NIR and red band (10 m).

2.4.2 Smoothing and resampling (phase 2)

Omissions in cloud masking result in erroneous VIs values and a simple drop-detecting algorithm could wrongly consider the drops as mowing events and therefore rise the commission error. A smoothing process is therefore needed (Hird and McDermid 2009). We applied a running-median smoother to the raw VITS to overcome abrupt drops in the time series caused by unmasked cloudy observations (Jin and Bing 2013). A Smoothed Time Series (STS) is computed by identifying an observation dates list, including both cloudy and uncloudy observation. To each date in the list the median of VITS values falling in a N Days Window (NDW) before and after each point is assigned, omitting cloudy (masked) values.

Table 2. Vegetation Indices (VIs) used to calculate time series. Wavelengths of S2 bands: B2 (blue) ~ 494.4 nm; B4 (red) ~ 664.8 nm; B5 (Red Edge 1) ~ 703.9 nm; B6 (Red Edge 2) ~ 739.7 nm; B7 (Red Edge 3) ~ 781.1 nm; B8 (NIR) ~ 834.1 nm; B8A (Red Edge 4) ~ 864.4 nm; B11 (SWIR 1) ~ 1612.1 nm; B12 (SWIR 2) ~ 2194.1 nm.

Vegetation Index	Formula using Sentinel-2 Bands	Reference
EVI (Enhanced Vegetation Index)	$2.5 \frac{B8-B4}{(B8+6*B4-7.5*B2)+1}$	(Huete et al. 2002)
GVMI (Global Vegetation Moisture Index)	$\frac{(B8+0.1)-(B12+0.02)}{(B8+0.1)+(B12+0.02)}$	(Ceccato et al. 2002)
MTCI (MERIS Terrestrial chlorophyll index)	$(B8A - B5)/(B5 - B4)$	(Jadunandan and Curran 2004)
NDII (Normalized Difference Infrared Index)	$(B8 - B11)/(B8 + B11)$	(Hardisky, Klemas, and Smart 1983)
NDVI (Normalized Difference Vegetation Index)	$(B8 - B4)/(B8 + B4)$	(Rouse et al. 1974)
RENDVI$_{783.740}$ (Red edge Normalized Difference Vegetation Index)	$(B7 - B6)/(B7 + B6)$	(Peng et al. 2017)

A running-median smoother is resistant to outliers as it efficiently removes the invalid low values caused by unmasked cloudy observations.

In the preliminary analyses of our study, we found that in low-intensively managed grasslands, VI values can fluctuate during the summer for reasons that are different from mowing and are usually referable to water stress and heat stress. As we are interested only in major drops caused by mowing events, we reduced the temporal resolution of the time series using a fixed Resampling Interval (RI) to obtain Resampled Time Series (RTS). RTS is computed by defining a dates' list starting from half RI after the start of the growing period date and prosecuting with dates at RI intervals until the end of the growing period. To each date in the list the mean of STS values falling in NDW before and after each point is assigned. Raw and derived vegetation index time series of a grassland pixel are displayed in Figure 3 as an example.

2.4.3 Mowing detection (phase 3)

Mowing events cause remarkable drops not only in the VITS (Stendardi et al. 2019), but also in the RTS, so we set the condition that a local minimum (i.e. an index value lower than previous value and following value) should reach a minimum drop (DROP) from the maximum in the last two points (MTS) of RTS to be interpreted as a mowing event. To obtain the Pixel Resolution Mowing Frequency (PiMF), the algorithm detects and counts the mowing events (defined as local minimum in the masked, smoothed, resampled time series) which cause a minimum drop from previous values. The two conditions are mathematically stated in equation 1, where RTS is the Resampled Time Series, MTS is the Maximum Time Series and DROP is an optimized parameter that defines the minimum percentage difference between MTS and RTS to identify a mowing event.

$$\begin{cases} RTS_{(t-1)} > RTS_{(t)} < RTS_{(t+1)} \\ RTS_{(t)} < MTS_{(t)} * (1 - DROP) \end{cases} \quad (1)$$

2.4.4 Majority analysis (phase 4)

To reduce the "salt and pepper" effect in the final mowing events map, we performed a majority analysis using a 3×3 pixels kernel, obtaining the Corrected pixel Mowing Frequency (CPiMF). This operation removes abnormal frequency values of some pixels (noise) from PiMF replacing them with values calculated from the majority of their neighboring cells. We have chosen a small kernel size (3x3 pixels) because the scale of management was often as small as a few pixels (Qian, Zhang, and Qiu 2005). Then, for each parcel we calculated the mode of the CPiMF of its pixels and obtained the Parcel Mowing Frequency (PaMF).

2.4.5 Design of experiment and accuracy assessment

To define the most accurate prediction algorithm and to measure its generalization capability, the following four experiments were carried out:

(1) Experiment 1: parameters optimization and vegetation index choice. The accuracies obtainable using different VIs were tested, optimizing the three parameters (NDW, RI, DROP) at the four sites. Parameters' levels to be tested were chosen based on preliminary analyses which revealed the ranges in which the most promising accuracies could be obtained in our study sites. We included 7 values of DROP (from 0 to 0.35), 15 values of RI (from 6 to 20), 5 values of NDW (from 6 to 10). We defined the best general optimization as the combination of parameters that gives the lowest Mean Absolute Error (MAE). We computed the mean MAE across all four sites for each parameter combination and we chose the parameter combination that determined the lowest MAE, as visually described in Figure 4. The MAE measures the average error regardless of its sign and gives the magnitude of the error in the same unit as the prediction, in this case, the mowing frequency (Lobert et al. 2021; Congalton and Green 2009). The MAE was computed as follows:

$$MAE = \frac{1}{n} \sum_{i=1}^{n} \left| \hat{Y}_i - Y_i \right| \quad (2)$$

(1) where n is the number of pixels, $\hat{Y}$ is the predicted mowing frequency and Y is the reference mowing frequency. Overall accuracy was also computed and reported. The overall accuracy is simply the sum of the major diagonal (i.e. the correctly classified sample units) divided by the total number of sample units in the
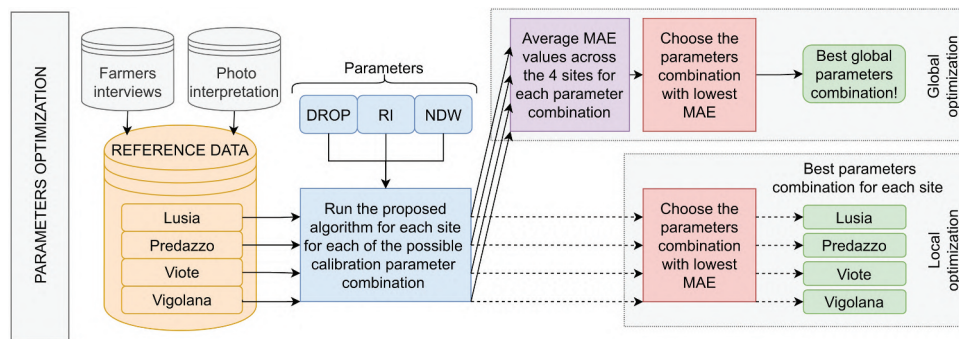
Figure 4. Architecture of parameters optimization process.

confusion matrix (Congalton and Green 2009). We used the function ee.FeatureCollection. errorMatrix implemented within the GEE platform to obtain the error matrix, ee. ConfusionMatrix.accuracy to obtain the Overall Accuracy, whereas the MAE was computed in GEE following equation 2. To understand how much accuracy is lost by generalizing the optimization of the algorithm, we compared the accuracies of locally optimized (separately in each site) algorithms and globally optimized (on all four sites together) algorithms (Figure 4).

(2) Experiment 2: testing of algorithm phases. All phases of the algorithm were tested in order to see if they were necessary to remarkably increase its accuracy. The phases presented in Figure 2 were therefore combined as presented in Table 3.

At each phase combination, the parameters optimized in the previous phase combination were re-optimized, as their best values could change in the new phase combination. The optimization was performed finding the best parameter combination for all study sites (global optimization). In order to carry on such experiments, some adjustments were necessary to the algorithm code at the first phase combination. In the algorithm considering only phases 1 and 3, a daily time series was built by applying a linear interpolator between each valid observation. MTS were computed taking the maximum value in the N Days Backward (NDB). The best NDB was optimized, choosing between values in sequence from −30 to −5 with step 5.

(1) Experiment 3: comparison of pixel and parcel resolution accuracy. We calculated the mode of each parcel's CPiMFs obtained with the best globally optimized model. The accuracy of the resulting PaMF was compared to that of CPiMF.

Table 3. Combinations of phases tested.

Phase combination	Description	Parameter to optimize
1,3	Vegetation index time-series computing (phase 1), and mowing detection (phase 3)	DROP, NDB
1,2,3	Vegetation index time-series computing (phase 1), smoothing and resampling (phase 2), and mowing detection (phase 3)	DROP, NDW, RI
1,2,3,4	Vegetation index time-series computing (phase 1), smoothing and resampling (phase 2), mowing detection (phase 3), and majority analysis (phase 4)	DROP, NDW, RI

Table 4. Confusion matrix (pixel count in cells), mean absolute error and overall accuracy resulting at each site from the algorithm optimized at all four sites (global optimization: DROP = 15%, NDW = 9 days, RI = 11 days). NDII used as vegetation index.

		Reference mowing frequency (no. mowing per year)																			
		Lusia					Predazzo					Viote					Vigolana				
		0	1	2	3	4	0	1	2	3	4	0	1	2	3	4	0	1	2	3	4
Predicted mowing frequency (no. mowing per year)	0	0	0	0	0	0	0	0	0	0	0	968	81	0	0	0	0	0	0	0	0
	1	25	2253	168	0	0	0	0	0	0	0	40	8324	0	0	0	2	651	17	0	0
	2	0	87	701	0	0	0	31	1268	187	15	0	0	0	0	0	0	47	1163	8	0
	3	0	0	0	0	0	0	0	273	1599	7	0	0	0	0	0	0	0	0	0	0
	4	0	0	0	0	0	0	0	2	39	255	0	0	0	0	0	0	0	0	0	0
	MAE	0.09					0.16					0.01					0.04				
	Overall Accuracy	91%					85%					99%					96%				

(2) Experiment 4: generalization error estimation. We performed a spatially stratified k-fold cross validation, using the sites as stratification layer to decrease correlation between optimization and validation pixels. We iteratively optimized the parameters of the model on three sites out of four, and we measured the accuracy obtained at the fourth site. We averaged the four accuracies obtained on the "left-out" site and we compared it to the four accuracies obtained on the optimization dataset to estimate the generalization capabilities of the proposed model.

3. Results

3.1 Masking processes

The number of available unmasked observations per pixel (Figure 5) considerably varied in the four study sites, depending on the topographical and geographical location of the study site, on the number of cloudy days and on the length of the growing season. The topography -especially the altitude- affects cloud distribution and snow persistence and therefore also the spatial distribution of valid observations (i.e. cloud, shadows, and cirrus free). In addition, altitude is the main determinant for the length of the growing season and therefore for the total number of dates to be considered. The average interval between unmasked observations is 9.19 days, 8.33 days,

4.15 days, and 4.25 days, respectively at the Lusia, Predazzo, Viote, Vigolana site. Sites located in the west of the province (Vigolana and Viote) are revisited every two to three days, so their time series is denser than the time series of sites located in the east of the province (Predazzo and Lusia), surveyed by one orbit only. The percentage of unmasked observations (average of site pixels) is similar in all four sites, between 57% (Lusia site) and 61% (Viote site).

3.2 Parameters optimization and vegetation index choice

NDII was chosen as the VI of the final algorithm, as it performed better than all other VIs, resulting in a MAE of 0.07 (average of all sites; Figure 6). Also, GVMI and NDVI performed quite well, with a MAE of 0.09 and 0.12, respectively (average of all sites).

In Figures 7, 8, the accuracies of NDII models with different DROP, NDW, RI across the four sites are reported. Viote and Vigolana sites generally showed a higher accuracy compared to Lusia and Predazzo and parameters optimization affected in different ways the results across sites. For NDW higher than 9 days there was a strong increase in MAE for the Lusia site, while MAE decreased in the Viote site. Predazzo site performed better with shorter RI, while Vigolana and Viote with longer RI. DROP did not strongly influence the accuracy on all sites except the Vigolana site, where there was an increase in MAE for DROP higher than 20%. The best global (for the four sites together) optimization for NDII was: DROP = 15%, NDW = 9 days, RI = 11 days.
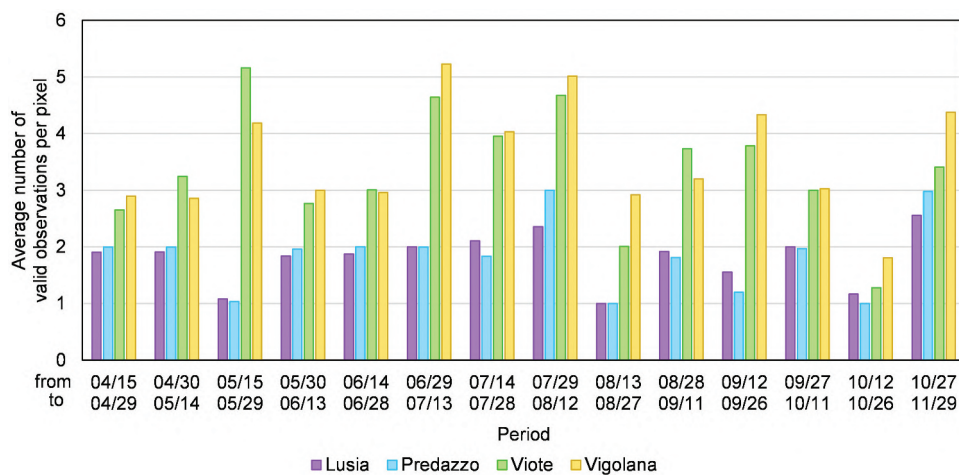

Figure 5. Average number of valid observations per pixel in the study sites in 14 days periods.
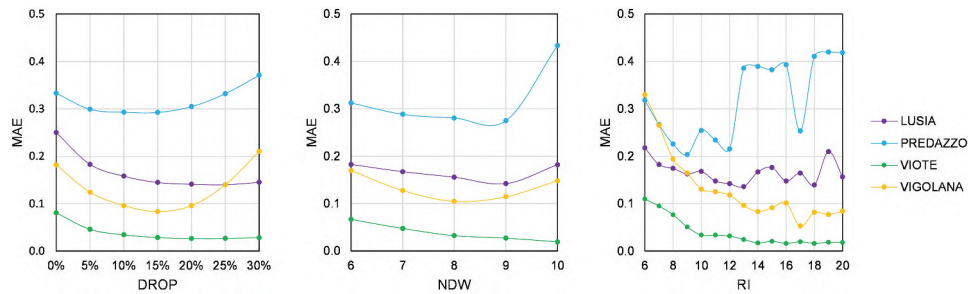
Figure 6. Mean absolute error of algorithms with different vegetation indices. Pixel level.

Figure 7. Mean absolute error in the study sites. NDII used as vegetation index. Pixel level.

In all four sites the commission and omission error were quite balanced, resulting in a percentage of pixels with predicted mowing frequency higher than reference mowing frequency similar to the percentage of pixels with predicted mowing frequency lower than reference (Figure 9). In all four study sites, the overall accuracy was higher than 85% and the MAE was equal or lower than 0.16 (Figure 6, Table 4). The MAE

Figure 8. Mean absolute error across the four study sites using algorithms with different NDW, RI, DROP. NDII used as vegetation index. Pixel level.
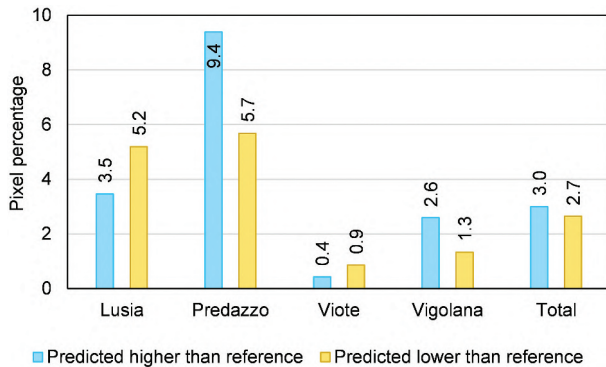
Figure 9. Types of errors in the four study sites at pixel level using the parameters of the global optimization, and NDII as vegetation index.

obtained using locally optimized algorithms was slightly lower than MAE obtained using globally optimized algorithms in all four sites (Figure 10).

In Figures 11 and 12, reference and predicted mowing frequency maps of the Predazzo and Viote sites are displayed. Predicted values were obtained using the best global optimization.
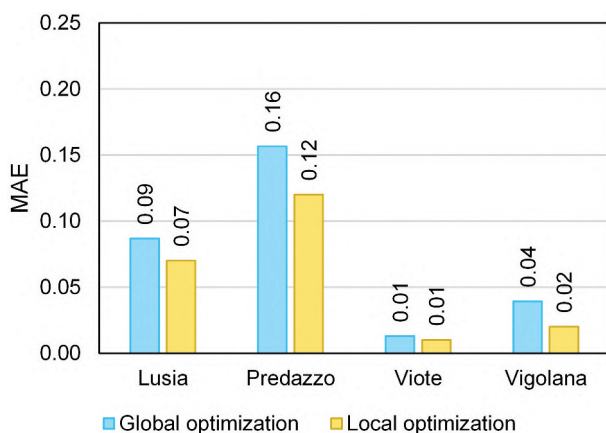
Figure 10. MAE at pixel level obtained using global optimization and local optimization, and NDII as vegetation index.

3.3 Testing of algorithm phases

In all the four sites, the algorithm which included all phases was by far the one that provided the lowest MAE (best results displayed in Figure 13).

In the optimization of the algorithm involving only phases 1 (VITS preparation) and 3 (drop and local minimum detection), a DROP of 75% from previous values and a NDB of ten days proved to be the best optimized parameters on average. The Viote and the Vigolana sites performed better with a higher DROP, with the lowest MAE (0.65 and 0.79 respectively) in correspondence to a DROP of 95%. The Lusia and the Predazzo sites performed better with a lower DROP, with the lowest MAE (0.25 and 0.39 respectively) in correspondence to a DROP of 60% and 65%. Adding the smoothing and resampling phases to the algorithm contributed to a substantial improvement in accuracy across all four sites, and the best results on average were found using a DROP of 15%, an NDW of 9 days and a RI of 12 days. The final algorithm which also includes the majority analysis (phase 4) gave the best results and the best global optimization parameters were DROP = 15%, NDW = 9, and RI = 11.

3.4 Comparison of pixel and parcel resolution accuracy

In the Viote and Vigolana sites, the aggregation of the parcel CpiMPs to PaMF through the mode rule did not impact the accuracy, while at the Lusia and Predazzo it determined a small increase in the MAE (Figure 14). On average at the four study sites we obtained a 90% overall accuracy and 0.10 MAE, and only 30 parcels out of 301 which were not correctly classified (Table 5).
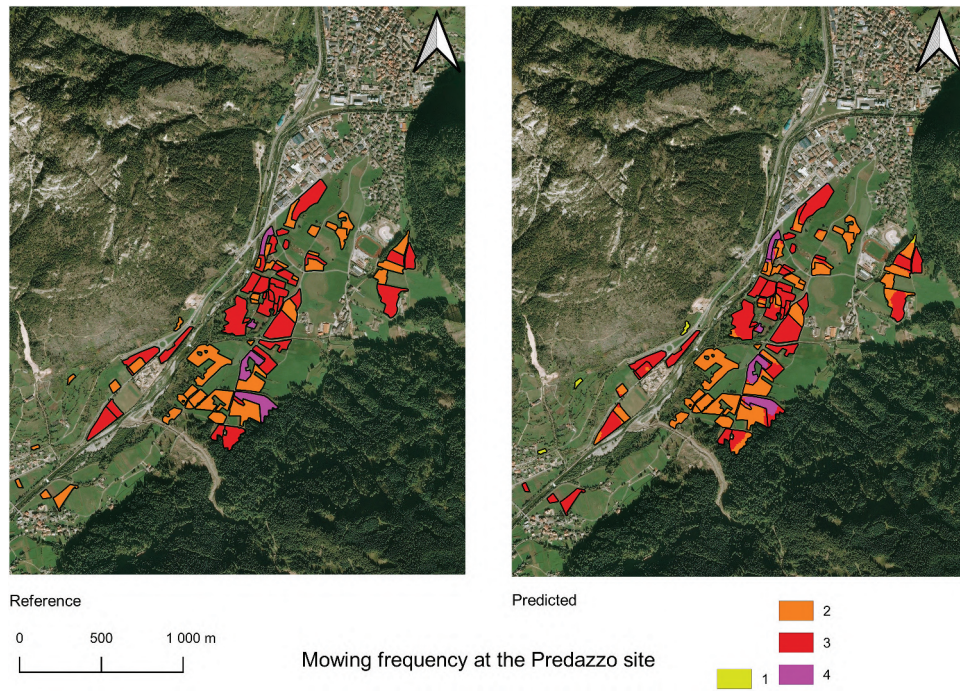
Figure 11. Reference (left) and predicted (right) mowing frequency map at pixel level of the Predazzo site. Predicted values are obtained using best global optimization, and NDII as vegetation index.
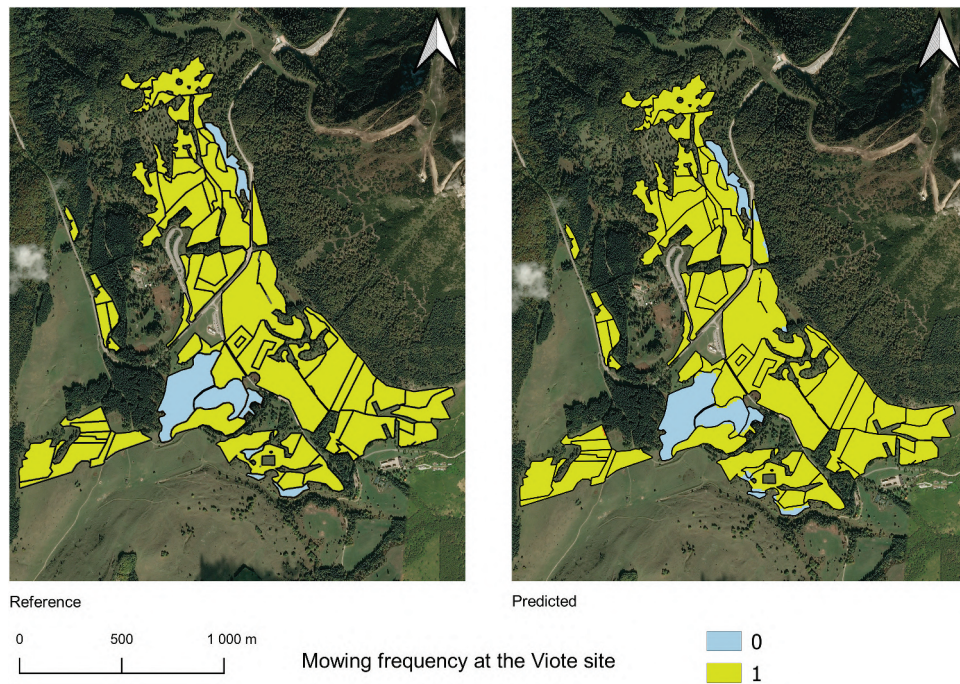

Figure 12. Reference (left) and predicted (right) mowing frequency map at pixel level of the Viote site. Predicted values are obtained using best global optimization, and NDII as vegetation index.
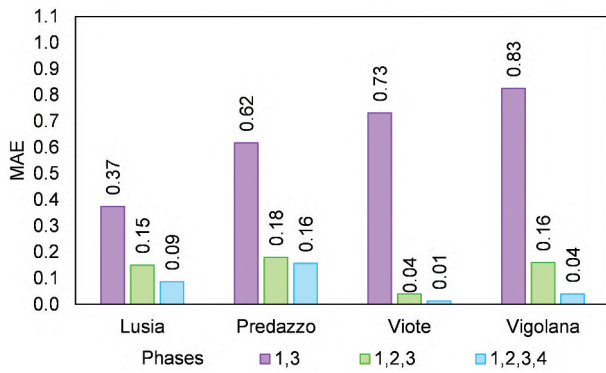
Figure 13. MAE of algorithms with increasing complexity. NDII was used as vegetation index. For phase description see Table 3. The values indicate the highest accuracy obtained with global optimization. Pixel level.
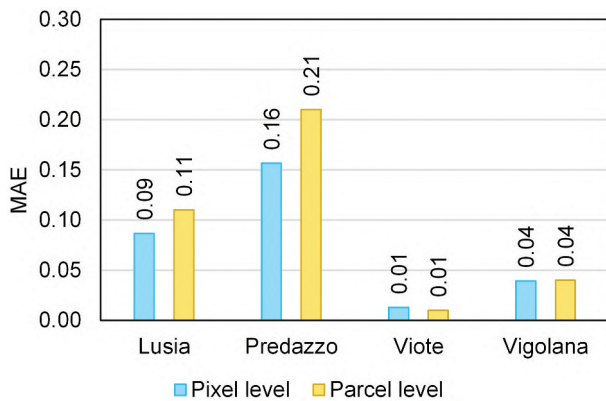
Figure 14. MAE of the best optimized algorithm at pixel and parcel level. NDII used as vegetation index.

3.5 Generalization error estimation

The average MAE obtained on the validation dataset (0.12) was almost double than the average MAE obtained on optimization dataset (0.07) but it is still very low, indicating that just approximately one pixel out of ten was wrongly classified (Figure 15). The third iteration (the one excluding the Viote site from the optimization dataset) gave the highest MAE on the optimization dataset and the lowest MAE on the validation dataset, whereas the second iteration (the one excluding the Predazzo site from the optimization dataset), on the opposite, gave the lowest MAE on the optimization dataset and the highest MAE on the validation dataset.

4. Discussion

Mapping mowing frequency over complex landscapes in mountain areas is crucial to inform conservation and management policies but is challenging as imagery with high spatial and temporal resolution is needed. In this study, we developed a new mowing detection algorithm based on S2 imagery in GEE, optimized and validated in four study sites. Results indicate that it can be successfully used, as the MAE of the complete model is 0.07, while the overall accuracy is 93% on average at the sites used for optimization and 0.12 and 89%, respectively, at sites not used for optimization.

4.1 Novel aspects

In addition to the use of S2 imagery for mowing detection, that has been exploited a few times so far, the major novel aspects of the present study are that very small and fragmented parcels were used as reference, that the algorithm works at pixel level and that the algorithm can be run using a provided ready to use code working on one planetary-scale cloud platform using free imagery.

Reference dataset consists of particularly small and fragmented hay meadows that are typical of mountain areas, whereas previous research work focused mainly on much more homogeneous landscapes, so their accuracy in complex landscapes was therefore not tested. In our study, 53% of unshrunken parcels

Table 5. Confusion matrix (parcel count in cells), Mean Absolute Error and overall accuracy resulting at each site from the algorithm optimized at all four sites (global optimization: DROP = 15%, NDW = 9 days, RI = 11 days). NDII used as vegetation index.

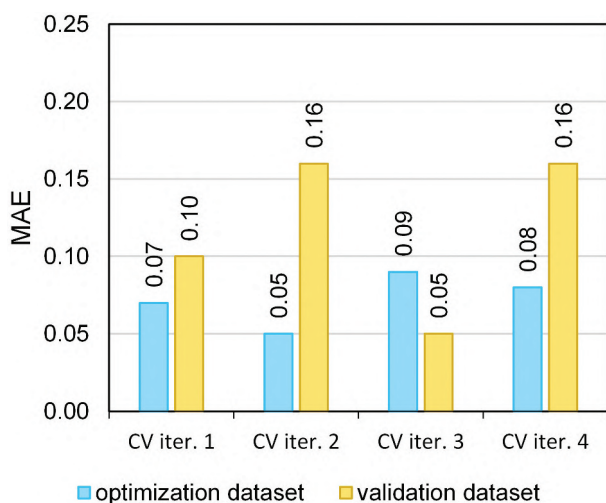|		Reference mowing frequency (no. mowing per year)																				
		Lusia					Predazzo					Viote					Vigolana				
		0	1	2	3	4	0	1	2	3	4	0	1	2	3	4	0	1	2	3	4
Predicted mowing frequency (no. mowing per year)	0	0	0	0	0	0	0	0	0	0	6	1	0	0	0	0	0	0	0	0	0
	1	0	44	4	0	0	0	0	0	0	0	0	72	0	0	0	0	24	2	0	0
	2	0	3	19	0	0	0	3	27	6	1	0	0	0	0	0	0	2	48	1	0
	3	0	0	0	0	0	0	0	7	27	0	0	0	0	0	0	0	0	0	0	0
	4	0	0	0	0	0	0	0	0	0	4	0	0	0	0	0	0	0	0	0	0
	MAE	0.10					0.24					0.01					0.06				
	Overall Accuracy	90%					77%					99%					94%				

Figure 15. Results of the k-fold cross validation. NDII used as vegetation index. Pixel level. CV iter. 1 = validation on the Lusia site, CV iter. 2 = validation on the predazzo site, CV iter. 3 = validation on the viote site, CV iter. 4 = validation on the vigolana site. Average error on optimization datasets = 0.07, average error on validation datasets = 0.12.

were smaller than 0.5 ha and 78% were smaller than 1 ha whereas in (Garioud et al. 2019) the parcel average size was 5.1 ha and in (Griffiths et al. 2020) all parcels were larger than 1 ha. Only Kolecka et al. (2018) included parcels with sizes comparable to the ones we included.

The analysis concept in our study builds on the pixel level because in most of grassland systems management parcels, defined as grassland unfragmented parcels mowed on the same days, are not available a priori, as administrative boundaries often differ substantially from real field limits (Inglada et al. 2012). An algorithm working at pixel level can analyze a meadow system without prior information about management parcels and without losing the possibility to aggregate later the results at parcel level as we did at paragraph 3.4, which is very useful for various purposes such as subsidies granting and fertilization plan development. The accuracies obtained at parcel level were slightly lower than at the pixel level at the Lusia and Predazzo sites, where the size of the erroneously classified parcels was on average 35% and 50%, respectively, of a similar size to the correctly classified parcels. Also, in the other sites the wrongly predicted parcels are on average much smaller than the correctly predicted, 13% the size of correctly predicted parcels at the Viote site and 26% the size of correctly predicted parcels at the

Vigolana site. This accuracy reduction was probably due to residual (after the initial edge pixels elimination by buffering procedure) edge effect of mixed pixels.

The development of our algorithm in GEE allowed us to access, process and display S2 data on only one platform and will allow algorithm's users to easily run the code on continuously updated imagery and in other regions, without needing to download and process the imagery. It is not possible to report exact computation times in GEE because they vary in each run, as the system handles resource allocation and parallelism. As an example, however, less than one minute is needed to compute and display the mowing frequency of hay-meadows in 20 km^2, and 2 minutes for exporting the mowing frequency map in ".tiff" format.

Mowing frequency maps produced adopting the proposed algorithm can be a valuable and reliable tool to identify extensively managed meadows needing protection and conservation measures. They can be used also to remotely verify that a mowing event occurred, which is frequently required not only to obtain CAP subsidies, but also to characterize forage systems at a regional level, using mowing events as a proxy to estimate nitrogen removal and forage production (Griffiths et al. 2020).

4.2 Accuracy and generalization capability

The possibility to reliably apply the algorithm to other areas after appropriate testing is suggested by the results of the k-fold cross validation. The average MAE obtained on the sites excluded from parameters optimization process is 0.12, with an overall accuracy of 89% on average. Also, local and global optimization did not give significantly different results, indicating that the algorithm is very flexible and that globally optimized parameters perform well in various different situations.

Some previous studies using SAR data reported an overall accuracy in mowing detection of 86% (Taravat, Wagner, and Oppelt 2019) using artificial neural networks from a set of Sentinel-1 derived variables, but models were trained and tested on just ten intensively managed parcels. Grant et al. (2015) reached a detection rate of 74% and Mathilde De, Radoux, and Defourny (2021) correctly identified only 56% of grasslands. The highest overall accuracy reported

using optical sensors is 85% and was obtained by Halabuk et al. (2015) as the best result of a cut-uncut classification in extensively managed grasslands. In a time series analysis approach Kolecka et al. (2018) using a drop-detection algorithm achieved an overall accuracy of 77% of correctly detected mowing. Estel et al. (2018), detecting local minima in a MODIS NDVI time-series, correctly identified 80% of mowing frequency. The combination of Sentinel-2 and Landsat-8 imagery resulted in denser time-series which were analyzed by Schwieder et al. (2021) using machine learning algorithms and leaded to a mean absolute percentage error between 35% (2020) and 40% (2018) whereas combining active and passive imagery Lobert et al. (2021) obtained a MAE of 0.369, 0.321, 0.420, 1.44 on grasslands with one to four mowing events per year, respectively. Our work, which benefits from S2 high temporal resolution, novel cloud masking and smoothing and resampling processes, reached a MAE of 0.12 and an overall accuracy of 89% on average on the sites excluded from parameters optimization process.

4.3 Parameters optimization and vegetation index choice

Building a mowing frequency reference dataset from optical imagery is not a straightforward task because of lack of temporal resolution caused by cloudy observations (Halabuk et al. 2015). In our experience the temporal resolution provided by Planet imagery was sufficient to detect mowing events, probably because farmers do not perform mowing in cloudy periods and wait a clear-sky window of at least 2 days to perform mowing. Furthermore, during summer clouds are much more common in the afternoon than in the morning (Whitcraft et al. 2015), when the Planet images are acquired.

NDVI is by far the most used index in previous studies about grasslands management and intensity and it describes the difference between reflectance in the red and near infrared regions (Reinermann, Asam, and Kuenzer 2020). In our study, however, NDII gave the best MAE, on average 0.05 points lower than NDVI. NDII is computed as the normalized difference between the red and the SWIR region, a wavelength that is sensitive to leaf water content. Observing NDVI and NDII profile we found that mowing events cause much more remarkable drops in NDII than in NDVI

and that NDVI saturates before NDII as biomass increases. The canopy water content and canopy structure traits change strongly during the mowing event determining a wider range of NDII values. The wider range of values NDII can assume compared to VIs sensitive to chlorophyll content proved to result in a higher algorithm's accuracy. The increase in accuracy provided by the SWIR wavelength is higher than the decrease caused by the lower spatial resolution of the Sentinel SWIR band (20 m) compared to NIR band (10 m). GVMI, which is computed using the SWIR 2 band (2.2 μm), gave accuracies that are comparable to that obtained using NDII (average MAE = 0.09 vs 0.07), whereas EVI, MTCI and RENDVI provided lower accuracies although they have widely been used in remote sensing of grassland biophysical parameters (Sakowska, Juszczak, and Gianelle 2016; Reinermann, Asam, and Kuenzer 2020; Imran et al. 2020; Halabuk et al. 2015).

The sites surveyed by two orbits (Viote and Vigolana) gave much higher accuracies. In these sites the shorter revisiting time provides a denser time series that is less affected by missing (cloud masked) observations. Only at the most intensively managed site, the Predazzo site, the MAE increases using longer RIs, whereas in extensively managed sites like the Viote site the MAE decreases for longer RIs. The longer RI in extensively managed sites reduces the possibility of false detections caused by VI fluctuations, whereas in intensively managed grassland is not able to describe the quick development of grassland biomass and cover.

4.4 Testing of algorithm phases

The complete algorithm -which includes all the four phases- provided the highest accuracies and was therefore chosen. The smoothing and resampling phases proved to be crucial to diminish the effect of invalid low values caused by unmasked cloudy observations and by small fluctuations of index values. The simple drop detection algorithm (phases 1 and 3) gave very low accuracy for example at the Viote site where there were three unmasked cloudy observations that caused abrupt drops in VITS that were detected as mowing events. These unmasked cloudy observations were smoothed by the running median, and the Viote sites is the one with the highest accuracies using the complete algorithm.

Following the experience of Halabuk et al. (2015) who obtained lower accuracies classifying cut and uncut hay meadows by smoothing NDVI and EVI time-series using the Fourier adjustment, smoothing processes were not included in past models because of the risk of losing small fluctuations which might be linked with mowing (Bekkema and Eleveld 2018). Also Jin and Bing (2013), proposing a temporal smoothing algorithm, advise that smoothing may not be suitable for modeling anthropogenic activities where an abrupt drop of the NDVI value reflects the actual situation rather than contamination. The running median smoother used in our work, however, proved to fix single invalid low values caused by unmasked cloudy observations. S2 temporal resolution proved to be sufficient to provide proper values and therefore to describe biomass evolution under the considered management intensities. Majority analysis significantly improved the algorithm accuracy, decreasing the MAE from 0.13 to 0.7 on average. Isolated pixels fixed by majority analysis are mainly located at parcel edge and in areas possibly shadowed by surrounding woodlands. Small and isolated trees were found to be one cause of "salt and pepper effect" at the Viote site. On more productive grasslands, lodging could be a possible cause of patchy anomalous mowing frequency values. Lodging is not a rare phenomenon on productive grasslands and can significantly alter grasslands structure and physiology, and therefore their spectral signature.

4.5 Limitations and further improvement

The major limitations of the presented algorithm are the spatial resolution, the prior management type detection, the lack of temporal accuracy, the reliability in areas with very different phenology. The spatial resolution of S2 imagery limits the accuracy of the algorithm in very fragmented parcels and in long and narrow management parcels which frequently occur in mountain areas. The algorithm was tested only on hay-meadows, and the process does not include a prior management type detection (grazed, mowed, mixed) like the one presented by Dusseux, Corpetti, and Hubert-Moy (2013). Grazed parcels should therefore be avoided, as grazing events with large stock density could be interpreted as mowing events.

The algorithm is specifically designed to detect annual grassland mowing frequency and not to predict mowing dates. In fact, smoothing and resampling phases improved impressively the algorithm accuracy, but changed the temporal resolution so that resampled dates can not be used to define precise mowing dates.

The algorithm should be tested and probably adapted before use in areas with very different climate and phenology. In Mediterranean grasslands, for example, the growing season is limited by high temperatures and the sudden decrease of water content that may occurs at the start of summer may be wrongly interpreted as a mowing event by the algorithm. In more cloudy regions, on the other hand, the lower density of the time series could affect algorithm accuracy, since the algorithm has been tested only in sites where the average number of days between uncloudy observations ranges from 4.15 (Viote site) to 9.19 (Lusia site).

Further improvement and optimization of the algorithm could be the inclusion of a classification algorithm for detecting management parcel geometries, the type of grassland management and the automatic definition of the start and the end of growing season at a pixel-size resolution (Jönsson and Eklundh 2004). A pixel-level automatically defined growing season would avoid the necessity to manually define growing season based on available climatic data and would model a growing season more similar to real one in each grassland pixel. As the frequency of cloudy masked and invalid unmasked pixels proved to considerably affect the algorithm accuracy and algorithm performed less well when the mowing frequency was higher (Predazzo), its validation in other climatic regions would be important. In addition to these, orbit overlap giving better results suggests that accuracy could be improved by increasing the density of the time series either by adding optical sensors (Griffiths et al. 2020; Lobert et al. 2021; Stumpf et al. 2020) or by multimodal approaches (Garioud et al. 2019; D'Andrimont, Lemoine, and Van der Velde 2018).

5. Conclusions

This study assessed the potential of a new algorithm based on S2 imagery time series for detecting mowing events. Using reliable reference data obtained by

Planet daily imagery and farmers interview, it was possible to test several vegetation indices and processing phases. Masking, smoothing and resampling phases and optimization of algorithm's parameter allowed to correctly identify the mowing frequency in 93% of the pixels, with a MAE of 0.07 on average, and 90% of parcels were correctly classified (Overall accuracy at parcel level) on sites used for optimization. NDII performed better than other indices probably because it assumes a wider range of values before and after mowing events.

The low MAE obtained on the sites excluded from parameters optimization process (MAE = 0.12, overall accuracy = 89%) suggest that the developed algorithm may be applicable on other grassland areas, and new studies are needed to confirm this. The code was developed in GEE, a platform that can access and process continuously updated images worldwide, so that agencies and practitioners can easily run the algorithm as only start and end of growing season, and hay-meadows parcel geometries are required as an input parameter. The resulting mowing frequency maps can inform grasslands conservation and management policies by identifying extensively managed grasslands.

Disclosure statement

No potential conflict of interest was reported by the author(s).

ORCID

Davide Andreatta http://orcid.org/0000-0001-6821-1152
Damiano Gianelle http://orcid.org/0000-0001-7697-5793
Michele Scotton http://orcid.org/0000-0002-0221-0875
Loris Vescovo http://orcid.org/0000-0001-8212-8320
Michele Dalponte http://orcid.org/0000-0001-9850-8985

References

Assandri, G., G. Bogliani, P. Pedrini, M. Brambilla, and G. Siriwardena. 2019. "Toward the Next Common Agricultural Policy Reform: Determinants of Avian Communities in Hay Meadows Reveal Current Policy's Inadequacy for Biodiversity Conservation in Grassland Ecosystems." *Journal of Applied Ecology* 56 (3): 604–617. doi:10.1111/1365-2664.13332. Edited by Gavin Siriwardena.

Bekkema, M. E., and M. Eleveld. 2018. "Mapping Grassland Management Intensity Using Sentinel-2 Satellite Data." *GI_Forum* 1. doi:10.1553/giscience2018_01_s194.

Benoit, M., and J. Claude Simon. 2004. "Grassland and Water Resources: Recent Findings and Challenges in Europe." In *Proceedings of the 20 Th General Meeting, Land Use System in Grassland Dominated Regions*, 21-24 June 2004, *Luzern, Switzerland*, 117–118.

Ceccato, P., S. Flasse, J. Marie Grégoire, B. Pinty, and S. Tarantola. 2002. "Designing a Spectral Index to Estimate Vegetation Water Content from Remote Sensing Data: Part 1: Theoretical Approach." *Remote Sensing of Environment* 82 (2–3): 188–197. doi:10.1016/S0034-4257(02)00037-8.

Cocca, G., E. Sturaro, L. Gallo, and M. Ramanzin. 2012. "Is the Abandonment of Traditional Livestock Farming Systems the Main Driver of Mountain Landscape Change in Alpine Areas?" *Land Use Policy* 29 (4): 878–886. doi:10.1016/j.landusepol.2012.01.005.

Conant, R. T. 2010. "Challenges and opportunities for carbon sequestration in grassland systems." Rome: Food and Agriculture Organization of the United Nations (FAO).

Congalton, R. G., and K. Green. 2009. "*Assessing the Accuracy of Remotely Sensed Data: Principles and Practices* 2nd." Boca Raton: CRC Press / Taylor & Francis. 210. 978-1-4200-5512-2.

Courault, D., R. Hadria, F. Ruget, A. Olioso, B. Duchemin, O. Hagolle, and G. Dedieu. 2010. "Combined Use of FORMOSAT-2 Images with a Crop Model for Biomass and Water Monitoring of Permanent Grassland in Mediterranean Region." *Hydrology and Earth System Sciences* 14 (9): 1731–1744. doi:10.5194/hess-14-1731-2010.

D'Andrimont, R., G. Lemoine, and M. Van der Velde. 2018. "Targeted Grassland Monitoring at Parcel Level Using Sentinels, Street-Level Images and Field Observations." *Remote Sensing 2018* 10 (8): 1300. doi:10.3390/RS10081300.

Davidson, A., S. Wang, and J. Wilmshurst. 2006. "Remote Sensing of Grassland-Shrubland Vegetation Water Content in the Shortwave Domain." *International Journal of Applied Earth Observation and Geoinformation* 8 (4): 225–236. doi:10.1016/j.jag.2005.10.002.

Drusch, M., U. Del Bello, S. Carlier, O. Colin, V. Fernandez, F. Gascon, B. Hoersch, et al. 2012. "Sentinel-2: ESA's Optical High-Resolution Mission for GMES Operational Services." *Remote Sensing of Environment* 120 (May): 25–36. DOI:10.1016/j.rse.2011.11.026.

Dusseux, P., T. Corpetti, and L. Hubert-Moy. 2013. "Temporal Kernels for the Identification of Grassland Management Using Time Series of High Spatial Resolution Satellite Images." In *International Geoscience and Remote Sensing Symposium (IGARSS)*, Melbourne, 3258–3260. 10.1109/IGARSS.2013.6723522.

Estel, S., S. Mader, C. Levers, P. H. Verburg, M. Baumann, and T. Kuemmerle. 2018. "Combining Satellite Data and Agricultural Statistics to Map Grassland Management Intensity in Europe." *Environmental Research Letters* 13 (7): 074020. doi:10.1088/1748-9326/aacc7a.

Frantz, D., E. Haß, A. Uhl, J. Stoffels, and J. Hill. 2018. "Improvement of the Fmask Algorithm for Sentinel-2 Images: Separating Clouds from Bright Surfaces Based on Parallax Effects." *Remote Sensing of Environment* 215 (September): 471–481. doi:10.1016/j.rse.2018.04.046.

Garioud, A., S. Giordano, S. Valero, and C. Mallet. 2019. Challenges in Grassland Mowing Event Detection with Multimodal Sentinel Images, 2019 10th International Workshop on the Analysis of Multitemporal Remote Sensing Images (MultiTemp), 5-7 Aug. 2019, Shanghai, China . Institute of Electrical and Electronics Engineers. doi:10.1109/Multi-Temp.2019.8866914.

Gensler, G. A. 1946. *Der Begriff Der Vegetationszeit*. *Diss*. (X) Samedan Und St. Moritz.

Gorelick, N., M. Hancher, M. Dixon, S. Ilyushchenko, D. Thau, and R. Moore. 2017. "Google Earth Engine: Planetary-Scale Geospatial Analysis for Everyone." *Remote Sensing of Environment* 202 (December): 18–27. doi:10.1016/j.rse.2017.06.031.

Grant, K., R. Siegmund, M. Wagner, and S. Hartmann. 2015. "Satellite-based assessment of grassland yields." *International Archives of the Photogrammetry, Remote Sensing and Spatial Information Sciences - ISPRS Archives*, Vol. XL-7/W3, 15–18. doi:10.5194/isprsarchives-XL-7-W3-15-2015. https://www.int-arch-photogramm-remote-sens-spatial-inf-sci.net/XL-7-W3/15/2015/

Griffiths, P., C. Nendel, J. Pickert, and P. Hostert. 2020. "Towards National-Scale Characterization of Grassland Use Intensity from Integrated Sentinel-2 and Landsat Time Series." *Remote Sensing of Environment* 238 (March): 111124. doi:10.1016/j.rse.2019.03.017.

Halabuk, A., M. Mojses, M. Halabuk, and S. David. 2015. "Towards Detection of Cutting in Hay Meadows by Using of NDVI and EVI Time Series." *Remote Sensing* 7 (5): 6107–6132. doi:10.3390/rs70506107.

Hardisky, M., V. Klemas, and M. Smart. 1983. "The Influence of Soil Salinity, Growth Form, and Leaf Moisture on the Spectral Radiance of Spartina Alterniflora Canopies." *Photogrammetric Engineering and Remote Sensing* 49: 77–83.

Herzon, I., T. Birge, B. Allen, A. Povellato, F. Vanni, K. Hart, G. Radley, et al. 2018. "Time to Look for Evidence: Results-Based Approach to Biodiversity Conservation on Farmland in Europe." *Land Use Policy* 71 (February): 347–354. doi:10.1016/j.landusepol.2017.12.011.

Hilpold, A., J. Seeber, V. Fontana, G. Niedrist, A. Rief, M. Steinwandter, E. Tasser, and U. Tappeiner. 2018. "Decline of Rare and Specialist Species across Multiple Taxonomic Groups after Grassland Intensification and Abandonment." *Biodiversity and Conservation* 27 (14): 3729–3744. doi:10.1007/s10531-018-1623-x.

Hird, J. N., and G. J. McDermid. 2009. "Noise Reduction of NDVI Time Series: An Empirical Comparison of Selected Techniques." *Remote Sensing of Environment* 113 (1): 248–258. doi:10.1016/J.RSE.2008.09.003.

Hua, X., P. Sirguey, and R. Ohlemüller. 2021. "Recent Trends in the Timing of the Growing Season in New Zealand's Natural and Semi-Natural Grasslands." *GIScience & Remote Sensing* 58 (7): 1090–1111. doi:10.1080/15481603.2021.1969629.

Huete, A., K. Didan, T. Miura, E. Patricia Rodriguez, S. Gao, and L. Guimarães Ferreira. 2002. "Overview of the Radiometric and Biophysical Performance of the MODIS Vegetation Indices." *Remote Sensing of Environment* 83 (1–2): 195–213. doi:10.1016/S0034-4257(02)00096-2.

Imran, H. A., D. Gianelle, D. Rocchini, M. P. M. Michele Dalponte, K. Sakowska, G. Wohlfahrt, L. Vescovo, and L. Vescovo. 2020. "VIS-NIR, Red-Edge and NIR-Shoulder Based Normalized Vegetation Indices Response to Co-Varying Leaf and Canopy Structural Traits in Heterogeneous Grasslands." *Remote Sensing* 12 (14): 2254. doi:10.3390/rs12142254.

Inglada, J., J. Francois Dejoux, O. Hagolle, and G. Dedieu. 2012. "Multi-Temporal Remote Sensing Image Segmentation of Croplands Constrained by a Topographical Database." *International Geoscience and Remote Sensing Symposium (IGARSS)*, 22-27 July 2012, Munich, Germany, 6781–6784. doi:10.1109/IGARSS.2012.6352607.

ISTAT, 2010. VI Censimento generale dell'Agricoltura. Roma: Italian National Institute of Statistics. https://www4.istat.it/it/censimento-agricoltura/agricoltura-2010

Jadunandan, D., and P. J. Curran. 2004. "The MERIS Terrestrial Chlorophyll Index." *International Journal of Remote Sensing* 25 (23): 5403–5413. doi:10.1080/0143116042000274015.

Jin, Z., and X. Bing. 2013. "A Novel Compound Smoother - RMMEH to Reconstruct MODIS NDVI Time Series." *IEEE Geoscience and Remote Sensing Letters* 10 (4): 942–946. doi:10.1109/LGRS.2013.2253760.

Johan, E., D. Kleijn, P. Batáry, M. Albrecht, A. Báldi, N. Blüthgen, E. Knop, A. Kovács-Hostyánszki, and H. G. Smith. 2020. "High Land-Use Intensity in Grasslands Constrains Wild Bee Species Richness in Europe." *Biological Conservation* 241 (January): 108255. doi:10.1016/j.biocon.2019.108255.

Jönsson, P., and L. Eklundh. 2004. "TIMESAT - A Program for Analyzing Time-Series of Satellite Sensor Data." *Computers & Geosciences* 30 (8): 833–845. doi:10.1016/j.cageo.2004.05.006.

Kaupo, V., T. Jagdhuber, A. Olesk, I. Hajnsek, and K. P. Papathanassiou. 2013. "Towards a Detection of Grassland Cutting Practices with Dual Polarimetric TerraSAR-X Data." *International Journal of Remote Sensing* 34 (22): 8081–8103. doi:10.1080/01431161.2013.829593.

Kim, J., S. Kang, B. Seo, A. Narantsetseg, and Y. Han. 2020. "Estimating Fractional Green Vegetation Cover of Mongolian Grasslands Using Digital Camera Images and MODIS Satellite Vegetation Indices." *GIScience & Remote Sensing* 57 (1): 49–59. doi:10.1080/15481603.2019.1662166.

Klaus, F., T. Tscharntke, J. Uhler, and I. Grass. 2021. "Calcareous Grassland Fragments as Sources of Bee Pollinators for the Surrounding Agricultural Landscape." *Global Ecology and Conservation* 26 (April): e01474. doi:10.1016/j.gecco.2021.e01474.

Kolecka, N., C. Ginzler, R. Pazur, B. Price, and P. H. Verburg. 2018. "Regional Scale Mapping of Grassland Mowing Frequency with Sentinel-2 Time Series." *Remote Sensing* 10 (8): 1221. doi:10.3390/rs10081221.

Lobert, F., A.-K. Holtgrave, M. Schwieder, M. Pause, J. Vogt, A. Gocht, and S. Erasmi. 2021. "Mowing Event Detection in Permanent Grasslands: Systematic Evaluation of Input Features from Sentinel-1, Sentinel-2, and Landsat 8 Time Series." *Remote Sensing of Environment* 267 (December): 112751. doi:10.1016/J.RSE.2021.112751.

Marcolini, G., A. Bellin, M. Disse, and G. Chiogna. 2017. "Variability in Snow Depth Time Series in the Adige Catchment." *Journal of Hydrology: Regional Studies* 13 (October): 240–254. doi:10.1016/J.EJRH.2017.08.007.

Mathilde De, V., J. Radoux, and P. Defourny. 2021. "Grassland Mowing Detection Using Sentinel-1 Time Series: Potential and Limitations." *Remote Sensing* 13 (3): 1–19. doi:10.3390/rs13030348.

Oenema, O., C. De Klein, and M. Alfaro. 2014. "Intensification of Grassland and Forage Use: Driving Forces and Constraints." *Crop and Pasture Science*, Vol. 65, 524–537. Clayton, Australia: CSIRO. doi:10.1071/CP14001.

Pe'er, G., L. V. Dicks, P. Visconti, R. Arlettaz, A. Báldi, T. G. Benton, S. Collins, et al. 2014. "EU Agricultural Reform Fails on Biodiversity." *Science* 344 (6188): 1090–1092. doi:10.1126/science.1253425.

Pe'er, G., S. Lakner, R. Müller, G. Passoni, V. Bontzorlos, D. Clough, and F. Moreira, et al. 2017. "Is the CAP Fit for purpose? An evidence-based fitness-check assessment." Leipzig, German: German Centre for Integrative Biodiversity Research (iDiv) Halle-Jena-Leipzig. https://www.idiv.de/fileadmin/content/iDiv_Files/Documents/peer_et_al_2017_cap_fitness_check_final_20-11.pdf

Peng, Y., A. Nguy-Robertson, T. Arkebauer, and A. A. Gitelson. 2017. "Assessment of Canopy Chlorophyll Content Retrieval in Maize and Soybean: Implications of Hysteresis on the Development of Generic Algorithms." *Remote Sensing* 9 (3): 226. doi:10.3390/rs9030226.

Planet Team. 2018. "Planet Application Program Interface: In Space for Life on Earth." https://api.planet.com .

QGIS Development Team. 2021. *QGIS 3.16. Geographic Information System User Guide*. Grüt, Switzerland: QGIS Association.

Qian, Y., K. Zhang, and F. Qiu. 2005. "Spatial Contextual Noise Removal for Post Classification Smoothing of Remotely Sensed Images." *Proceedings of the ACM Symposium on Applied Computing*, March 13 - 17, 2005, Santa Fe New Mexico 1: 524–528. doi:10.1145/1066677.1066795.

Reinermann, S., S. Asam, and C. Kuenzer. 2020. "Remote Sensing of Grassland Production and Management-A Review." *Remote Sensing* 12 (12): 1949. doi:10.3390/rs12121949.

Reynolds, S., and J. Frame. 2005. *Grasslands: Developments, Opportunities, Perspectives*. Enfield, New Hampshire: Science Publishers.

Rouse, J. W., R. Haas, J. Schell, and D. Deering. 1974. "Monitoring Vegetation Systems in the Great Plains with ERTS." *NASA Special Publication* 351 (1974): 309.

Sakowska, K., R. Juszczak, and D. Gianelle. 2016. "Remote Sensing of Grassland Biophysical Parameters in the Context of the Sentinel-2 Satellite Mission." *Journal of Sensors* 2016: 1–16. doi:10.1155/2016/4612809.

Sboarina, A., A. Cescatti, C. Sboarina, and A. Cescatti. 2004. "Il Clima Del Trentino–Distribuzione Spaziale Delle Principali Variabili Climatiche Report 33." *Centro Di Ecologia Alpina Monte Bondone*.

Schwieder, M., M. Wesemeyer, D. Frantz, K. Pfoch, S. Erasmi, J. Pickert, C. Nendel, and P. Hostert. 2021. "Mapping Grassland Mowing Events across Germany Based on Combined Sentinel-2 and Landsat 8 Time Series." *Remote Sensing of Environment* November. 112795. doi:10.1016/J.RSE.2021.112795.

Scotton, M., L. Sicher, and A. Kasal. 2014. "Semi-Natural Grasslands of the Non Valley (Eastern Italian Alps): Agronomic and Environmental Value of Traditional and New Alpine Hay-Meadow Types." *Agriculture, Ecosystems & Environment* 197 (December): 243–254. doi:10.1016/J.AGEE.2014.08.003.

Siegmund, R., S. Redl, M. Wagner, and S. Hartmann. 2019. "Grassland Monitoring Based on Sentinel-1." In *Proceedings of the Remote Sensing for Agriculture, Ecosystems, and Hydrology XXI, Strasbourg, France*, 21 October 2019; *Volume 11149*, 19. SPIE-Intl Soc Optical Eng. 10.1117/12.2532801.

Stendardi, L., S. Rune Karlsen, G. Niedrist, R. Gerdol, M. Zebisch, M. Rossi, and C. Notarnicola. 2019. "Exploiting Time Series of Sentinel-1 and Sentinel-2 Imagery to Detect Meadow Phenology in Mountain Regions." *Remote Sensing* 11 (5): 542. doi:10.3390/RS11050542.

Streifeneder, T., U. Tappeiner, F. V. Ruffini, G. Tappeiner, and C. Hoffmann. 2007. "Selected Aspects of Agro-Structural Change within the Alps." *Revue de Géographie Alpine* September (95–3): 41–52. doi:10.4000/rga.295.

Stumpf, F., M. K. Schneider, A. Keller, A. Mayr, T. Rentschler, R. G. Meuli, M. Schaepman, and F. Liebisch. 2020. "Spatial Monitoring of Grassland Management Using Multi-Temporal Satellite Imagery." *Ecological Indicators* 113 (June): 106201. doi:10.1016/j.ecolind.2020.106201.

Tamm, T., K. Zalite, K. Voormansik, and L. Talgre. 2016. "Relating Sentinel-1 Interferometric Coherence to Mowing Events on Grasslands." *Remote Sensing* 8 (10): 802. doi:10.3390/rs8100802.

Taravat, A., M. Wagner, and N. Oppelt. 2019. "Automatic Grassland Cutting Status Detection in the Context of Spatiotemporal Sentinel-1 Imagery Analysis and Artificial Neural Networks." *Remote Sensing* 11 (6): 711. doi:10.3390/rs11060711.

Tasser, E., J. Walde, U. Tappeiner, A. Teutsch, and W. Noggler. 2007. "Land-Use Changes and Natural Reforestation in the Eastern Central Alps." *Agriculture, Ecosystems & Environment* 118 (1–4): 115–129. doi:10.1016/j.agee.2006.05.004.

Velthof, G., J. Peter Lesschen, R. Schils, A. Smit, B. Elbersen, G. Hazeu, S. Mucher, and O. Oenema. 2014. "*Grasslands Areas, Production and Use.*" Wageningen: Alterra Wageningen UR.

Voormansik, K., T. Jagdhuber, K. Zalite, M. Noorma, and I. Hajnsek. 2016. "Observations of Cutting Practices in Agricultural Grasslands Using Polarimetric SAR." *IEEE Journal of Selected Topics in Applied Earth Observations and Remote Sensing* 9 (4): 1382–1396. doi:10.1109/JSTARS.2015.2503773.

Wachendorf, M., T. Fricke, and T. Möckel. 2018. "Remote Sensing as aTool to Assess Botanical Composition, Structure, Quantity and Quality of Temperate Grasslands." *Grass and Forage Science* 73: 1–14. doi:10.1111/gfs.12312.

Whitcraft, A. K., E. F. Vermote, I. Becker-Reshef, and C. O. Justice. 2015. "Cloud Cover Throughout the Agricultural Growing Season: Impacts on Passive Optical Earth Observations." *Remote Sensing of Environment* 156 (January): 438–447. doi:10.1016/J.RSE.2014.10.009.

Xiaojun, N., W. Xiaodan, L. Suzhen, G. Shixian, and L. Haijun. 2010. "137Cs Tracing Dynamics of Soil Erosion, Organic Carbon and Nitrogen in Sloping Farmland Converted from Original Grassland in Tibetan Plateau." *Applied Radiation and Isotopes* 68 (9): 1650–1655. doi:10.1016/j.apradiso.2010.04.017.

Yan, X., L. Jing, Y. Shao, H. Zhenqi, Z. Yang, S. Yin, and L. Cui. 2020. "Driving Forces of Grassland Vegetation Changes in Chen Barag Banner, Inner Mongolia." *GIScience & Remote Sensing* 57 (6): 753–769. doi:10.1080/15481603.2020.1794395.

Zalite, K., O. Antropov, J. Praks, K. Voormansik, and M. Noorma. 2016. "Monitoring of Agricultural Grasslands with Time Series of X-Band Repeat-Pass Interferometric SAR." *IEEE Journal of Selected Topics in Applied Earth Observations and Remote Sensing* 9 (8): 3687–3697. doi:10.1109/JSTARS.2015.2478120.

Zarei, A., E. Asadi, A. Ebrahimi, M. Jafari, A. Malekian, H. Mohammadi Nasrabadi, A. Chemura, and G. Maskell. 2020. "Prediction of Future Grassland Vegetation Cover Fluctuation under Climate Change Scenarios." *Ecological Indicators* 119. doi:10.1016/j.ecolind.2020.106858.

Appendix 1: Abbreviations

CPiMF: Corrected Pixel Mowing Frequency
EVI: Enhanced Vegetation Index
GEE: Google Earth Engine platform
GVMI: Global Vegetation Moisture Index
MAE: Mean Absolute Error
MTCI: MERIS Terrestrial chlorophyll index
MTS: Maximum Time Series
NDB: N Days Backward
NDII: Normalized Difference Infrared Index
NDVI: Normalized Difference Vegetation Index
NDW: N Days Window
PaMF: Parcel Mowing Frequency
PiMF: Pixel Mowing Frequency
RENDVI: Red edge Normalized Difference Vegetation Index
RI: Resampling Interval
RS: Remote Sensing
RTS: Resampled Time Series
S2: Sentinel-2
SAR: Synthetic Aperture Radar
STS: Smoothed Time Series
VIs: Vegetation Indices
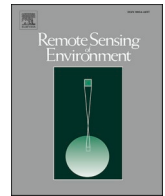VITS: Vegetation Index Time Series.

Study III

Extracting flowering phenology from grassland species mixtures using time-lapse cameras

Davide Andreatta, Christoph Bachofen, Michele Dalponte, Valentin H. Klaus, Nina Buchmann

Please refer to the online version for the supplementary materials

Contents lists available at ScienceDirect

Remote Sensing of Environment

Extracting flowering phenology from grassland species mixtures using time-lapse cameras

Davide Andreatta [a,b,*], Christoph Bachofen [c,d], Michele Dalponte [b], Valentin H. Klaus [e,f], Nina Buchmann [e]

[a] *Department of Agronomy, Food, Natural Resources, Animals and Environment, University of Padova, Legnaro, Padova, Italy*
[b] *Research and Innovation Centre, Fondazione Edmund Mach, San Michele all'Adige, Trento, Italy*
[c] *Plant Ecology Research Laboratory PERL, School of Architecture, Civil and Environmental Engineering, EPFL, Lausanne, Switzerland*
[d] *Functional Plant Ecology, Community Ecology Unit, Swiss Federal Institute for Forest, Snow and Landscape WSL, Birmensdorf, Switzerland*
[e] *Institute of Agricultural Sciences, Department of Environmental Systems Science, ETH Zürich, Zürich, Switzerland*
[f] *Forage Production and Grassland Systems, Agroscope, Zürich, Switzerland*

ARTICLE INFO

ABSTRACT

Understanding the impacts of climate change on plant phenology is crucial for predicting ecosystem responses. However, accurately tracking the flowering phenology of individual plant species in grassland species mixtures is challenging, hindering our ability to study the impacts of biotic and abiotic factors on plant reproduction and plant-pollinator interactions. Here, we present a workflow for extracting flowering phenology from grassland species mixtures using near-surface time-lapse cameras. We used 89 image series acquired in plots with known species composition at the Jena trait-based experiment (Germany) to develop random forest classifiers, which were used to classify images and compute time series of flower cover for each species. The high temporal resolution of time-lapse cameras allowed to select images in proper light conditions, and to extract vegetation indices and texture metrics to improve discrimination among flowering species. The random forest classifiers showed a high accuracy in predicting the cover of *Leucanthemum vulgare, Ranunculus acris,* and *Knautia arvensis* flowers, whereas graminoid flowers were harder to predict due to their green-to-brownish colours. The proposed workflow can be applied in climate change studies, ecosystem functioning, plant community ecology, and biodiversity change research, including the investigation of effects of species richness on individual species' flowering phenology. Our method could be a valuable tool for understanding the impacts of climate change on plant reproduction and ecosystem dynamics.

1. Introduction

Global change affects plant communities and their functioning in various ways. Consistent changes in the timing of phenological events are clear indicators of the impact of global change on plant life cycles (Piao et al., 2008; Schwartz, 2013). For instance, warming tends to advance the green-up and to delay the end of the vegetation growing season (Estiarte and Peñuelas, 2015; Liu et al., 2020; Menzel et al., 2006; Shen et al., 2011). However, recent studies revealed that the analysis of

phenology at whole-ecosystem scale is not always suitable for describing the effect of global change on individual plant species, because phenological responses to climate change can differ among species of the same ecosystem (Thackeray et al., 2016). Furthermore, Collins et al. (2021) challenged the expectation that all phenological events will advance in unison to warming. Instead, they observed that vegetative and reproductive phenology are differentially affected by experimental warming, suggesting that different aspects of phenology should be separately investigated. Moreover, it was observed that many plant species

flowered earlier in response to reductions in diversity, so that declining diversity could exacerbate phenological changes attributed to rising global temperatures (Wolf et al., 2017). To further investigate these multifaceted processes, there is an increasing need for effective methods to track single species flowering phenology in species mixtures.

Thanks to their planetary-scale analysis capabilities and short revisiting time, remote sensing (RS) and proximal sensing are opening new possibilities for phenological studies, overcoming laborious and time-consuming ground-based vegetation observations (Szigeti et al., 2016). The large-scale observation potential of RS has been applied to track vegetation reproductive phenology (Gonzales et al., 2022), but the coarse spatial resolution of satellite images restricts flowering estimation to massive homogeneous flowering events in rather homogeneous ecosystems such as of eucalypt species (Dixon et al., 2021), oil seed rape fields (d'Andrimont et al., 2020), almond (Chen et al., 2019) and pear plantations (Wouters et al., 2013). Flowers of different functional groups were mapped for the first time by Landmann et al. (2015), in African savannas using hyperspectral imagery. Images at finer spatial resolution captured by drones recently allowed Gallmann et al. (2022) to recognize flower species in permanent grasslands, a task that would not have been possible with satellite-resolution images. Frequent (sub-weekly) drones flights, however, are usually too expensive for agricultural and ecological phenological studies, and other technologies are therefore needed.

PhenoCams (PCs), i.e., digital cameras configured to capture time-lapse images, can bridge the gap between satellite monitoring and traditional ground-based vegetation observations (Brown et al., 2016; D'Odorico et al., 2015; Richardson et al., 2010). Compared to RS, PC imagery can provide a very fine temporal and spatial resolution, allowing to explore the inter- and intraspecific variability in plant phenology at a sub-daily scale to a much lower cost than repeated drone flights. However, only in 2022, PC images were used for the first time to map flowering phenology of two Arctic species, the mountain avens *Dryas octopetala* and *Dryas integrifolia* (Mann et al., 2022). For more complex ecosystems, such as multi-species and multi-layered grasslands, different automation routines and analysis processes still need to be developed.

Tracking floral phenology using time-lapse camera in grasslands is challenging due to many reasons: i) images are acquired under various light conditions, ii) sensors usually measure reflectance values only in the visible spectral region, iii) flower structures are relatively small and only cover a few pixels, iv) flowers might be occluded by vegetative plant parts, and v) grasslands are biodiversity rich compared to other ecosystems, to name a few (Andrew and Ustin, 2008; Gallmann et al., 2022; Mann et al., 2022). Even though PC imagery has been used in phenological studies at whole-ecosystem scale to track greenness, and despite floral phenology (typically determined manually) being a key trait of grasslands ecosystems, no processing workflow to track flowering phenology in grasslands has been proposed so far. Nevertheless, a workflow to extract flower cover time series (FCTS) from PC imagery is urgently needed to, for example, study the response of reproductive phenology to environmental and biotic drivers. Moreover, such a workflow could easily be applied to different questions of biodiversity and climate impact research as well as land management to assess plant-pollinator interactions, grasslands cultural services evaluation, and grassland productivity monitoring, providing important inputs to vegetation and biogeochemical models (Inouye, 2020; Richardson et al., 2012; Wolf et al., 2017).

Here, we suggest a processing workflow to extract FCTS from RGB time-lapse cameras (RGB as Red, Green, Blue digital numbers). To address the aforementioned challenges, we i) leveraged the high temporal resolution of PC imagery by selecting only images in proper light condition, ii) based our classification on vegetation indices derived from RGB reflectance, iii) included texture metrics to improve discrimination among flower species by their shapes. More specifically, we applied image filtering, calculated features of selected pixels (vegetation indices and texture metrics), and then used the subset of features with highest

accuracy to train random forest classifiers. Finally, we extracted FCTS and derived phenological metrics for single or groups of plant species. We present an example application on experimental grassland plots of different diversity levels.

2. Materials and methods

2.1. Study site

Images used in this study were acquired in 2014 within the Trait-Based Biodiversity Experiment (TBE; Ebeling et al., 2014) at the field site of the Jena Experiment (Thuringia, Germany; 50°55 N, 11°35 E, 130 m a.s.l.) (Roscher et al., 2005). The TBE was established in 2010 following a design which covers gradients in plant species and functional richness, ranging from 1 to 8 species in 138 plots (3.5 m × 3.5 m). Species not belonging to the initially sown species pool were weeded every year in April, July and October to maintain the species richness gradient. Grasslands were mowed two times per year to mimic local traditional management. We included 89 plots, covering the whole species richness gradient. Selected plots were sown with a combination of 13 species, of which seven were grasses: *Anthoxanthum odoratum, Avenula pubescens, Dactylis glomerata, Festuca rubra, Holcus lanatus, Phleum pratense, Poa pratensis;* and six were forbs: *Centaurea jacea, Geranium pratense, Knautia arvensis*, *Leucanthemum vulgare*, *Plantago lanceolata,* and *Ranunculus acris.* Selected species were cultivated as monocultures (14 plots), in 2-species mixtures (32 plots), in 3-species mixtures (23 plots), in 4-species mixtures (18 plots), and in 8-species mixtures (2 plots).

2.2. Image acquisition

In spring 2014, 92 time-lapse cameras (TLC 100, Brinno) were installed on 1.5 m poles pointing north at 60° angle from horizontal, capturing an area of 3.5 m^2 in each frame. Images were recorded hourly during daylight according to the automatic mode of the cameras from April 12th through August 22nd, 2014 (Fig. 1). Here, we focus on the spring growing period, i.e., between the spring weeding (April 24th) and the first mowing (May 29th). Plots 20, 27 and 33 of the TBE plots were discarded because of failure in image collection. A total of 52′678 images stored in jpg format (1280 × 1040 pixels) were considered in the study.

2.3. Workflow for data processing

The proposed workflow (Fig. 2) can be divided in four main phases: 1) image selection and pixel labelling, 2) feature computation, 3) feature selection and final classifier compilation, 4) FCTS extraction, smoothing and calculation of phenological metrics. All analyses were performed with the R version 4.3.0 (R Core Team, 2023).

2.3.1. Image selection and pixel labelling (phase 1)

In Phase 1, image selection phase aimed at increasing the spectral separability between six pixel classes. *C. jacea* and *G. pratense* did not flower during the spring and could therefore not be considered in the analyses, while the green-greyish *P. lanceolata* flowers were not big enough to be labelled separately from "Green vegetation". The graminoid species were combined for the flower identification because their flowers were not distinguishable, whereas the other three flowering species (*R. acris*, *K. arvensis*, and L. *vulgare*) were considered separately. The resulting classes used for labelling elements inside the plots were: "Green vegetation", "Soil", "Graminoids flowers", "*K. arvensis* flowers", "*L. vulgare* flowers", "*R. acris* flowers". Light conditions heavily affect pixel colours: images with high brightness were usually foggy, and images with high contrast were usually acquired in direct sunlight conditions. We calculated brightness and contrast for all images using the "extractVIs" function of the R package "Phenopix" (Filippa et al., 2016) and tested which brightness and contrast combinations allow the

Fig. 1. Examples of analysed images. Left: Plot where *G. pratense, H. lanatus, P. pratense* and *P. lanceolata* were sown; image acquired May 27th, 2014. Right: Plot where *C. jacea, K. arvensis* and *L. vulgare* were sown; image acquired May 23th, 2014.
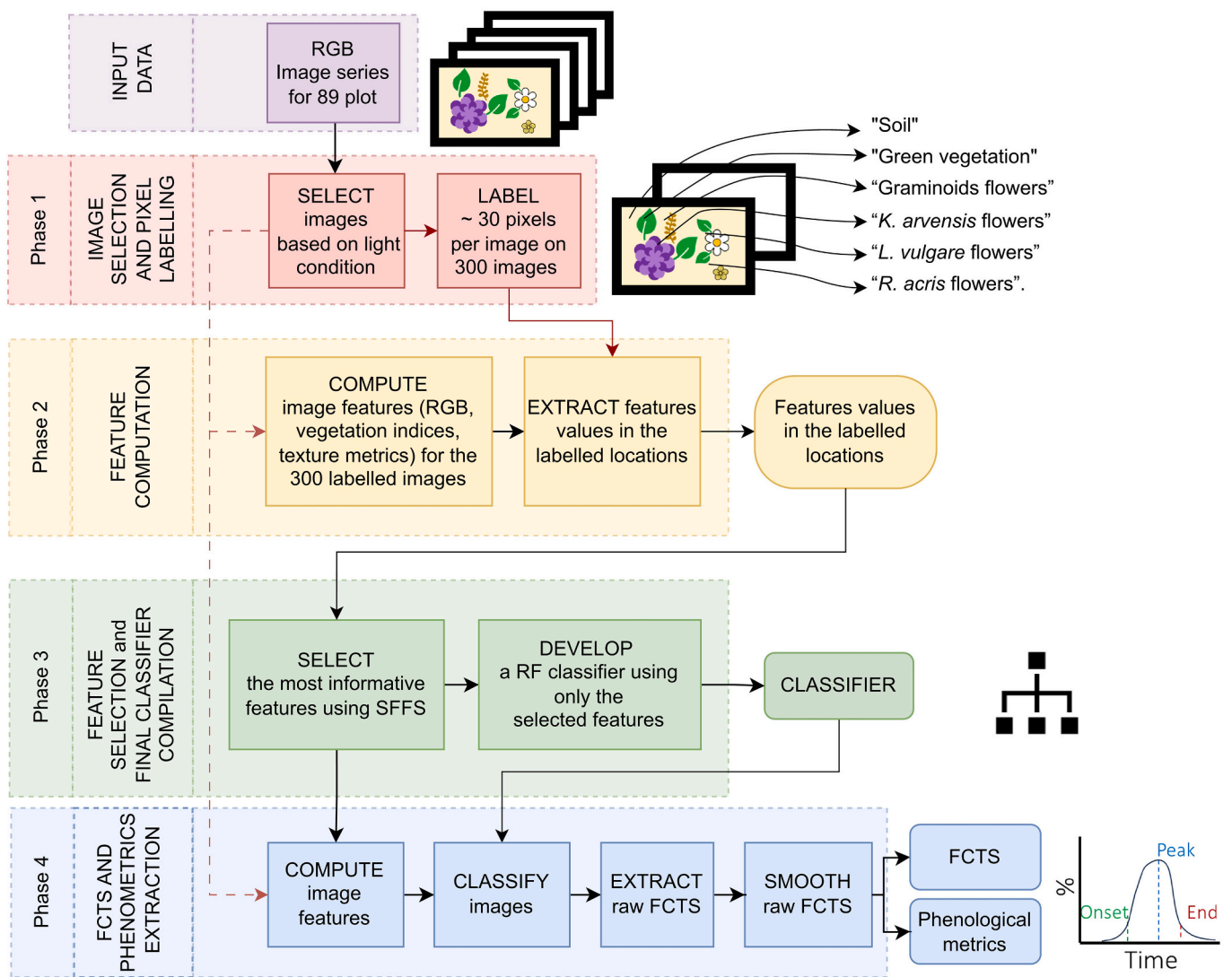

Fig. 2. Structure of the proposed workflow with four phases to extract flower phenology from PhenoCam pictures of a grassland biodiversity experiment. Abbreviations are as follows: RF = Random Forest; SFFS = Sequential Floating Forward Selection; FCTS = Flower Cover Time Series.

selection of images acquired in homogeneous light conditions. Images with uniform light conditions were retrieved by selecting brightness and contrast between the 10th and the 40th percentile within a 3-day window. The selection of the best images within this 3-day window avoided including images taken on days with sub-optimal observations (e.g., all foggy or high contrast images).

To develop a labelled dataset, 300 images were randomly selected (60 images in the period between Apr 24 and May 5; 60 images between May 6 and May 18; 180 images between May 19 and May 29, 2014). For each image, a 200 pixels × 200 pixels image patch was randomly selected and plotted in RGB colours using the "plotRGB" function of the "raster" package (Hijmans, 2022). Around 30 pixels per image were labelled by clicking on the image to retrieve the x and y coordinates using the "locator" function of the "graphics" package and assigning to each pixel the class to which it belongs (see subsection 2.1). To prevent duplicated pixels after downscaling the images (see the subsequent section for downscaling details), any labelled pixels that were within a distance of eight pixels from one another were removed from the dataset. The labelling phase resulted in a table where the class and pixel coordinates were stored.

2.3.2. Feature computation (phase 2)

To increase the spectral separability of pixels between different classes, we computed RGB-based features: vegetation indices and texture metrics, described in detail in Table 1. We selected four vegetation indices well established in colour analysis literature (Lussem et al., 2018; Zhao, 2021). For pixels with a specific shade of purple colour, the calculation of the Visible Atmospherically Resistant Index (VARI) resulted in infinite values (for definition, see Table 1). Since only

Table 1

Image features tested for Phase 2. $P_{i,j}$ is the probability of values i and j occurring in adjacent pixels in the original image within the window defining the neighbourhood. i and j are the labels of the columns and rows (respectively) of the co-occurrence matrixes. Because of the construction of the co-occurrence matrixes, i refers to the value of a target pixel, and j is the value of its immediate neighbour (Rook's case).

Feature name	Equation	Reference
Red Digital Number	R	
Green Digital Number	G	
Blue Digital Number	B	
RGBVI (Red Green Blue Vegetation Index)	$\dfrac{((G^2)-(R*B))}{((G^2)+(R*B))}$	Bendig et al. (2015)
GLI (Green Leaf Index)	$\dfrac{(2*G-R-B)}{(2*G+R+B)}$	Louhaichi et al. (2001)
VARI (Visible Atmospherically Resistant Index)	$\dfrac{(G-R)}{(G+R-B)}$	Gitelson et al. (2002)
NGRDI (Normalised Green Red Difference Index)	$\dfrac{(G-R)}{(G+R)}$	Tucker (1979)
Homogeneity	$\sum_{i,j=0}^{N-1}\dfrac{P_{i,j}}{1+(i-j)^2}$	Haralick et al. (1973)
Contrast	$\sum_{i,j=0}^{N-1}P_{i,j}(i-j)^2$	Haralick et al. (1973)
Dissimilarity	$\sum_{i,j=0}^{N-1}P_{i,j}|i-j|$	Haralick et al. (1973)
Entropy	$\sum_{i,j=0}^{N-1}P_{ij}\left(-lnP_{i,j}\right)$	Haralick et al. (1973)
Second Moment	$\sum_{i,j=0}^{N-1}P_{i,j}^2$	Haralick et al. (1973)
Mean	$\mu=\sum_{i,j=0}^{N-1}i(P_{i,j})$	Haralick et al. (1973)
Variance	$\sigma^2=\sum_{i,j=0}^{N-1}P_{i,j}(1-\mu)^2$	Haralick et al. (1973)

finite values can be used for classifier development, infinite VARI values were replaced with the highest finite value sampled (or lowest in case of negative infinite values), which occurred in <0.1% of the labelled pixels. The image textures were derived from co-occurrence matrices for each colour band, since we expected that the flower colours differed from the background (green vegetation or soil) surfaces (Guru et al., 2010), using the "glcm" package in R Studio (Zvoleff, 2020; Haralick et al., 1973). Homogeneity, Contrast, Dissimilarity, Entropy, Second Moment, Mean, and Variance were computed in four directions (0°, 45°, 90° and 135°) and then averaged to one rotation-invariant texture as commonly used in texture analysis (e.g., Guru et al., 2010). For the computation of texture metrics, we needed to define the size of the window used for co-occurrence matrices. Moreover, downscaling the images to a lower resolution before feature extraction can give the best detection accuracy while also vastly increasing processing speed compared to higher resolution images (Mann et al., 2022). We tested the influence of window size and downscaling factor on classification accuracy and processing time, and found that a downscaling factor equal to four and a window size equal to eleven resulted in the highest accuracy (Fig. S1). Processing time of the downscaled image (4 × 4 pixels) was 16 times shorter than the processing time of the full resolution image (24 s per image vs. 395 s per image, respectively). The feature values of the labelled pixels were then extracted. The feature computation phase resulted in a table where class, and features values of the labelled pixels were stored.

2.3.3. Feature selection and final classifier development (phase 3)

In Phase 3, we selected a set of best suitable features to optimize processing time, and to reduce redundancy of highly correlated features. Decreasing the number of features typically increases the classifier generalisation capability, because it avoids overfitting (Ho, 1995). First, we randomly assigned 70% of images for training, and 30% of images for validation. Validating a classifier on a separate part of the dataset is a common technique used to evaluate the performance of the classifier and to avoid overfitting. For the feature selection, we used the training dataset and applied the "varSelSFFS" function from the "varSel" package, which performs feature selection using the Sequential Forward Floating Selection search strategy and the Jeffries-Matusita distance (Bruzzone et al., 1995; Dalponte and Ørka, 2021; Pudil et al., 1994). The Jeffries-Matusita distance saturates at square root of two, when including a new feature does not increase class separation. Thus, the number of features to select was defined according to the saturation, as described in Richards and Jia (2006). In addition, we investigated the capability of RGB bands, vegetation indices, and texture metrics to distinguish classes. For this, we compared the accuracies of RF models trained on different subsets of features from the training dataset, including: i) features selected by SFFS, ii) RGB bands alone, iii) RGB bands combined with vegetation indices, iv) RGB bands combined with texture metrics, and v) all features. The accuracies were measured on the validation dataset.

To perform RF classifications, we used the "randomForest" function of the "randomForest" package (Liaw and Wiener, 2002). The metric to calculate the accuracy of the RF classifiers was the mean F1 score of the six classes. The F1 score is derived from precision and recall metrics as described in eq. 1. The precision is intuitively the ability of the classifier not to label a sampled pixel as positive when it is negative, whereas the recall is the ability of the classifier to find all the positive sampled pixels. Precision and recall are described in eqs. 2 and 3, where *tp* is the number of true positives, *tn* is the number of true negatives, *fp* the number of false positives, and *fn* the number of false negatives. All the described metrics have their best score at 1 and their worst score at 0 (Congalton and Green, 2009).

$$F1 = \frac{2*(precision*recall)}{precision + recall} \tag{1}$$

$$precision = \frac{tp}{tp + fp} \quad (2)$$

$$recall = \frac{tp}{tp + fn} \quad (3)$$

We calculated the processing time for the calculation of all features and subsequent image classification for one image. For this, we used one core of an AMD Ryzen 73,700 U processor (CPU, 2300 MHz) with 16 GB RAM, and 500 GB solid-state drive storage device. The feature combination providing the best trade-off between accuracy and processing time was selected for the RF final classifier compilation.

2.3.4. Extraction of flower cover time series and phenological metrics (phase 4)

Once the final RF classifier had been trained, the percentage of pixels in each class was computed for each image. For this, images were selected (see section 2.3.1), for each image the selected features were computed, and percentages of each class within each image were calculated using the RF classifier developed in subsection 2.3.3. We identified and removed outliers from the derived flower cover time series using the "tsclean" function of the "forecast" R package which is based on Friedman's SuperSmoother for non-seasonal series (Hyndman and Khandakar, 2008). Values were aggregated at daily temporal resolution by taking the arithmetic mean. A Local Polynomial Regression function was fitted to smooth the time series using the "loess" function of the "stats" package (R Core Team, 2023). Time series calculated from nine TBE plots were displayed and analysed to show the potential applications and limitations of the proposed workflow. To obtain further insights into the reliability of FCTS, we conducted an analysis of flower cover of species that were not sown in each plot. For each image series (i.e., for each plot), we identified the predicted FCTS of unsown species, e.g., the predicted FCTS of L.
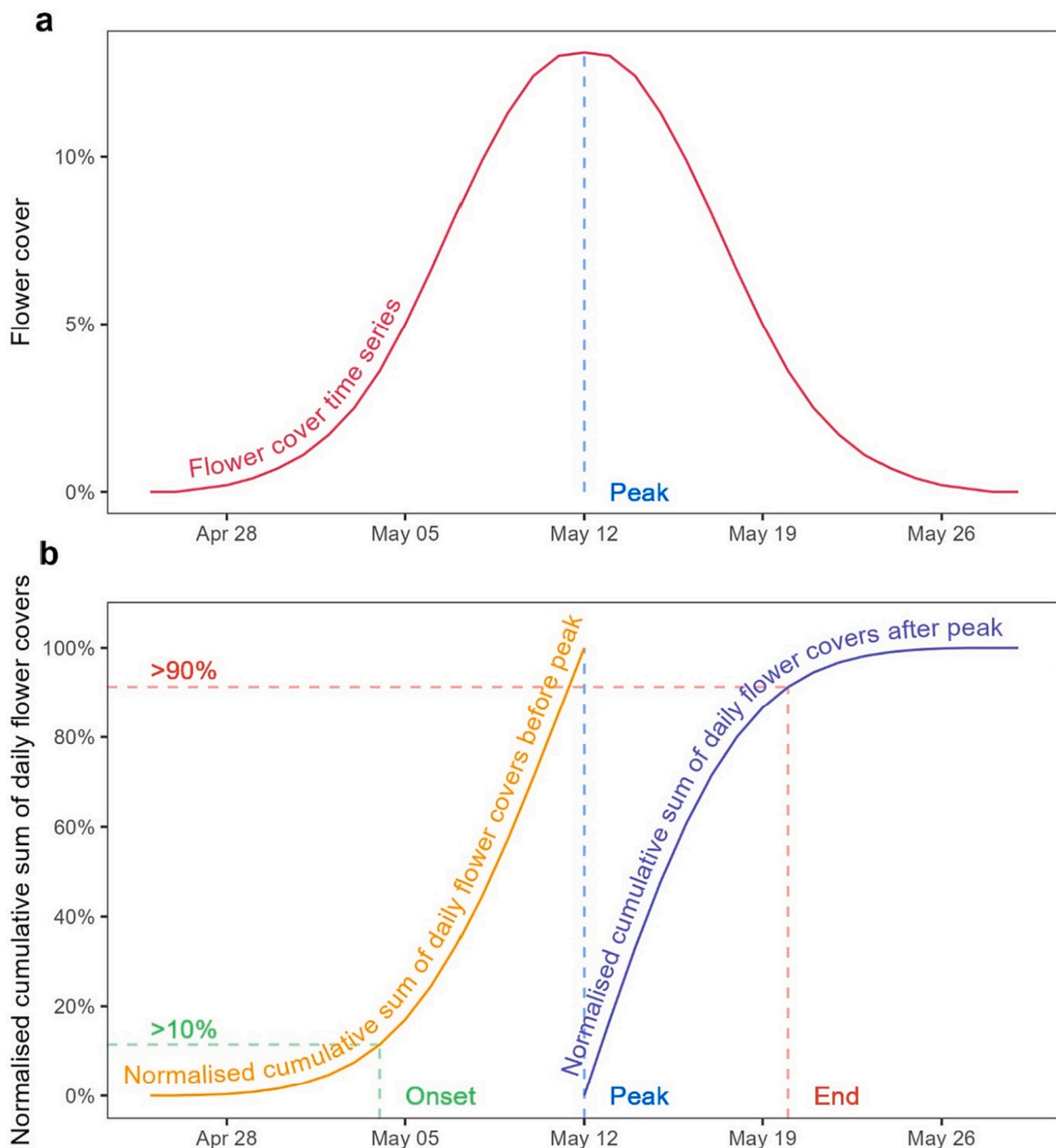

Fig. 3. Identification of flowering phenological metrics based on time-lapse cameras. Panel a: Example of flower cover time series. Panel b: Flowering phenological metrics identification for the flower cover time series in panel a; onset was defined as the first day above 10% of the normalised cumulative sum of daily flower covers before the peak; end of the season was identified as the first day above 90% of the normalised cumulative sum of daily flower covers after the peak. Both approaches allow determination of onset and end of season when logistics or management prohibited recording the full flowering season (see main text).

vulgare in plots where L. *vulgare* was not sown.

For each FCTS, onset, peak, and end of flowering were extracted. The peak was identified as the day of maximum in the FCTS, when the value was higher than the values before and after it. The onset of flowering was identified on the basis of the normalised cumulative sum of daily flower covers before the peak, whereas the end of flowering was identified on the basis of the normalised cumulative sum of daily flower covers after the peak. This allowed the identification of flowering onset in FCTS when the end of the flowering was not observable (e.g., because of mowing) as well as the identification of the end of flowering in FCTS when the onset of flowering was not observable (e.g. image acquisition started later). The cumulative sums were min-max normalised (0%–100%), and the onset was defined as the first day when the normalised cumulative sum of daily flower cover exceeded 10% (Fig. 3). Moreover, the end of the season was identified as the first day when the normalised cumulative sum of daily flower cover after the peak exceeds 90%. The 10% and 90% thresholds were chosen as a compromise between robustness against outliers and timely identification of changes. The onset of flowering was determined exclusively for FCTS exhibiting a low flower cover ($< 1\%$) at the start of the observation period to avoid errors in plots for which the observation period started after the onset of flowering. Similarly, the end of flowering was defined exclusively for FCTS with a low flower cover ($< 1\%$) at the end of the observation period to prevent the mischaracterization of the end of flowering in plots for which the observation period ended prior to the end of flowering. We expected a flower cover of unsown species above 0% due to wrongly classified pixels and therefore did not extract phenological metrics from time series for which the peak of the sown species was lower than 1% to avoid potential misclassification. The phenological metrics of single species that were calculated with this approach can easily be compared between treatments (i.e., multiple image time-series), and summary statistics can be derived from multiple plots, such as mean and standard deviation as well as further statistical analyses.

3. Results

With the proposed workflow we were able to successfully develop a RF model tailored to the recorded PC images, and thereby extract flower cover time-series and flowering phenology metrics of single species or groups of species from 89 image series. After the image selection based on light conditions in Phase 1 (see Fig. 2), there were on average more than three valid images per day per plot. The median number of images per plot in the period of interest was thereby reduced from 592 to 137 images per plot, leaving in total 11′472 images out of the originally 52′678. Tables and figures showing image availability before and after image selection are available in the supplementary material (Fig. S2, Table S1, Table S2).

The dataset used for the RF classifiers training and validation consisted of 9073 pixels. The "Green vegetation" class was the most represented, with 4281 pixels from 300 images. 1184 pixels were labelled as "Soil" from 139 images, 1570 pixels were labelled as "Graminoids flowers" from 115 images, 1160 as "*L. vulgare* flowers" from 65 images, 506 as "*K. arvensis* flowers" from 36 images, and 372 as "*R. acris* flowers" from 40 images. The average number of labelled pixels per image was 30. Labelling 9073 pixels in 300 images took around 300 min (labelled pixels highlighted on RGB images are available as supplementary materials in the ETH Zurich repository).

The distribution of pixel classes in the RGB space (Fig. 4) suggested a good spectral separability of some classes (e. g., "*R. acris* flowers" vs. "*K. arvensis* flowers"; "Green vegetation" vs "*R. acris* flowers"), whereas some other spectral signatures were not easily distinguishable in the RGB space (e.g., "Soil" vs. "Graminoids flowers" vs. "*K. arvensis* flowers"). The classifier developed using RGB bands resulted in an accuracy of 0.791 (Table 2). The addition of vegetation indices and texture

Table 2
Accuracy (mean F1 score of the six classes) and processing time (s image^{-1}) of random forest classifiers developed using different combinations of features (number of features in brackets). The set of eleven features selected using sequential floating forward selection (SFFS) gave a slightly lower accuracy compared to the model including all 28 features (0.888 vs. 0.905) but required less than half of the time for image processing (11 vs. 24 s). It was therefore chosen as the best feature set.

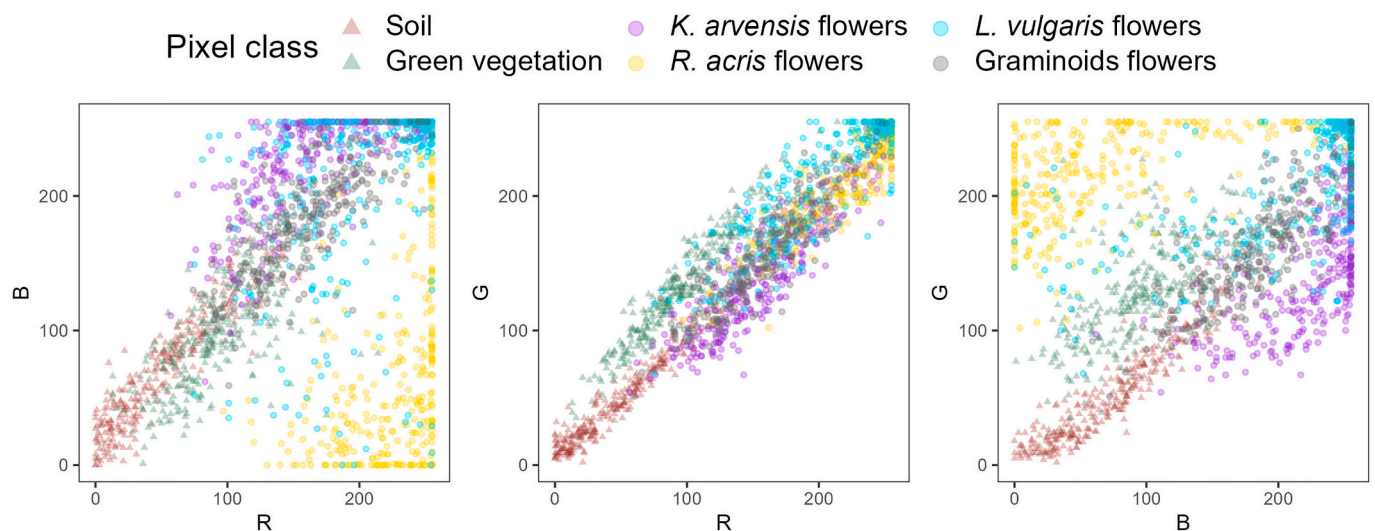|	RGB (3)	RGB + vegetation indices (7)	RGB + texture metrics (24)	All features (28)	Selected using SFFS (11)
Mean F1 score	0.791	0.800	0.883	0.905	0.888
Processing time (s image^{-1})	4	4	23	24	11

Fig. 4. Spectral separability of the labelled pixels in the RGB space. Based on two digital numbers (R and B, R and G, B and G), the overlaps of the six classes are presented. R is the red band digital number, G is the green band digital number, B is the blue band digital number. Values were extracted from 300 pixels per class without downscaling. (For interpretation of the references to colour in this figure legend, the reader is referred to the web version of this article.)

metrics increased this accuracy up to 0.905. Sequential floating forward selection led to the identification of eleven features out of a total of 28 as the most informative (Phase 3). This reduction in feature number reduced the processing time from 24 s to 11 s per image, without remarkable changes in accuracy (mean F1 scores of the six classes were 0.888 vs. 0.905). The eleven selected features were red, green and blue digital number, GLI, NGRDI, RGBVI, VARI, Second Moment computed on the red band, as well as Contrast, Second Moment, and Entropy computed on the blue band.

The confusion matrix of the classification performed with the best RF classifiers gave insights into the quality of our proposed workflow (Table 3). All six classes had precisions above 0.78, indicating a low proportion of wrong pixels in the classified classes. "Graminoids flowers" were difficult to distinguish from "Soil", and "*K. arvensis* flowers" were difficult to distinguish from "Graminoids flowers" (see also Fig. 4). The recall of "Graminoids flower" and "*K. arvensis* flowers" classes was therefore the lowest (0.79 and 0.76, respectively). 3.4% of the pixels labelled as "Soil" were classified as "Graminoids flower". Even though this value appears to be low, it will result in a substantial overestimation of graminoids flowers, since a large number of the pixels in the images were classified as soil pixels at the start of the season. At the end of the season, conversely, "Graminoids flower" cover could be underestimated, since 9% of the pixels labelled as "Graminoids flower" were misclassified as soil.

In Phase 4, we extracted time series of flower cover for all the plots, e. g., a plot where *L. vulgare, R. acris, P. pratensis* and *G. pratense* were sown (Fig. 5). In this example plot, we could observe that L. *vulgare* and *R. acris* were the dominant flowering species (left panel) and that classified images showed a good match with RGB images. Moreover, *L. vulgare* flowered later than *R. acris*, reaching its peak five days before mowing date (May 25th). Graminoids flower cover showed positive values around 1.5% in the fitted time series, even though the flowers of *P. pratensis,* the only graminoid species sown, were not present in the RGB images (Fig. 5, right panel). This indicated that in this case the graminoids flower cover was overestimated.

We applied the developed workflow and extracted time series for all plots. Here we show the result for nine exemplary plots, dominated by L. *vulgare* (Fig. 6 A, B, and C), by graminoids (Fig. 6 D, E, F), or by *R. acris* and *K. arvensis* (Fig. 6 G, H, I). *L. vulgare* and graminoid-dominated plots showed the highest maximum flower covers, whereas *K. arvensis* and *R. acris* showed lower flower covers. The peak day of flowering of each species differed among plots: graminoids started flowering more slowly compared to the other species, before developing faster than other species after mid-May.

We further investigated the seasonal average of FCTS of species that were not sown in the plots (Figs. 7 and S3). Our findings showed that in four out of 89 plots, the flower cover of these unsown species exceeded 10%, primarily due to the presence of pixels misclassified as graminoids flowers. However, the average flower cover for unsown species across all 89 plots was relatively low with 2%. Furthermore, when the graminoids

class was excluded, the error was almost negligible, being just 0.6%. In the experimental setting of the TBE, flowering started in some cases before the observation period had begun (i.e., before the spring weeding took place). These occurrences were identified (see Section 2.3.4) and the onset of flowering was not extracted for these cases. Similarly, in some cases flowering did not reach its peak before the end of the observation period (i.e., grassland mowing on May 30th) and consequently the end of flowering was not extracted. Peak day was extracted from 33 time-series, onset day from 16 time-series, and end of flowering from eight time-series.

4. Discussion

We propose a workflow to efficiently track flowering phenology of individual plant species or groups of plant species in grasslands using time-lapse cameras, which are widely applied in ecological studies. Therefore, sensor availability and installation are no limiting factors for ecologists who can use the proposed workflow for various applications (Brown et al., 2016; see subsection 4.1). Specifically, we propose an automated selection of vegetation indices and texture metric features to enhance the accuracy and processing time of a random forest classifier. The workflow can easily be replicated following FAIR principles and can be applied to new case studies. The codes have been developed in the free software R (R Core Team, 2023, GNU General Public License), and a tutorial is provided (https://github.com/andreattad/Flower_covers_phe nocams).

4.1. Possible applications of flower cover extraction workflow

Multiple opportunities to apply the developed procedure in basic and applied ecological research exist. Fields of application span from climate change studies over ecosystem functioning to plant community ecology and biodiversity change research, with both experimental as well as observational settings.

Application is possible in biodiversity research such as biodiversity-ecosystem functioning experiments. The experimental site where the current study was conducted was designed to investigate species interactions and to mechanistically understand biodiversity-ecosystem functioning relationships (Ebeling et al., 2014). However, manual assessments of flowering phenology are very labour-intensive and cannot be carried out regularly. In contrast, time-lapse cameras with the proposed processing workflow can be applied to investigate if and how individual plant species change their flowering phenology. The proposed workflow opens new possibilities in the study of flowering phenology of individual species in response to a wide range of biotic and abiotic drivers, for example to assess the effects of increased carbon dioxide concentrations and higher temperatures, heat and drought stress on reproductive phenology (Collins et al., 2021; Dorji et al., 2020; Fernández-Pascual et al., 2019). Pollinator ecology is another research field that could benefit strongly from the availability of the proposed

Table 3

Confusion matrix of the final random forest classifier on the validation dataset used in Phase 3. The mean F1 Score of the six classes was 0.888, the mean recall was 0.888, and the mean precision was 0.888.

|		Reference pixel class							
		K. arvensis flowers	*L. vulgare* flowers	Graminoids flowers	*R. acris* flowers	Green vegetation	Soil	Total	Precision
Predicted pixel class	*K. arvensis* flowers	117	21	12	0	0	0	150	0.78
	L. vulgare flowers	6	363	21	1	1	0	392	0.93
	Graminoids flowers	28	11	334	0	12	14	399	0.84
	R. acris flowers	0	2	1	163	2	0	168	0.97
	Green vegetation	2	4	16	5	1157	7	1191	0.97
	Soil	0	1	38	0	34	394	467	0.84
	Total	153	402	422	169	1206	415	2767	
	Recall	0.76	0.90	0.79	0.96	0.96	0.95		
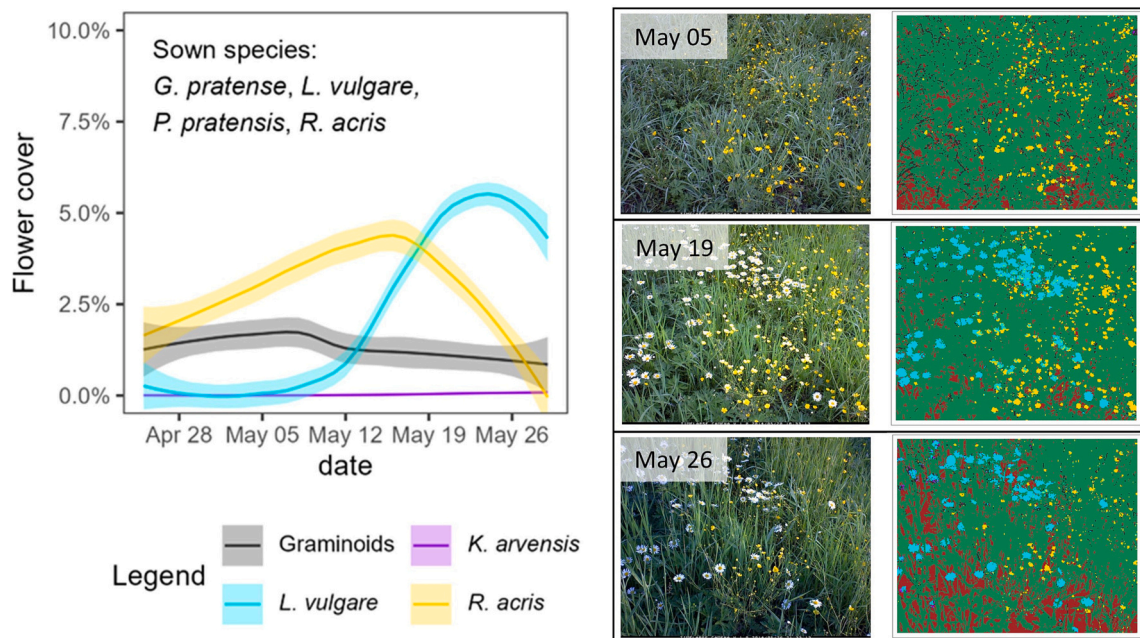
Fig. 5. Left panel: Time series of flower cover extracted from images from an example plot where L. *vulgare, R. acris, P. pratensis* and *G. pratense* were growing. Time series were fitted using Local Polynomial Regression, and 0.95 confidence intervals are displayed. Right panel: RGB and classified images acquired on the same example plot on May 5th, May 19th and May 26th, 2014 are presented. Green and brown pixels represent the "Green vegetation" and "Soil" classes, respectively. (For interpretation of the references to colour in this figure legend, the reader is referred to the web version of this article.)

workflow, since plant-pollinator interactions are strongly time-sensitive (Byers, 2017; Dicks et al., 2021; Freimuth et al., 2022; Vasiliev and Greenwood, 2021; Vázquez et al., 2023).

Grasslands do not only provide animal feed, pollen and nectar, but they also provide cultural services, which are relevant for tourism, recreation, mental and physical human health, aesthetically appreciated, inspire art as well as design, and are considered a typical feature of cultural landscape in many world regions (Richter et al., 2021). Animal feed production could also benefit from the proposed workflow as grassland management requires accurate data on plant phenology in near real time as a predictor of forage quality. Flowering phenology is crucial also in plant breeding (Arzani et al., 2004; Jung and Müller, 2009).

4.2. Challenges in flower detection and limitations of the proposed workflow

Classifier development for PC image classification is challenging since light conditions vary substantially during the recording times, and some classes are likely to be strongly underrepresented, for example flowers of rare species. Here we propose an efficient labelling phase with analyses of image patches from many images, allowing the representation of also rare species in the labelled sample. We aggregate all graminoids flowers in a single pixel class, since taxonomically and phenotypically close plant species are often too similar to be distinguished reliably, especially in the case of sedge, rush and grass species. We expect that a similar aggregation of different species in one class might also be necessary in future applications in biodiversity-rich grasslands that include many closely-related species.

Not all flower species can be spectrally easily distinguished. For example, young *K. arvensis* head colours are very similar to green-greyish graminoids flowers. On the other hand, *D. glomerata* mature flowerheads may be red- to purple-tinged, very similar to *K. arvensis* flowers. Their classes were described by very similar feature characteristics, which can result in lower classification accuracy (cf. Table 3 and Fig. 4). Following these observations, we expect that with increasing complexity of the study system in terms of plant diversity, maintaining

the accuracy of the method will become more challenging, even though texture metrics considerably increased the separability of different flower structures in our study. But in such very rich grasslands, plant biodiversity is then often described with plant functional types, e.g., grasses, forbs and legumes, instead of plant species, and their flower separation using time-lapse images could follow the presented, albeit further developed approach. However, low-diversity grasslands are common both in nature and as a research infrastructure, where sown swards are studied in field or pot experiments, typically to investigate the role of biodiversity and environmental factors on ecosystem functioning (Jentsch et al., 2009; Roscher et al., 2005; Wolf et al., 2017).

Phenological metrics that are automatically extracted through the proposed method can be related to metrics identified with traditional field methods. Field observation of plant flowering phenology is usually repeated at daily to weekly intervals and thus describes plant development at various degrees of detail. Simple metrics such as the first and last day with flowering individuals in the plots, or the day with the highest number of flowering individuals per plot are frequently used in ecological studies dealing with the effect of global change on plant phenology (Cleland et al., 2006; Dorji et al., 2020; Wolf et al., 2017). They are conceptually similar to the metrics proposed here. However, very detailed scales for the description of plant development such as the BBCH scale (Meier et al., 2009) with >50 distinct plant development stages, separately determined for groups of species or single species, can be more difficult to relate to the metrics proposed here. The BBCH scale is not based on flower count or flower cover, but on the description of developmental characteristics, which currently cannot be derived from images through the proposed automated workflow. Thus, future research should attempt to implement pathways to measure more traditional plant phenology metrics that are currently not assessed via automated remote sensing techniques.

When investigating plots with highest average seasonal flower cover of unsown species (i.e., the nine plots shown in Fig. S3), we found these had higher soil cover compared to the overall seasonal average (25% vs. 10%). As already reported in the confusion matrix in Table 3, some soil pixels were misclassified as flowers, and the number of pixels in the flower classes were therefore overestimated. The image dataset we
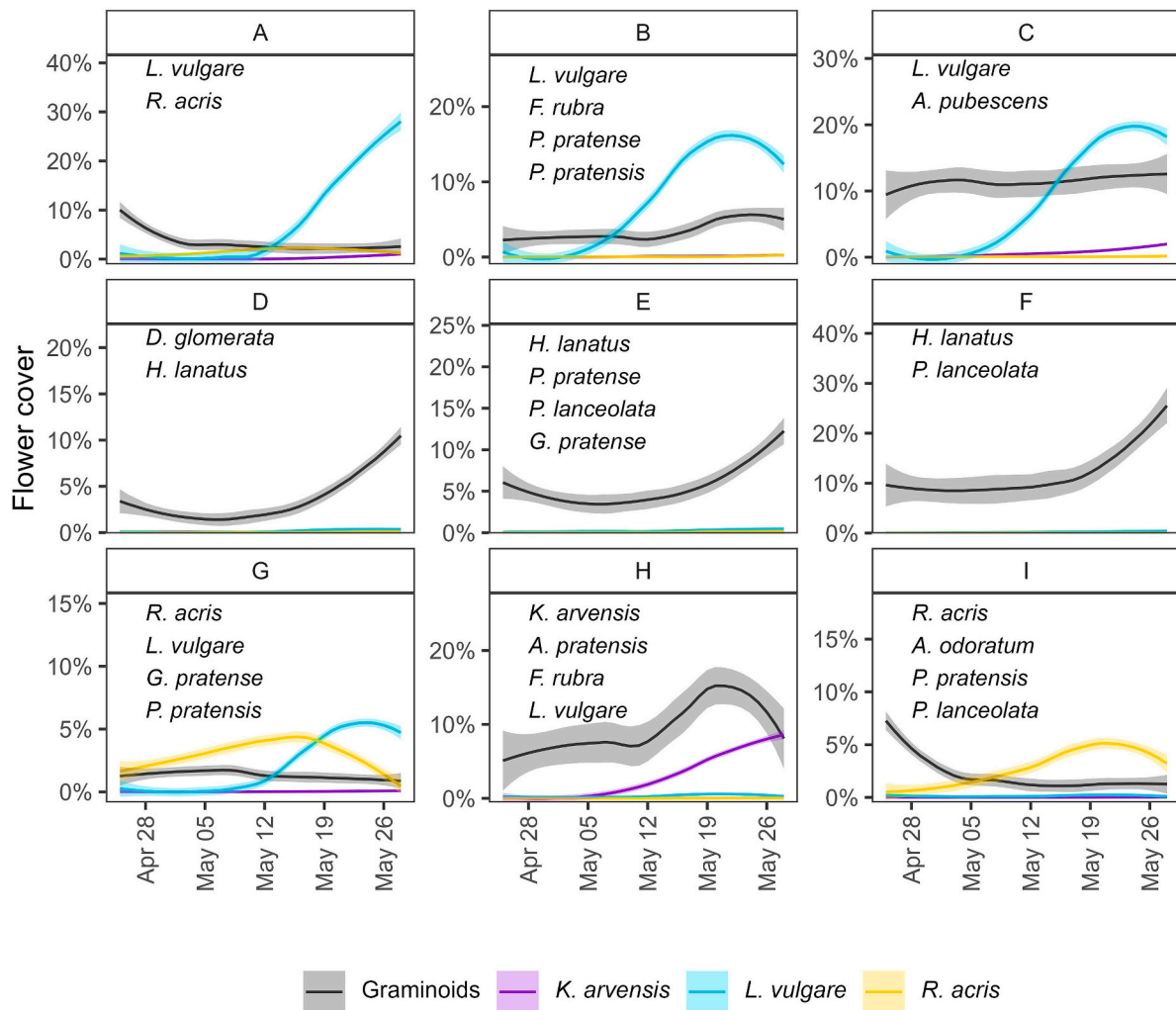
Fig. 6. Time series of flower cover extracted from images acquired in nine experimental plots in spring 2014 (before first mowing). Time series are fitted using Local Polynomial Regression. Confidence intervals (0.95) and sown species names are given in each panel.

analysed in the current study captured an area of 3.5 m², which resulted in a pixel size (ground sampling distance) lower than ¼ of the flower size. This ¼ is the suggested minimum ratio between pixel and object dimension for accurate classification (Hengl, 2006). PC images are usually acquired capturing larger areas to describe vegetation patches at landscape scale (Wingate et al., 2015). Thus, for the study design of future studies on the monitoring of reproductive phenology, an optimised field of view should be chosen, considering flowers size and PC resolution. For example, a camera pointing at an angle of 60° from horizontal, the field of view of 49.5° and an optical resolution of 1280 × 1040 pixels should be installed at a maximum height of 1.5 m to classify flowers of size 5 mm and at a maximum height of 3 m to classify flowers of size 10 mm. To ensure the observation of the onset of flowering, it is crucial to establish an experimental setting for phenological observation that spans the entire growing season, whenever possible. However, in this study, this was not always possible as the observation period began after spring weeding of the experiment, preventing the observation of the onset of flowering in some cases.

4.3. Paths for further investigation

New technologies and methodologies are opening new possibilities in grassland phenological studies. Active learning is a promising methodology for balanced sample collection with reduced labelling effort, and was already proposed, for example, for the reduction of sampling

effort in forestry inventories (Malek et al., 2019; Persello et al., 2014). The use of active learning could facilitate the labelling phase in biodiversity rich grasslands.

Computer vision (CV) techniques are increasingly being used in ecological studies and have recently been applied to classify grassland images acquired from drones as well as PC images of arctic vegetation (Gallmann et al., 2022; Mann et al., 2022; Wäldchen and Mäder, 2017). However, to our knowledge, no study about grassland flowering phenology using CV techniques to classify PC imagery has been carried out so far. In this study, we applied a pixel approach rather than CV techniques, and quantified flower cover rather than flower count as abundance metric, because CV techniques require a much larger labelling effort and computational capacity, and might not be suited for graminoids flowers and occluded or overlapping flowers. Furthermore, we favoured pixel classification over CV techniques, because the former requires highly specialised knowledge, which is not always available to both biologists and ecologists (Wäldchen and Mäder, 2018). Flower cover is an informative metric also because it can better capture the effect of flowering on greenness, which is widely used to describe vegetation status (Shen et al., 2010). Nevertheless, the increasing availability of pre-trained models that can be fine-tuned, and the recent higher accessibility of these techniques suggest that, in some cases, they could be applied to estimate species flower cover in grassland mixtures (Kirillov et al., 2023; Mann et al., 2022; Wäldchen and Mäder, 2018). Thus, the availability of the proposed workflow opens up new
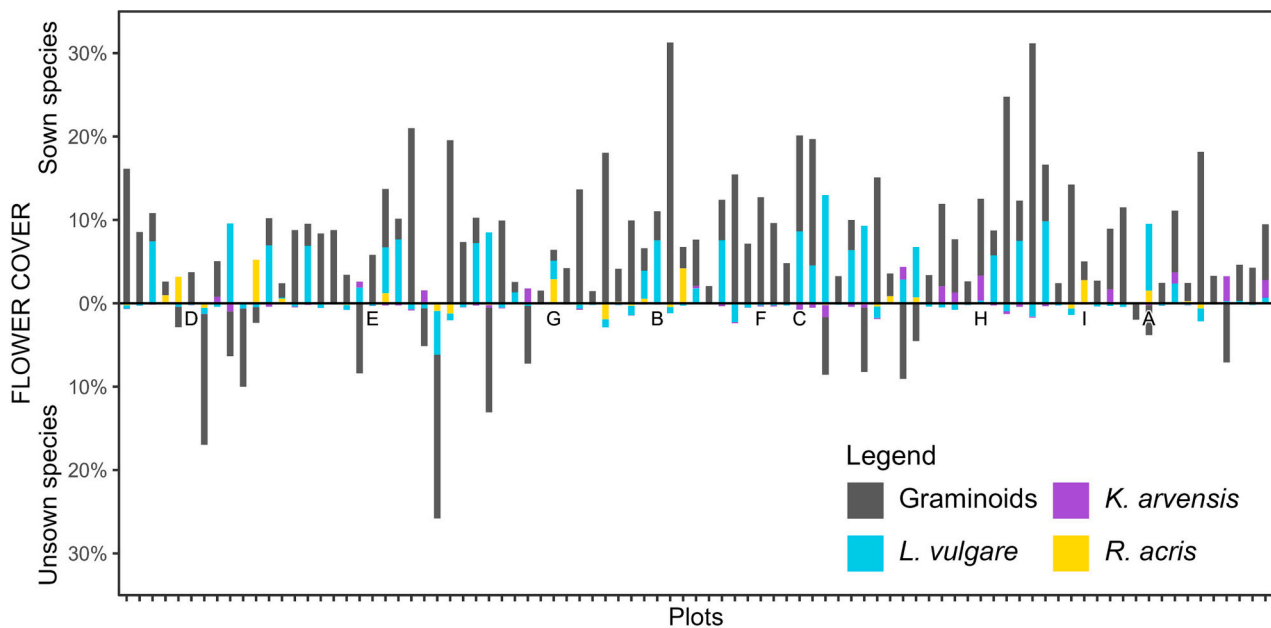
Fig. 7. Seasonal average of flower cover per class, according to the experimental design with different species mixtures. Upper panel: Sown species are displayed. Lower panel: Unsown species are displayed. The plot IDs shown in Fig. 6 (A to I) are reported below the upper panel, indicating zero flower cover. The mean flower cover of unsown species in each plot was 2% with, and 0.6% without the graminoids class.

possibilities in many ecological research fields, including the investigation of species richness effects on individual species flowering phenology.

Author contributions

All authors contributed to the intellectual development and conception of this manuscript; Davide Andreatta performed the analyses and led the writing of the manuscript. All authors contributed critically to the drafts and gave final approval for publication.

Declaration of Competing Interest

The authors declare that they have no known competing financial interests or personal relationships that could have appeared to influence the work reported in this paper.

Data availability

All the PhenoCam images, regions of interest, labelled pixels displayed on RGB image details and labelled pixel coordinates have been made available via the ETH Zurich repository (https://doi.org/10.3929/ethz-b-000634004). We provide a tutorial to guide the reader in the application of the proposed methodology. The tutorial is available at the link (https://github.com/andreattad/Flower_covers_phenocams). Three figures were provided in the supplementary materials. Fig. S1 shows accuracy of classifiers based on features calculated at different downscaling factors and window sizes. Fig. S2, Table S1 and Table S2 showing image availability before and after image selection are available in the Supplementary information. Fig. S3 shows the time series of flower cover of the nine experimental plots with the highest seasonal average of flower cover of unsown species.

Acknowledgements

Special thanks to Thomas Lanners who acquired all the images in 2014. We acknowledge all the coordinators, the gardening team from the Jena Experiment, and many field assistants for maintaining the field.

Appendix A. Supplementary data

Supplementary data to this article can be found online at https://doi.org/10.1016/j.rse.2023.113835.

References

Andrew, M.E., Ustin, S.L., 2008. The role of environmental context in mapping invasive plants with hyperspectral image data. Remote Sens. Environ. 112 (12), 4301–4317. https://doi.org/10.1016/J.RSE.2008.07.016.
Arzani, H., Zohdi, M., Fish, E., Amiri, G.H.Z., Nikkhah, A., Wester, D., 2004. Phenological effects on forage quality of five grass species. J. Range Manag. 57 (6), 624–629. https://doi.org/10.2111/1551-5028(2004)057.
Bendig, J., Yu, K., Aasen, H., Bolten, A., Bennertz, S., Broscheit, J., Gnyp, M.L., Bareth, G., 2015. Combining UAV-based plant height from crop surface models, visible, and near infrared vegetation indices for biomass monitoring in barley. Int. J. Appl. Earth Obs. Geoinf. 39, 79–87. https://doi.org/10.1016/J.JAG.2015.02.012.
Brown, T.B., Hultine, K.R., Steltzer, H., Denny, E.G., Denslow, M.W., Granados, J., Henderson, S., Moore, D., Nagai, S., Sanclements, M., Sánchez-Azofeifa, A., Sonnentag, O., Tazik, D., Richardson, A.D., 2016. Using phenocams to monitor our changing earth: toward a global phenocam network. Front. Ecol. Environ. 14 (2), 84–93. https://doi.org/10.1002/FEE.1222.
Bruzzone, L., Roli, F., Serpico, S.B., 1995. An extension of the Jeffreys-Matusita distance to multiclass cases for feature selection. IEEE Trans. Geosci. Remote Sens. 33 (6), 1318–1321. https://doi.org/10.1109/36.477187.
Byers, D.L., 2017. Studying plant–pollinator interactions in a changing climate: a review of approaches. Appl. Plant Sci. 5 (6), 1700012. https://doi.org/10.3732/apps.1700012.
Chen, B., Jin, Y., Brown, P., 2019. An enhanced bloom index for quantifying floral phenology using multi-scale remote sensing observations. ISPRS J. Photogramm. Remote Sens. 156, 108–120. https://doi.org/10.1016/j.isprsjprs.2019.08.006.
Cleland, E.E., Chiariello, N.R., Loarie, S.R., Mooney, H.A., Field, C.B., 2006. Diverse responses of phenology to global changes in a grassland ecosystem. Proc. Natl. Acad. Sci. 103 (37), 13740–13744. https://doi.org/10.1073/pnas.0600815103.
Collins, C.G., Elmendorf, S.C., Hollister, R.D., Henry, G.H.R., Clark, K., Bjorkman, A.D., Myers-Smith, I.H., Prevéy, J.S., Ashton, I.W., Assmann, J.J., Alatalo, J.M., Carbognani, M., Chisholm, C., Cooper, E.J., Forrester, C., Jónsdóttir, I.S., Klanderud, K., Kopp, C.W., Livensperger, C., Suding, K.N., 2021. Experimental warming differentially affects vegetative and reproductive phenology of tundra plants. Nat. Commun. 12 (1), 1–12. https://doi.org/10.1038/s41467-021-23841-2.

Congalton, R.G., Green, K., 2009. Assessing the Accuracy of Remotely Sensed Data: Principles and Practices, 2nd ed. CRC Press/Taylor & Francis.

Dalponte, M., Ørka, H.O., 2021. varSel: Sequential Forward Floating Selection using Jeffries-Matusita Distance. R package version 0.2. https://CRAN.R-project.org/package=varSel.

d'Andrimont, R., Taymans, M., Lemoine, G., Ceglar, A., Yordanov, M., van der Velde, M., 2020. Detecting flowering phenology in oil seed rape parcels with Sentinel-1 and -2 time series. Remote Sens. Environ. 239, 111660. https://doi.org/10.1016/J.RSE.2020.111660.

Dicks, L.v., Breeze, T.D., Ngo, H.T., Senapathi, D., An, J., Aizen, M.A., Basu, P., Buchori, D., Galetto, L., Garibaldi, L.A., Gemmill-Herren, B., Howlett, B.G., Imperatriz-Fonseca, V.L., Johnson, S.D., Kovács-Hostyánszki, A., Kwon, Y.J., Lattorff, H.M.G., Lungharwo, T., Seymour, C.L., Potts, S.G., 2021. A global-scale expert assessment of drivers and risks associated with pollinator decline. Nat. Ecol. Evol. 5 (10), 1453–1461. https://doi.org/10.1038/s41559-021-01534-9.

Dixon, D.J., Callow, J.N., Duncan, J.M.A., Setterfield, S.A., Pauli, N., 2021. Satellite prediction of forest flowering phenology. Remote Sens. Environ. 255, 112197. https://doi.org/10.1016/J.RSE.2020.112197.

D'Odorico, P., Gonsamo, A., Gough, C.M., Bohrer, G., Morison, J., Wilkinson, M., Hanson, P.J., Gianelle, D., Fuentes, J.D., Buchmann, N., 2015. The match and mismatch between photosynthesis and land surface phenology of deciduous forests. Agric. For. Meteorol. 214–215, 25–38. https://doi.org/10.1016/J.AGRFORMET.2015.07.005.

Dorji, T., Hopping, K.A., Meng, F., Wang, S., Jiang, L., Klein, J.A., 2020. Impacts of climate change on flowering phenology and production in alpine plants: the importance of end of flowering. Agric. Ecosyst. Environ. 291, 106795. https://doi.org/10.1016/J.AGEE.2019.106795.

Ebeling, A., Pompe, S., Baade, J., Eisenhauer, N., Hillebrand, H., Proulx, R., Roscher, C., Schmid, B., Wirth, C., Weisser, W.W., 2014. A trait-based experimental approach to understand the mechanisms underlying biodiversity-ecosystem functioning relationships. Basic Appl. Ecol. 15 (3), 229–240. https://doi.org/10.1016/j.baae.2014.02.003.

Estiarte, M., Peñuelas, J., 2015. Alteration of the phenology of leaf senescence and fall in winter deciduous species by climate change: effects on nutrient proficiency. Glob. Chang. Biol. 21, 1005–1017.

Fernández-Pascual, E., Mattana, E., Pritchard, H.W., 2019. Seeds of future past: climate change and the thermal memory of plant reproductive traits. Biol. Rev. 94 (2), 439–456. https://doi.org/10.1111/BRV.12461.

Filippa, G., Cremonese, E., Migliavacca, M., Richardson, A., Galvagno, M., Forkel, M., 2016. Phenopix: Pixel Based Phenology. September.

Freimuth, J., Bossdorf, O., Scheepens, J.F., Willems, F.M., 2022. Climate warming changes synchrony of plants and pollinators. Proc. R. Soc. B 289 (1971), 20212142. https://doi.org/10.1098/RSPB.2021.2142.

Gallmann, J., Schüpbach, B., Jacot, K., Albrecht, M., Winizki, J., Kirchgessner, N., Aasen, H., 2022. Flower mapping in grasslands with drones and deep learning. Front. Plant Sci. 12, 774965. https://doi.org/10.3389/fpls.2021.774965.

Gitelson, A.A., Kaufman, Y.J., Stark, R., Rundquist, D., 2002. Novel algorithms for remote estimation of vegetation fraction. Remote Sens. Environ. 80 (1), 76–87. https://doi.org/10.1016/S0034-4257(01)00289-9.

Gonzales, D., Hempel de Ibarra, N., Anderson, K., 2022. Remote sensing of floral resources for pollinators – new horizons from satellites to drones. Front. Ecol. Evol. 10 (414), 869751. https://doi.org/10.3389/FEVO.2022.869751.

Guru, D.S., Sharath, Y.H., Manjunath, S., 2010. Texture features and KNN in classification of flower images. IJCA 1, 21–29. Special Issue on RTIPPR.

Haralick, R.M., Dinstein, I., Shanmugam, K., 1973. Textural features for image classification. IEEE Trans. Syst. Man Cybern. SMC-3 (6), 610–621. https://doi.org/10.1109/TSMC.1973.4309314.

Hengl, T., 2006. Finding the right pixel size. Comput. Geosci. 32 (9), 1283–1298. https://doi.org/10.1016/J.CAGEO.2005.11.008.

Hijmans, R.J., 2022. raster: Geographic Data Analysis and Modeling. https://cran.r-project.org/package=raster.

Ho, T.K., 1995. Random decision forests. In: Proceedings of the International Conference on Document Analysis and Recognition, ICDAR, 1, pp. 278–282. https://doi.org/10.1109/ICDAR.1995.598994.

Hyndman, R.J., Khandakar, Y., 2008. Automatic time series forecasting: the forecast package for R. J. Stat. Softw. 27 (3) https://doi.org/10.18637/jss.v027.i03.

Inouye, D.W., 2020. Effects of climate change on alpine plants and their pollinators. Ann. N. Y. Acad. Sci. 1469 (1), 26–37. https://doi.org/10.1111/NYAS.14104.

Jentsch, A., Kreyling, J., Boettcher-Treschkow, J., Beierkuhnlein, C., 2009. Beyond gradual warming: extreme weather events alter flower phenology of European grassland and heath species. Glob. Chang. Biol. 15 (4), 837–849. https://doi.org/10.1111/j.1365-2486.2008.01690.x.

Jung, C., Müller, A.E., 2009. Flowering time control and applications in plant breeding. Trends Plant Sci. 14 (10), 563–573. https://doi.org/10.1016/J.TPLANTS.2009.07.005.

Kirillov, A., Mintun, E., Ravi, N., Mao, H., Rolland, C., Gustafson, L., Xiao, T., Whitehead, S., Berg, A.C., Lo, W.-Y., Dollár, P., Girshick, R., 2023. Segment Anything, ArXiv. http://arxiv.org/abs/2304.02643.

Landmann, T., Piiroinen, R., Makori, D.M., Abdel-Rahman, E.M., Makau, S., Pellikka, P., Raina, S.K., 2015. Application of hyperspectral remote sensing for flower mapping in African savannas. Remote Sens. Environ. 166, 50–60. https://doi.org/10.1016/J.RSE.2015.06.006.

Liaw, A., Wiener, M., 2002. Classification and regression by random forest. R News 2 (3), 1822.

Liu, Y., Wang, J., Dong, J., Wang, S., Ye, H., 2020. Variations of vegetation phenology extracted from remote sensing data over the Tibetan plateau hinterland during 2000–2014. J. Meteorol. Res. 34 (4), 786–797. https://doi.org/10.1007/s13351-020-9211-x.

Louhaichi, M., Borman, M.M., Johnson, D.E., 2001. Spatially Located Platform and Aerial Photography for Documentation of Grazing Impacts on Wheat. Geocarto International 16 (1), 65–70. https://doi.org/10.1080/10106040108542184.

Lussem, U., Bolten, A., Gnyp, M.L., Jasper, J., Bareth, G., 2018. Evaluation of RGB-Based Vegetation Indices from UAV Imagery to Estimate Forage Yield in Grassland. https://doi.org/10.5194/isprs-archives-XLII-3-1215-2018.

Malek, S., Miglietta, F., Gobakken, T., Næsset, E., Gianelle, D., Dalponte, M., 2019. Optimizing field data collection for individual tree attribute predictions using active learning methods. Remote Sens. 11 (8), 949. https://doi.org/10.3390/rs11080949.

Mann, H.M.R., Iosifidis, A., Jepsen, J.U., Welker, J.M., Loonen, M.J.J.E., Høye, T.T., 2022. Automatic flower detection and phenology monitoring using time-lapse cameras and deep learning. Remote Sens. Ecol. Conserv. 8 (6), 765–777. https://doi.org/10.1002/rse2.275.

Meier, U., Bleiholder, H., Buhr, L., Feller, C., Hack, H., Heß, M., Lancashire, P., Schnock, U., Stauß, R., van den Boom, T., Weber, E., Zwerger, P., 2009. The BBCH system to coding the phenological growth stages of plants-history and publications. J. Kult. 61 (2).

Menzel, A., Sparks, T.H., Estrella, N., Koch, E., Aasa, A., Ahas, R., Alm-Kübler, K., Bissolli, P., Braslavská, O., Briede, A., Chmielewski, F.M., Crepinsek, Z., Curnel, Y., Dahl, Å., Defila, C., Donnelly, A., Filella, Y., Jatczak, K., Måge, F., Zust, A., 2006. European phenological response to climate change matches the warming pattern. Glob. Chang. Biol. 12 (10), 1969–1976. https://doi.org/10.1111/J.1365-2486.2006.01193.X.

Persello, C., Boularias, A., Dalponte, M., Gobakken, T., Naesset, E., Scholkopf, B., 2014. Cost-sensitive active learning for remote sensing data classification: optimizing field surveys for remote sensing data classification. IEEE Trans. Geosci. Remote Sens. 52 (10), 6652–6664. https://doi.org/10.1109/TGRS.2014.2300189.

Piao, S., Ciais, P., Friedlingstein, P., Peylin, P., Reichstein, M., Luyssaert, S., Margolis, H., Fang, J., Barr, A., Chen, A., Grelle, A., Hollinger, D.Y., Laurila, T., Lindroth, A., Richardson, A.D., Vesala, T., 2008. Net carbon dioxide losses of northern ecosystems in response to autumn warming. Nature 451 (7174), 49–52. https://doi.org/10.1038/nature06444.

Pudil, P., Novovičová, J., Kittler, J., 1994. Floating search methods in feature selection. Pattern Recogn. Lett. 15 (11), 1119–1125. https://doi.org/10.1016/0167-8655(94)90127-9.

R Core Team, 2023. *R: A Language and Environment for Statistical Computing*. R Foundation for Statistical Computing. https://www.R-project.org/.

Richards, J.A., Jia, Xiuping, 2006. Remote Sensing Digital Image Analysis : An Introduction. Springer.

Richardson, A.D., Black, T.A., Ciais, P., Delbart, N., Friedl, M.A., Gobron, N., Hollinger, D.Y., Kutsch, W.L., Longdoz, B., Luyssaert, S., Migliavacca, M., Montagnani, L., Munger, J.W., Moors, E., Piao, S., Rebmann, C., Reichstein, M., Saigusa, N., Tomelleri, E., Varlagin, A., 2010. Influence of spring and autumn phenological transitions on forest ecosystem productivity. Philos. Trans. R. Soc. B 365 (1555), 3227–3246. https://doi.org/10.1098/RSTB.2010.0102.

Richardson, A.D., Anderson, R.S., Arain, M.A., Barr, A.G., Bohrer, G., Chen, G., Chen, J. M., Ciais, P., Davis, K.J., Desai, A.R., Dietze, M.C., Dragoni, D., Garrity, S.R., Gough, C.M., Grant, R., Hollinger, D.Y., Margolis, H.A., McCaughey, H., Migliavacca, M., Xue, Y., 2012. Terrestrial biosphere models need better representation of vegetation phenology: results from the North American Carbon Program Site Synthesis. Glob. Chang. Biol. 18 (2), 566–584. https://doi.org/10.1111/j.1365-2486.2011.02562.x.

Richter, F., Jan, P., el Benni, N., Lüscher, A., Buchmann, N., Klaus, V.H., 2021. A guide to assess and value ecosystem services of grasslands. Ecosyst. Serv. 52, 101376. https://doi.org/10.1016/J.ECOSER.2021.101376.

Roscher, C., Temperton, V.M., Scherer-Lorenzen, M., Schmitz, M., Schumacher, J., Schmid, B., Buchmann, N., Weisser, W.W., Schulze, E.D., 2005. Overyielding in experimental grassland communities - irrespective of species pool or spatial scale. Ecol. Lett. 8 (4), 419–429. https://doi.org/10.1111/J.1461-0248.2005.00736.X.

Schwartz, M., 2013. *Phenology: An Integrative Environmental Science* (M. D. Schwartz, Ed.). Springer, Netherlands. https://doi.org/10.1007/978-94-007-6925-0.

Shen, M., Chen, J., Zhu, X., Tang, Y., Chen, X., 2010. Do flowers affect biomass estimate accuracy from NDVI and EVI? Int. J. Remote Sens. 31 (8), 2139–2149. https://doi.org/10.1080/01431160903578812.

Shen, M., Tang, Y., Chen, J., Zhu, X., Zheng, Y., 2011. Influences of temperature and precipitation before the growing season on spring phenology in grasslands of the central and eastern Qinghai-Tibetan plateau. Agric. For. Meteorol. 151 (12), 1711–1722. https://doi.org/10.1016/J.AGRFORMET.2011.07.003.

Szigeti, V., Kőrösi, Ádam, Haros, A., Nagy, J., Kis, J., 2016. Measuring floral resource availability for insect pollinators in temperate grasslands - a review. Ecol. Entomol. 41 (3), 231–240. https://doi.org/10.1111/een.12298.

Thackeray, S.J., Henrys, P.A., Hemming, D., Bell, J.R., Botham, M.S., Burthe, S., Helaouet, P., Johns, D.G., Jones, I.D., Leech, D.I., Mackay, E.B., Massimino, D., Atkinson, S., Bacon, P.J., Brereton, T.M., Carvalho, L., Clutton-Brock, T.H., Duck, C., Edwards, M., Wanless, S., 2016. Phenological sensitivity to climate across taxa and trophic levels. Nature 535 (7611), 241–245. https://doi.org/10.1038/nature18608.

Tucker, C.J., 1979. Red and photographic infrared linear combinations for monitoring vegetation. Remote Sens. Environ. 8 (2), 127–150. https://doi.org/10.1016/0034-4257(79)90013-0.

Vasiliev, D., Greenwood, S., 2021. The role of climate change in pollinator decline across the Northern Hemisphere is underestimated. Sci. Total Environ. 775, 145788. https://doi.org/10.1016/j.scitotenv.2021.145788.

Vázquez, D.P., Vitale, N., Dorado, J., Amico, G., Stevani, E.L., Leal, R., 2023. Phenological mismatches and the demography of solitary bees. Proc. R. Soc. B 290 (1990). https://doi.org/10.1098/RSPB.2022.1847, 20221847.

Wäldchen, J., Mäder, P., 2017. Plant species identification using computer vision techniques: a systematic literature review. Arch. Comput. Methods Eng. 25 (2), 507–543. https://doi.org/10.1007/S11831-016-9206-Z.

Wäldchen, J., Mäder, P., 2018. Machine learning for image based species identification. Methods Ecol. Evol. 9 (11), 2216–2225. https://doi.org/10.1111/2041-210X.13075.

Wingate, L., Cremonese, E., Migliavacca, M., Brown, T., D'Odorico, P., Peichl, M., Gielen, B., Lukas, H., 2015. PROTOCOL Phenocamera: automated phenology monitoring. ICOS, p. 17.

Wolf, A.A., Zavaleta, E.S., Selmants, P.C., 2017. Flowering phenology shifts in response to biodiversity loss. Proc. Natl. Acad. Sci. U. S. A. 114 (13), 3463–3468. https://doi.org/10.1073/pnas.1608357114.

Wouters, N., de Ketelaere, B., de Baerdemaeker, J., Saeys, W., 2013. Hyperspectral waveband selection for automatic detection of floral pear buds. Precis. Agric. 14 (1), 86–98. https://doi.org/10.1007/S11119-012-9279-0/TABLES/3.

Zhao, Y., 2021. The segmentation of plants on RGB images with index based color analysis. In: 2021 5th International Conference on Robotics and Automation Sciences, ICRAS 2021, pp. 221–225. https://doi.org/10.1109/ICRAS52289.2021.9476331.

Zvoleff, A., 2020. Package 'glcm.' Calculate Textures from Grey-Level Co-Occurence Matrices (GLCMs). *Available Online: Https://CRAN.R-Project.Org/Package=Glcm*.

Study IV

Diverging trends in plant phenology across European mountains in a warming world

Davide Andreatta, Loris Vescovo, Michele Dalponte, Luca Belelli Marchesini, Tommaso Jucker, Nina Buchmann, Michele Scotton, Damiano Gianelle

This study has not been submitted for publication yet.

Diverging trends in plant phenology across European mountains in a warming world

Authors

Davide Andreatta[1,2], Loris Vescovo[2], Michele Dalponte[2], Luca Belelli Marchesini[2], Tommaso Jucker[3], Nina Buchmann[4], Michele Scotton[1], Damiano Gianelle[2]

Affiliations

[1] Department of Agronomy, Food, Natural Resources, Animals and Environment, University of Padova, Legnaro, Padova, Italy

[2] Research and Innovation Centre, Fondazione Edmund Mach, San Michele all'Adige, Trento, Italy

[3] School of Biological Sciences, University of Bristol, Bristol, UK

[4] Institute of Agricultural Sciences, Department of Environmental Systems Science, ETH Zürich, Zürich, Switzerland

Highlights

- Temporal shifts in plant phenology vary depending on elevation
- Natural grasslands and broadleaved forests showed diverging phenological dynamics
- No evidence of more uniform spring phenology across elevations and geographic areas
- Temporal decoupling of Growing Season Length and Gross Primary Productivity

Keywords

Phenology; Europe; Grasslands; Broadleaved Forests; Growing season; Carbon cycling.

Abstract

Global warming is affecting both the phenology and productivity of plant ecosystems, with big implications for carbon cycling on land. However, we continue to lack a clear picture of how plant phenological trends are shifting in climatically heterogenous mountain landscapes, and how this is affecting ecosystem productivity. Using satellite data, our study reveals substantial differences in the phenological response among vegetation types and across elevations in the European mountains from 2001 to 2021. These divergent trends led to a more uniform spring phenology across elevations in natural grasslands, while broadleaved forests exhibited the

1

Diverging trends in plant phenology across European mountains in a warming world
Andreatta et al. (2024), *unpublished*

opposite trend. Despite global warming increasing both the growing season length and gross primary productivity, we only found a weak correlation between the two ($R^2 < 0.02$), indicating that phenology has not been the primary factor limiting productivity over the past two decades.

One-Sentence Summary

Satellite data uncovers surprising elevation-dependent patterns in plant phenology, and implications for carbon cycling.

Introduction

Global warming is increasing the length of the potential thermal growing season in temperature limited ecosystems, with big implications for vegetation phenology and carbon cycling[1]. However, while in some cases extending the growing season length will result in a higher net carbon uptake in temperate, boreal, and alpine ecosystems[2–5], there is also evidence to the contrary[6–8], underscoring the complexity of how phenological responses to climate change ultimately influence carbon cycling [9–11]. Identifying spatial and temporal phenological trends and better understanding climate-phenology feedbacks is urgent to forecast changes in the climate system.

The actual green season start advance lagged three times behind the advance of the potential thermal season start in the last two decades[1,12–14]. This discrepancy has been attributed to the lack of the necessary winter chilling requirement for leaf unfolding in a warmer climate[1] and to the photoperiod control on spring phenology[13,15]. The mismatch between the actual and the potential thermal autumn phenology were directly related to productivity-phenology feedbacks[16–20]. Recent findings suggested that the increased ecosystem productivity can potentially limit the current delaying trend in autumn leaf senescence because of the limited availability of "carbon sink" tissues, i.e., the impossibility to stock the additional products of photosynthesis in the last part of the season[19,20]. However, it was also observed that interannual trends do not always match decadal trends, because the acclimation of phenology has enabled plants to transcend premature carbon sink saturation over the course of several decades[21].

In mountainous regions, the combination of elevation and regional climate plays a crucial role in determining the length of the potential thermal growing season, and this interaction occurs across very small spatial scales. The complex topography, characterized by significant variations in elevation over short distances, results in a large spatial heterogeneity of plant phenology. Previous studies carried out in the Alps showed that the factors that regulate plant phenology vary in importance at different elevations. At high elevations correlations between

snow cover duration and the start of the growing season were more pronounced[22], at mid to low elevation the start of the growing season was more influenced by spring temperatures[23,24]. Since the various climatic variables do not vary uniformly between each other nor uniformly in space, it is reasonable to anticipate a phenological response that is dependent on elevation. However, the typical spatial resolution adopted in most recent phenological studies[9,25] cannot provide a clear understanding of processes happening along elevational gradients in areas with complex topography and of the different phenological responses of vegetation types in fragmented landscapes[26,27]. While field observations can offer valuable insights into phenological trends across different elevations[28], satellite observations at a relatively fine scale must be used to obtain consistent, long-term data on phenology and productivity over large regions. However, elevational patterns in phenology and the coupling between phenology and productivity across major mountain chains remain unclear, hindering our understanding of the future functioning of mountain vegetation in a warming world.

Here, we want to contribute to fill this knowledge gap by verifying: i) the entity and variability of the phenological trends across elevational gradients, mountain regions and vegetation types; ii) the uniformization of phenology along the elevational gradient[28]; iii) the concurrent increase of Growing Season Length (GSL) and Gross Primary Productivity (GPP). To test the aforementioned hypothesis we i) selected four of the biggest mountain regions in Europe: the Alps, the Carpathians, the Nordic Mountains, and the Pyrenees as study sites to explore patterns along elevation gradients; ii) removed the potential noise caused by mixed pixels by selecting areas with permanent land-cover in the last two; iii) compared two widely distributed vegetation types: natural grasslands and broadleaved forests; and iv) identified phenological and productivity trends using MODIS imagery at 500 m resolution.

Trends in phenometrics

Compared to previous studies we investigated phenological trends at finer spatial resolution (500 m) along elevational gradients in fragmented landscapes, minimizing the mixed-pixel challenge of moderate-resolution satellite imagery, better accounting for vegetation type change and investigating a more recent period (2001-2021) (Materials and methods are available as supplementary materials).The pixel dataset consisted of 142,128 pixels, whose frequency distribution in geographic regions, vegetation type and Mean Annual Temperature (MAT) is displayed in Fig. 2b. Our study revealed (Fig. 1) a bigger shift in Mid Greendown (MGDO) rather than in the Mid Greenup (MGUP). We observed a much smaller advance in MGUP in forests compared to previous findings[1] (0.06 d y^{-1} during 2001-2021 vs. 0.31 d y^{-1} during 1980-2016 in central Europe), but a larger delay in MGDO (0.19 d y^{-1} vs -0.03 d y^{-1}, Fig. S1). The average regional advance of MGUP showed different magnitude in grasslands

compared to forests, but not consistently across geographic areas: on the Alps MGUP advanced more in forests than in grasslands (0.11 d y^{-1} vs 0.07 d y^{-1}), whereas on the Carpathians and on the Pyrenees MGUP advanced more in grasslands than in forests (0.26 d y^{-1} vs 0.07 d y^{-1} and 0.14 d y^{-1} vs 0.09 d y^{-1}, respectively). Nordic Mountain forests showed no MGUP trend on average, but we detected clear spatial patterns. The northern-western region showed an intense delay of MGUP (up to >0.40 d y^{-1}), whereas the southern-eastern region showed an intense advance of MGUP (up to >0.30 d y^{-1}) (Fig. 1). Other hotspots of forest MGUP advance are the outer Alps, western Carpathians, and eastern Pyrenees. Grassland MGUP was notably advanced in the central-eastern Pyrenees whereas it was delayed in western Pyrenees. We observed the largest delays in MGDO on the Alps (grasslands 0.33 d y^{-1} and forests 0.24 d y^{-1}), on the Pyrenees (grasslands 0.32 d y^{-1} and forests 0.19 d y^{-1}), and on the Carpathian forests (0.24 d y^{-1}). We observed weaker MGDO delays in the Nordic Mountains forests (0.07 d y^{-1}). In the Carpathian grasslands we observed an advance in MGDO (-0.15 d y^{-1}). The clearest spatial pattern in MGDO is in the Nordic Mountains, where in north-eastern and south-western areas MGDO showed an advance and in the other areas MGDO showed a delay (Fig. S1). Only a small proportion of pixels showed significant trends in phenometrics (p-value <0.1), with percentages of 4%, 25%, and 25% observed in MGUP, MGDO, and GSL, respectively (Fig S3).

Climatic trends poorly explained the spatial variability of phenological trends (Fig. S4, S5, S6). We observed the clearest relationship in Nordic Mountains, where trends in pre-season temperatures and in pre-season precipitations are related to trends in MGUP (Fig. 1, S4a, S4c, S6; Pearson correlation coefficient= 0.56, and 0.4). The R^2 of multiple linear regression models estimating phenological trends based on climatic trends are consequently low, both at regional ($R^2 < 0.42$) and at continental scale ($R^2 < 0.17$) (Fig. S6).
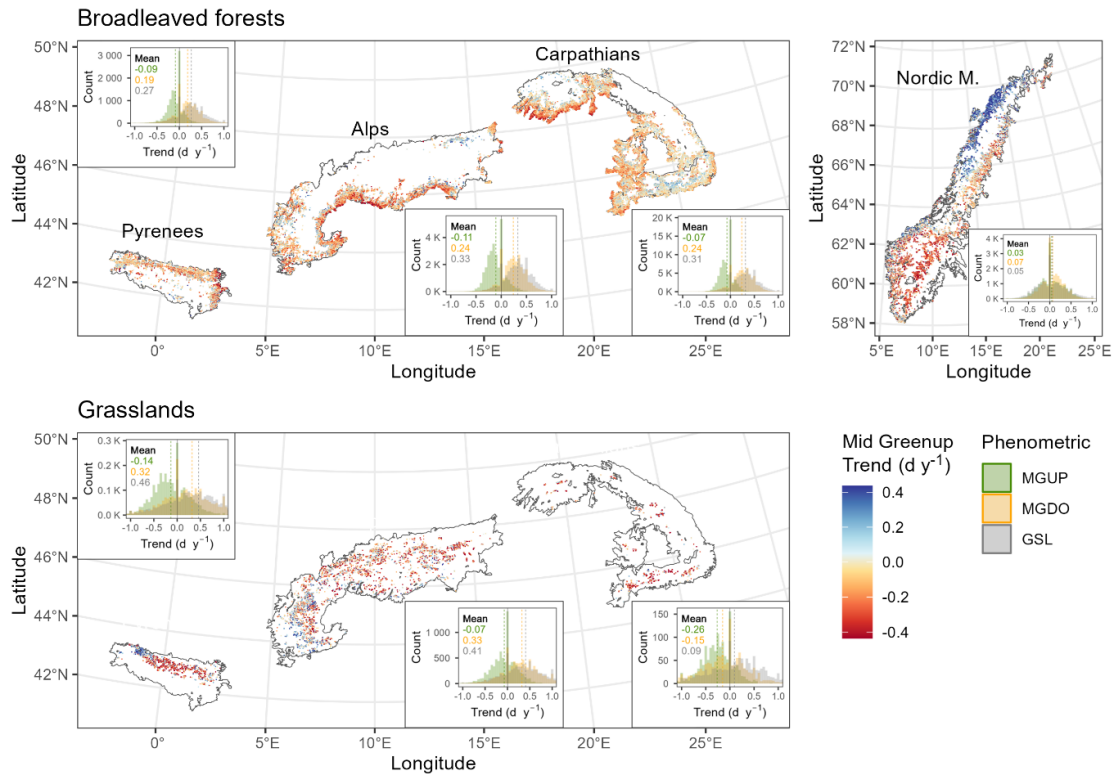
Fig. 1. Spatial distribution of trends in Mid Greenup in broadleaved forests and natural grasslands during 2001-2021 in the Alps, in the Carpathians, in the Nordic Mountains, and in the Pyrenees. Frequency distributions of trends in Mid Greenup, Mid Greendown and Growing Season Length are displayed in the small panels. All trends were estimated using the Theil-Sen estimator. Averages of trends are reported in the small panels as numbers and as vertical dashed lines in frequency distributions. Spatial Distribution of trends in MGDO and in GSL are available as Fig. S1 and Fig. S2, respectively. Abbreviations are as follows: MGUP = Mid Greenup; MGDO = Mid Greendown; GSL = Growing Season Length.

Elevational patterns in the phenological response

Our findings highlighted phenological patterns across elevations, which are not usually considered when phenological trends are described at 0.5° spatial resolution. The results obtained both under the approach followed by Vitasse et al. [28] and the linear mixed model analysis challenged previous findings. We found no evidence of more uniform spring phenology across elevations in forests in European mountains. Following the first approach, we observed an increasing trend in spring Elevation induced Phenological Shift (EPS) during 2001-2021 in the Alpine forests (range: 12-24 d 1000 m^{-1}) i.e., MGUP was advanced at low elevation and was delayed at high elevation, whereas Vitasse et al.[28] reported a decreasing EPS between 1960 and 2016 in Switzerland based on field observations (range: 22-34 d 1000 m^{-1}) (Fig. S7). The only decreasing spring EPS was in the Nordic Mountains where higher elevations are in the southern areas which experienced an advance in MGUP (Fig. 1). In this case, we attributed the observed EPS average trend to a spatial pattern rather than to an elevational pattern. Grassland spring EPS showed a decreasing trend on the Carpathians, i.e., MGUP advance was larger at higher elevations, but we identified no significant trend on the Alps and on the Pyrenees. Autumn phenology did not show clear variability across elevational (MAT) gradients (Fig. 2a), resulting in autumn EPS which are usually negative (i.e., earlier MGDO at higher elevations), but close to zero (Fig. S7). The only significant trend in autumn EPS was in Carpathian forests, where autumn phenology became more uniform across elevational gradients during 2001-2021 because of a larger MGDO delay at higher elevations.

The second approach we developed gave a better nuance of elevational pattern in phenological change (Tab. S1). In particular, the use of MAT instead of Elevation allowed the comparison of regions and sites at different latitudes. Regarding MGUP, MAT*Year interaction indicated a significant decrease in the uniformity of spring phenology across elevations in all forests except Nordic Mountains, because of MGUP advances at low elevations and MGUP delays at high elevations. On the contrary, we observed a more uniform spring phenology across elevations in natural grasslands, because of large advances at high elevations +and of delays at low elevations. Regarding MGDO, MAT*Year interaction indicated a more uniform autumn phenology across elevations, significant in all regions and vegetations but Pyrenean forests. The coefficient estimates for MAT in the MGUP models consistently showed negative values, indicating that MGUP occurred later in colder areas compared to warmer ones. Conversely, MAT control on autumn phenology was less clear and consistent. Grassland MGDO in the Alps and in the Carpathians occurred earlier in warmer areas compared to colder ones.

In some cases, we observed contrasting phenology trends at similar elevations between forests and grasslands (Fig 2.). We observed the most pronounced divergence in MGUP at low elevations in the Pyrenees (9 ≤ MAT ≤ 11), and the most pronounced divergence in MGDO at mid elevations in the Carpathians (4 ≤ MAT ≤ 7). As shown in Fig. S8 and Fig. S9, these diverging trends coexisted in adjacent areas.
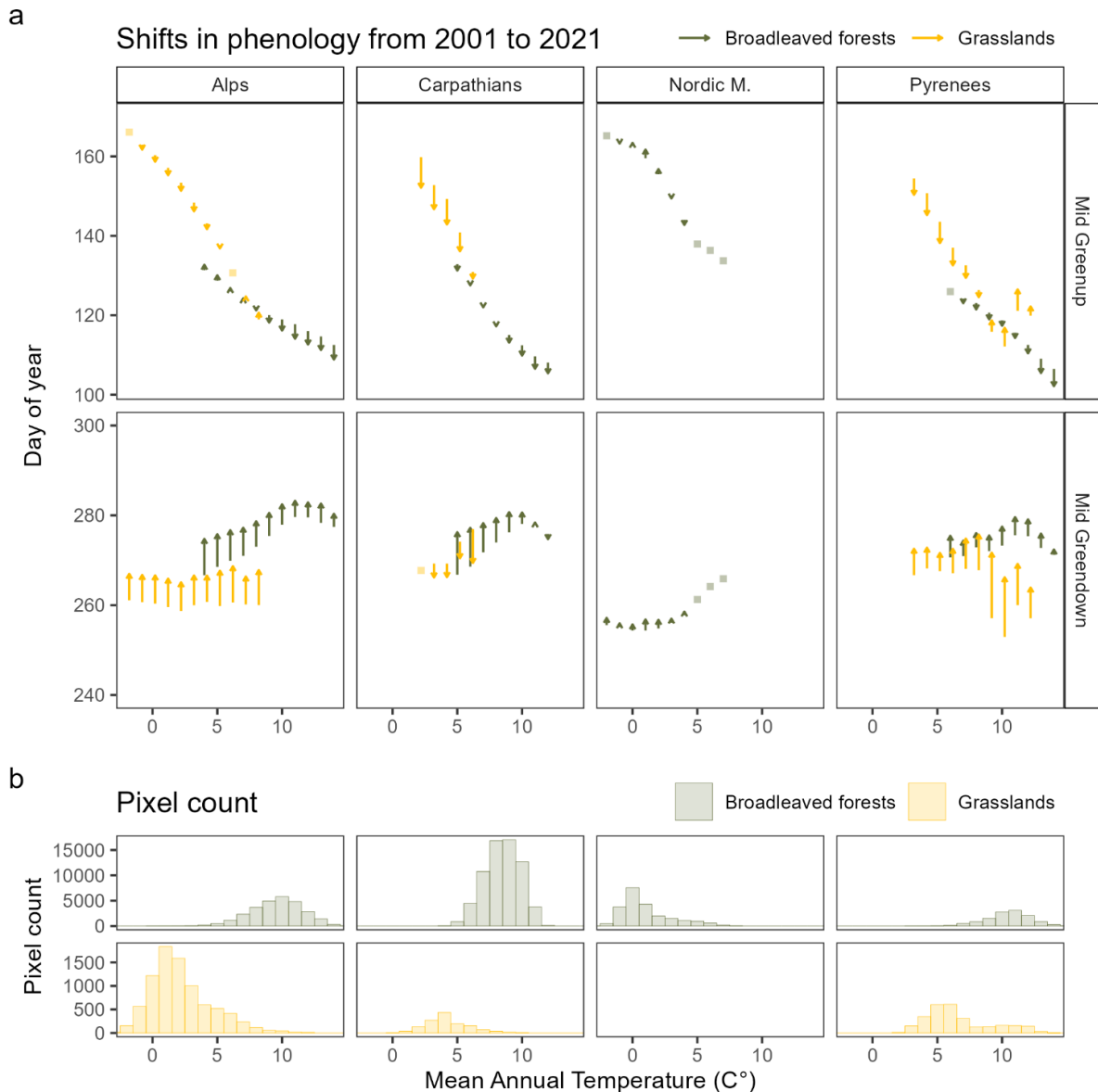

Fig. 2. Changes in broadleaved forest and natural grassland phenology during 2001-2021 in the Alps, Carpathians, Nordic Mountains, and Pyrenees along the temperature gradient. Panel a: Estimated change of Mid Greenup and of Mid Greendown from 2001 to 2021. Mid Greenup in 2001 and 2021 were estimated considering the average Mid Greenup and average trend in Mid Greenup in each class (i.e., after grouping based on region, vegetation type, rounded mean annual temperature). The average Mid Greenup was attributed to the central year of the observation period, values in 2001 (and 2021) were computed by subtracting (or adding) to it the average trend multiplied by ten (difference between central year and initial and final year). Mid Greendown estimates were computed in the same way. The

most evident patterns are that spring phenology is becoming less uniform along the elevational gradient in the Alpine, Carpathian and Pyrenean broadleaved forests, whereas it is becoming more uniform in natural grasslands. Autumn phenology is becoming more uniform, especially in Alpine and Carpathian broadleaved forests. Only classes with more than 100 observations were displayed. Panel b: Frequency distribution of pixels in each region and vegetation type across the temperature gradient.

Temporal decoupling of growing season length and gross primary productivity

Spatial and temporal GPP-GSL coupling showed different patterns. The two variables were highly spatially correlated both at regional and at continental scale: vegetation with longer growing seasons were associated to higher ecosystem productivity (Fig. 3a, 3c). Conversely, the relationships between temporal trends in GPP and temporal trends in GSL were much weaker (Fig. 3b, 3d). Both GSL and GPP have increased indeed during 2001-2021, but the extension of GSL explained <2% of the variance in the increase in GPP. The divergence of trends in GSL and trends in GPP showed clear spatial patterns (Fig. 4): in the western Carpathians and in the central area of the Nordic Mountains the extension in GSL was not followed by an increase in GPP, whereas in the Pyrenees and western Alps there was not large GSL extensions, but large increases in GPP occurred. Separate maps for GSL and GPP are available as Fig. S2 and Fig. S10, respectively.
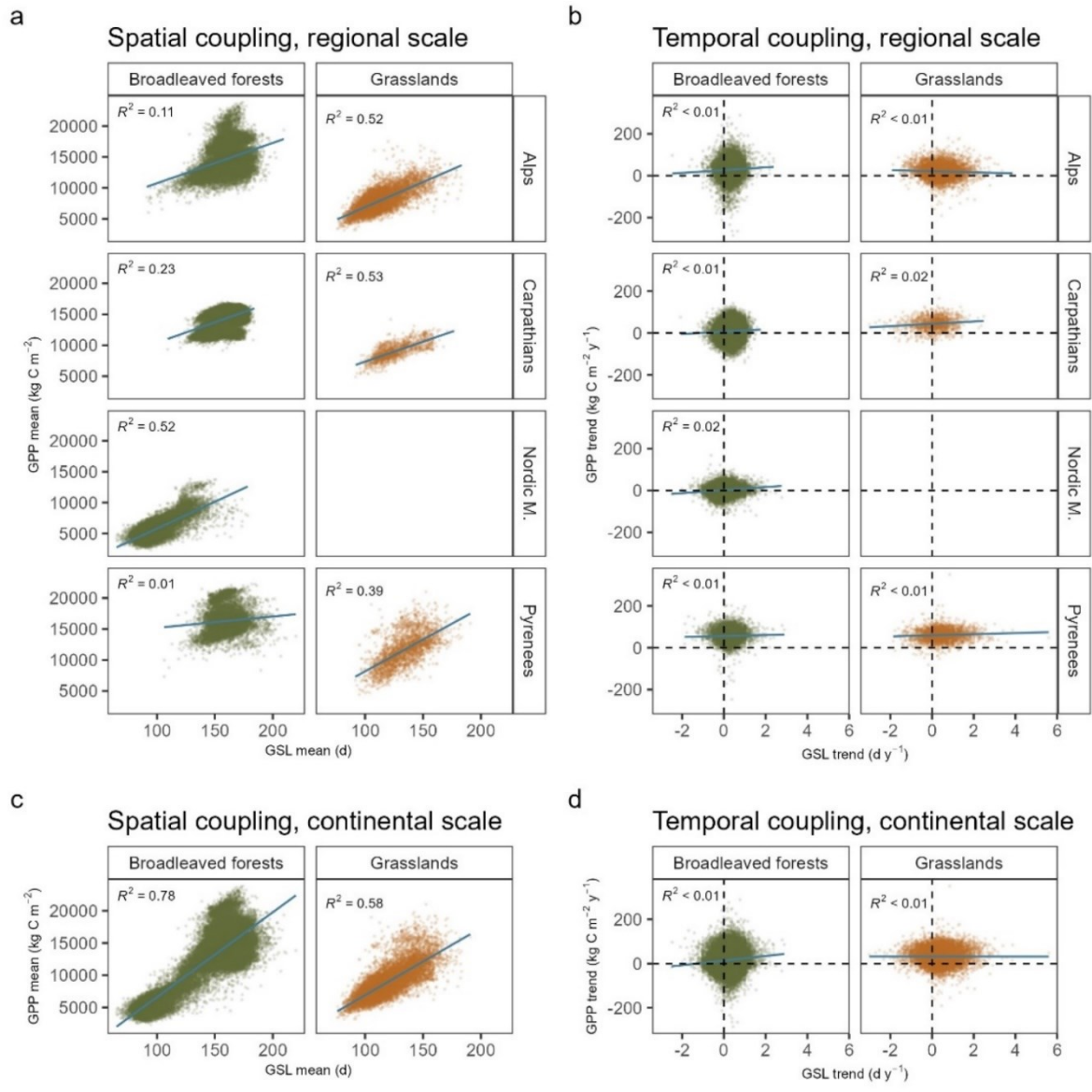
Fig. 3. Spatial and temporal coupling of Growing Season Length (GSL) and Gross Primary Productivity (GPP) at regional and continental scale. Spatial coupling was much stronger than temporal coupling. All trends were significant at probability level <0.001.
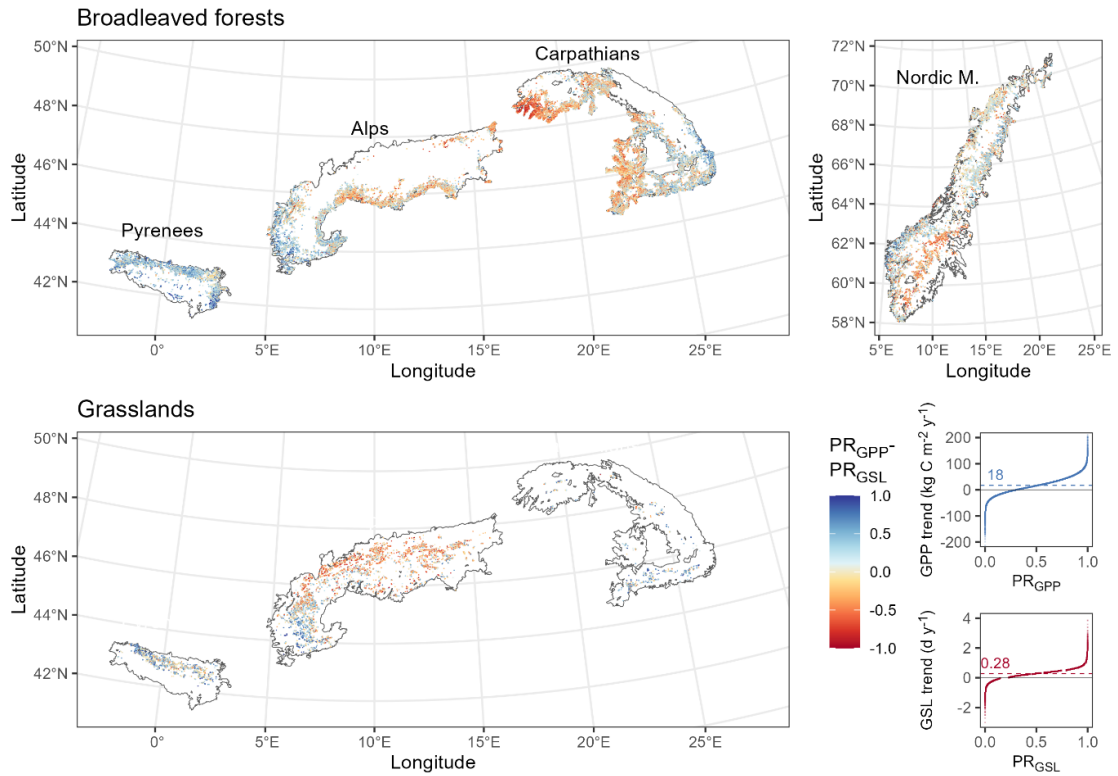
Fig. 4. Spatial distribution of differences in Percentile Ranks (PRs) of Gross Primary Productivity (GPP) and of Growing Season Length (GSL) trends. Values close to +1 indicate a large increase in GPP and a decrease in GSL, intermediate values indicate that GPP and GSL have the same direction and magnitude, and values close to -1 indicate a decrease in GPP and a large increase in GSL. The small panels show the trend value corresponding to each PR. Horizontal dashed lines indicate the mean trend.

Discussion

We observed clear spatial and elevational patterns in vegetation phenology trends in the European mountains, which challenge previous findings in literature. Forests MGUP showed a less uniform spring phenology during 2001-2021 because of advances at low elevations, no changes at mid-elevations and delays at high elevations. Despite GSL and GPP both showed positive temporal trends, the portion of variation in GPP increase explained by GSL extension is <2%, contrasting with the previously observed temporal coupling[2,3,5].

The smaller advance we observed at the beginning of the season compared to previous studies[1] may be attributed to the control of photoperiod, which limits further advances of spring phenology, and to warmer winter temperatures, which make it harder to meet chilling requirements for leaf unfolding[1,13,15]. A decrease in phenological sensitivity to warming has already been observed in widely distributed species in the European mountains broadleaved forests[13]. Regarding autumn phenology, our study revealed large delays in MGDO, which contradicts previous research indicating no trend during 1998-2014[29] and earlier leaf senescence in response to higher productivity[20]. However, our findings are consistent with numerous free-air CO_2 enrichment experiments, which have also demonstrated delayed autumn phenology in response to increased CO_2 levels and experimental warming [30]. Additionally, remote sensing data from 1985 to 2015 have shown similar autumn trends[31], and recent studies have provided evidence that plants can both extend their growing season and enhance productivity through acclimation[21].

The finer spatial resolution of our study compared to previous studies allowed us to assess the variability of phenological trends across space and to explore the nuances of their elevational patterns[27]. Differently from previous findings[28], we report a less uniform spring phenology across the elevational gradient in broadleaved forests. This pattern was consistent across sites and was determined by advances in spring phenology at low elevation and by delays at high elevation. Elevational patterns in grassland and broadleaved forest phenology were opposite. Grassland spring phenology was delayed at low elevations and was advanced at high elevations, leading to a more uniform grassland spring phenology across elevations. Elevational patterns in grassland phenology trends have rarely been explored, but a few studies studied them in the European Alps[23,32]. Even though the trends we observed are much smaller in magnitude (MGUP trend ≈ 0.1 d y^{-1} vs. ≈ 1 d y^{-1}), our findings are consistent with the reported larger advance at mid-high elevations compared to low elevations[23]. The divergent phenological trends observed in broadleaved forests and grasslands at similar elevations raise inquiries regarding the distinct physiological mechanisms that govern plant phenology, thereby suggesting paths for additional research. Moreover, these diverging phenological responses to the changing climate are increasingly recognized as major forces

structuring natural communities through the alteration of species interactions[33]. Regarding autumn phenology, our findings confirm that MAT poorly explained the spatial variation in MGDO[34]. In fact, autumn phenology is controlled by many interacting factors in addition to temperatures, including photoperiod, spring and summer photosynthesis[20], and water availability[35]. We observed a more pronounced MGDO delay at high elevations compared to low elevations, leading to a more uniform autumn phenology across elevations especially in forests (Fig. 2, Alps, Carpathians). We hypothesised that spring and summer droughts, along with heatwaves, exerted a more pronounced influence in low elevation vegetations, where a further delay of autumn phenology was therefore constrained[35,36].

Climatic trends poorly explained phenological trends, suggesting that there is not a single regionally or continentally valid major climatic driver of changes in phenology. Moreover, the low prediction capability of the climate variables can be attributed to the large deviation between climate variables estimated by downscaling coarse resolution global products and the actual microclimate near buds[37].

The observed temporal decoupling of GSL and GPP suggests a weakening of the 'warmer spring–bigger sink' mechanism[38]. In the observed area and period, growing season length was not the main limiting factor to the increase in productivity. Other key factors constraining the tree growth following the extension of the growing season could be disturbances, reduced water supply and shortened trees' lifespan[39–42]. Given these findings, it is crucial for biogeochemical models to incorporate this decoupling when simulating the potential carbon uptake of terrestrial ecosystems in future climate change scenarios.

Bibliography

1. Fu, Y. H. *et al.* Global warming is increasing the discrepancy between green (actual) and thermal (potential) seasons of temperate trees. *Glob Chang Biol* **29**, 1377–1389 (2023).

2. Dragoni, D. *et al.* Evidence of increased net ecosystem productivity associated with a longer vegetated season in a deciduous forest in south-central Indiana, USA. *Glob Chang Biol* **17**, 886–897 (2011).

3. Keenan, T. F. *et al.* Net carbon uptake has increased through warming-induced changes in temperate forest phenology. *Nat Clim Chang* **4**, 598–604 (2014).

4. Richardson, A. D. *et al.* Influence of spring and autumn phenological transitions on forest ecosystem productivity. *Philosophical Transactions of the Royal Society B: Biological Sciences* **365**, 3227–3246 (2010).

5. Xia, J. *et al.* Joint control of terrestrial gross primary productivity by plant phenology and physiology. *Proc Natl Acad Sci U S A* **112**, 2788–2793 (2015).

6. Piao, S. *et al.* Net carbon dioxide losses of northern ecosystems in response to autumn warming. *Nature* **451**, 49–52 (2008).

7. Didion-Gency, M. *et al.* Chronic warming and dry soils limit carbon uptake and growth despite a longer growing season in beech and oak. *Plant Physiol* (2023) doi:10.1093/plphys/kiad565.

8. Buermann, W. *et al.* Widespread seasonal compensation effects of spring warming on northern plant productivity. *Nature* **562**, (2018).

9. Piao, S. *et al.* Plant phenology and global climate change: Current progresses and challenges. *Glob Chang Biol* **25**, 1922–1940 (2019).

10. Richardson, A. D. *et al.* Climate change, phenology, and phenological control of vegetation feedbacks to the climate system. *Agric For Meteorol* **169**, 156–173 (2013).

11. Peñuelas, J., Rutishauser, T. & Filella, I. Phenology Feedbacks on Climate Change. *Science (1979)* **324**, 887–888 (2009).

12. Fu, Y. H. *et al.* Declining global warming effects on the phenology of spring leaf unfolding. *Nature 2015 526:7571* **526**, 104–107 (2015).

13. Meng, L. *et al.* Photoperiod decelerates the advance of spring phenology of six deciduous tree species under climate warming. *Glob Chang Biol* **27**, 2914–2927 (2021).

14. Menzel, A. *et al.* Climate change fingerprints in recent European plant phenology. *Glob Chang Biol* **26**, 2599–2612 (2020).

Diverging trends in plant phenology across European mountains in a warming world
Andreatta et al. (2024), *unpublished*

15. Way, D. A. & Montgomery, R. A. Photoperiod constraints on tree phenology, performance and migration in a warming world. *Plant Cell Environ* **38**, 1725–1736 (2015).

16. Gill, A. L. *et al.* Changes in autumn senescence in northern hemisphere deciduous trees: a meta-analysis of autumn phenology studies. *Ann Bot* **116**, 875–888 (2015).

17. Jiang, N. *et al.* Warming does not delay the start of autumnal leaf coloration but slows its progress rate. *Global Ecology and Biogeography* **31**, 2297–2313 (2022).

18. Zhang, Y. *et al.* Autumn canopy senescence has slowed down with global warming since the 1980s in the Northern Hemisphere. *Communications Earth & Environment 2023 4:1* **4**, 1–9 (2023).

19. Zohner, C. M. *et al.* Effect of climate warming on the timing of autumn leaf senescence reverses after the summer solstice. *Science (1979)* **381**, (2023).

20. Zani, D., Crowther, T. W., Mo, L., Renner, S. S. & Zohner, C. M. Increased growing-season productivity drives earlier autumn leaf senescence in temperate trees. *Science (1979)* **370**, 1066–1071 (2020).

21. Marqués, L. *et al.* Acclimation of phenology relieves leaf longevity constraints in deciduous forests. *Nat Ecol Evol* (2023) doi:10.1038/s41559-022-01946-1.

22. Xie, J. *et al.* Altitude-dependent influence of snow cover on alpine land surface phenology. *J Geophys Res Biogeosci* **122**, 1107–1122 (2017).

23. Xie, J. *et al.* Spring Temperature and Snow Cover Climatology Drive the Advanced Springtime Phenology (1991–2014) in the European Alps. *J Geophys Res Biogeosci* **126**, (2021).

24. Asam, S. *et al.* Relationship between Spatiotemporal Variations of Climate, Snow Cover and Plant Phenology over the Alps—An Earth Observation-Based Analysis. *Remote Sensing 2018, Vol. 10, Page 1757* **10**, 1757 (2018).

25. Jeong, S. J., Ho, C. H., Gim, H. J. & Brown, M. E. Phenology shifts at start vs. end of growing season in temperate vegetation over the Northern Hemisphere for the period 1982–2008. *Glob Chang Biol* **17**, 2385–2399 (2011).

26. Pan, Y. *et al.* Climate-driven land surface phenology advance is overestimated due to ignoring land cover changes. *Environmental Research Letters* **18**, 044045 (2023).

27. Zhang, X. *et al.* Exploration of scaling effects on coarse resolution land surface phenology. *Remote Sens Environ* **190**, 318–330 (2017).

28. Vitasse, Y., Signarbieux, C. & Fu, Y. H. Global warming leads to more uniform spring phenology across elevations. *Proceedings of the National Academy of Sciences* **115**, 1004–1008 (2018).

29. Wang, X. *et al.* No trends in spring and autumn phenology during the global warming hiatus. *Nature Communications 2019 10:1* **10**, 1–10 (2019).

Diverging trends in plant phenology across European mountains in a warming world
Andreatta et al. (2024), *unpublished*

30. Norby, R. J. Comment on "Increased growing-season productivity drives earlier autumn leaf senescence in temperate trees". *Science (1979)* **371**, (2021).

31. Shen, M. *et al.* Can changes in autumn phenology facilitate earlier green-up date of northern vegetation? *Agric For Meteorol* **291**, 108077 (2020).

32. Filippa, G. *et al.* Climatic Drivers of Greening Trends in the Alps. *Remote Sens (Basel)* **11**, 2527 (2019).

33. Rudolf, V. H. W. The role of seasonal timing and phenological shifts for species coexistence. *Ecol Lett* **22**, 1324–1338 (2019).

34. Richardson, A. D., Hufkens, K., Li, X. & Ault, T. R. Testing Hopkins' Bioclimatic Law with PhenoCam data. *Appl Plant Sci* **7**, e01228 (2019).

35. Wu, C. *et al.* Increased drought effects on the phenology of autumn leaf senescence. *Nat Clim Chang* **12**, (2022).

36. Song, J. *et al.* A meta-analysis of 1,119 manipulative experiments on terrestrial carbon-cycling responses to global change. *Nature Ecology & Evolution 2019 3:9* **3**, 1309–1320 (2019).

37. Vitasse, Y. *et al.* Impact of microclimatic conditions and resource availability on spring and autumn phenology of temperate tree seedlings. *New Phytologist* **232**, (2021).

38. Piao, S. *et al.* Weakening temperature control on the interannual variations of spring carbon uptake across northern lands. *Nature Climate Change 2017 7:5* **7**, 359–363 (2017).

39. Pugh, T. A. M., Arneth, A., Kautz, M., Poulter, B. & Smith, B. Important role of forest disturbances in the global biomass turnover and carbon sinks. *Nature Geoscience 2019 12:9* **12**, 730–735 (2019).

40. Brienen, R. J. W. *et al.* Forest carbon sink neutralized by pervasive growth-lifespan trade-offs. *Nature Communications 2020 11:1* **11**, 1–10 (2020).

41. Ruehr, S. *et al.* Evidence and attribution of the enhanced land carbon sink. *Nat Rev Earth Environ* **4**, 518–534 (2023).

42. Lian, X. *et al.* Diminishing carryover benefits of earlier spring vegetation growth. *Nat Ecol Evol* (2024) doi:10.1038/s41559-023-02272-w.

43. Melaas, E. K. *et al.* Using FLUXNET data to improve models of springtime vegetation activity onset in forest ecosystems. *Agric For Meteorol* **171–172**, 46–56 (2013).

44. Gray, J., Sulla-Menashe, D. & Friedl, M. A. User guide to collection 6 modis land cover dynamics (mcd12q2) product. *NASA EOSDIS Land Processes DAAC: Missoula, MT, USA* **6**, 1–8 (2022).

45. Yao, J. *et al.* Accelerated dryland expansion regulates future variability in dryland gross primary production. *Nature Communications 2020 11:1* **11**, 1–10 (2020).

46. Peifer, H. *About the EEA reference grid*. (2011).

47. Büttner, G. *et al. Copernicus Land Monitoring Service-CORINE Land Cover. User Manual*. https://land.copernicus.eu/en/technical-library/clc-product-user-manual/@@download/file (2021).

48. Kosztra, B., Büttner, G., Hazeu, G. & Arnold, S. Updated CLC illustrated nomenclature guidelines. *European Environment Agency: Wien, Austria* 1–124 (2017).

49. Muñoz-Sabater, J. *et al.* ERA5-Land: a state-of-the-art global reanalysis dataset for land applications. *Earth Syst Sci Data* **13**, 4349–4383 (2021).

50. Cortés, J. *et al.* Where Are Global Vegetation Greening and Browning Trends Significant? *Geophys Res Lett* **48**, (2021).

51. Sen, P. K. Estimates of the Regression Coefficient Based on Kendall's Tau. *J Am Stat Assoc* **63**, 1379–1389 (1968).

52. Huang, Z., Zhou, L. & Chi, Y. Spring phenology rather than climate dominates the trends in peak of growing season in the Northern Hemisphere. *Glob Chang Biol* **29**, 4543–4555 (2023).

53. Kendall, M. G. *Rank Correlation Methods*. (Oxford University Press, Oxford, 1975).

54. Mann, H. B. Nonparametric Tests Against Trend. *Econometrica* **13**, 245 (1945).

55. Bates, D., Mächler, M., Bolker, B. & Walker, S. Fitting Linear Mixed-Effects Models Using lme4. *J Stat Softw* **67**, 1–48 (2015).

56. Kamil Bartoń. MuMIn: Multi-Model Inference. Preprint at https://CRAN.R-project.org/package=MuMIn (2023).

57. R Core Team. R: A Language and Environment for Statistical Computing. Preprint at https://www.R-project.org/. (2023).

Supplementary Materials

This section includes:

- Materials and Methods
- Figs. S1 to S10
- Table S1

Materials and methods

All the workflow is fully reproducible, and we provide a structured document reporting and commenting in detail all the codes used for this study at the link https://drive.google.com/file/d/1oSCTsJ-PqcEi1UV6lM11bnAMiXgW_IlZ/view?usp=drive_link. We accessed a set of datasets including phenological, climatic, productivity and topographical information through the Google Earth Engine Data Catalog (https://developers.google.com/earth-engine/datasets). We considered the Alps, the Carpathians, the Pyrenees, and the Nordic Mountains as delineated in the European Mountain Areas dataset (European Environment Agency, 2008).

Phenology, productivity, terrain, and vegetation datasets

We obtained phenological dates from the Terra and Aqua combined Moderate Resolution Imaging Spectroradiometer Land Cover Dynamics product Version 6.1 at 500m resolution, which in previous studies showed a good agreement with phenometrics derived from eddy covariance data[21,43,44]. We chose Mid Greenup (MGUP) and Mid Greendown (MGDO) as phenometrics, since Greenup and Dormancy metrics are more prone to errors in high elevation areas[21,44]. We computed Growing Season Length (GSL) as the difference between MGDO and MGUP. We selected only pixels with all phenological observations from 2001 to 2021 flagged as «best» quality or «good» quality according to the quality assurance scores bands. We derived Yearly Gross Primary Productivity (GPP) from the MODIS Terra Net Primary Production Gap-Filled Yearly L4 Global 500 m, which has proved to reliably quantify spatiotemporal variability in GPP[45]. Moreover, for each selected pixel we extracted Elevation from the Copernicus Digital Elevation Model GLO-30 dataset. All these datasets were rescaled to the spatial resolution of 500 m and reprojected to ETRS89-LAEA Europe coordinate reference system[46]. We investigated two widely distributed vegetation types: "natural grasslands" and "broadleaved forests", as defined in the Corine Land Cover taxonomy[47,48]. "Natural grasslands" class excludes "pastures, meadows and other permanent grasslands under agricultural use", but includes grasslands affected by "sporadic extensive grazing with low livestock unit/ha"[48]. Since vegetation index time series may be affected by biomass removal through grazing and not only by phenological development, grassland MGDO estimates should be considered with caution. To calculate rescaled pixels at a resolution of 500 m while filtering areas at the boundaries between different vegetation types, we initially chose pixels with consistent classification across the four available Corine Land Cover products (2000, 2006, 2012, 2018). Subsequently, we rescaled the Corine Land Cover pixels, originally at a resolution of 100 m, to a resolution of 500 m. We then focused solely on the rescaled pixels where at least 90% of the area was characterized by the same vegetation type.

Climate datasets

We used ERA5-Land monthly aggregated ECMWF Climate Reanalysis product[49], extracting trends in the mean temperatures of the pre-season, and of the growing season. We defined the pre-season as the average month of Mid Greenup for each pixel during the 21-year investigation, as well as the two preceding months. We defined the growing season as the months encompassing both the average month of Mid Greenup and Mid Greendown for each pixel during the 21-year investigation period. To match phenology spatial resolution, we downscaled temperatures from 11132 m spatial resolution to 500 m by applying an approach based on lapse rate[14]: first, for each temperature map and for each region, we computed the lapse rate. Then, we adjusted the ERA5 temperatures by adding the product of the lapse rate and the difference between the elevation of each pixel at 500 m resolution and the mean elevation of the overlapping ERA5 pixel. We chose Mean Annual Temperature (MAT) during 2001-2021 as a proxy variable to investigate phenological patterns across elevational gradients, since it is more informative than elevation when comparing climates across different regions and latitudes, and phenological variation is well explained by annual mean temperature[34].

Temporal trends

We estimated trends using the Theil-Sen estimator, a nonparametric method not affected by outliers and therefore frequently used in phenological studies[50–52]. We evaluated the significance of the trends by applying the Mann-Kendall nonparametric test[53,54]. We used the "sens.slope" function of the "trends" R package to estimate trends and significance. We displayed and inspected the spatial distributions of the trends, and identified local hotspots and coldspots. To explore the role of climatic trends in shaping phenological response, we computed the Pearson correlation coefficients between each phenometric and a set of climatic variables including trend of precipitations and temperature of the pre-season and of the growing season. Lastly, we fitted multiple linear regression models to estimate the amount of variability in phenological changes which can be explained by climatic trends at regional scale and at continental scale.

Elevational patterns in the phenological response

To assess the uniformization of spring phenology across elevations, we first applied the same analysis performed by Vitasse et al.[28], then we further analysed the patterns using mixed effect models. Under both approaches we developed a separate model for each region and vegetation type. The Elevation Induced Phenological Shift (EPS), expressed as d 1000 m^{-1}, was determined for each year by calculating the slope of the linear regression between MGUP and Elevation. Once we computed EPSs, we identified temporal trends by fitting linear

regressions between EPS and Year. We analysed autumn EPSs following the same procedure. Regarding the second approach, we defined mixed models including MGUP (or MGDO) as a response variable, Year, MAT and their interaction as fixed effect, and pixel ID as a random intercept effect. The coefficient of the interaction between Year and MAT therefore indicates the increase of effectiveness of Year on MGUP for a one unit increase in MAT. We used the "lmer" function of the "lme4" R package to fit the mixed effect models[55], and the "r.squared.GLMM" function of the "MuMIn" R package to compute the conditional R^2, which gives the amount of variance explained by both fixed and random factors [56].

Temporal coupling of growing season length and gross primary productivity

We first assessed the spatial coupling of GSL and GPP by fitting a linear regression between mean GSL during 2001-2021 in each pixel and mean GPP during 2001-2021 in each pixel. Then, we evaluated the existence of temporal coupling by regressing trends in GSL during 2001-2021 and trends in GPP during 2001-2021. We estimated trends with Theil-Sen estimator. We investigated the relationships both at regional and at continental scale (i.e., analysing the dataset without separating into the four regions under investigation). To investigate spatial patterns in GSL-GPP coupling we analysed the difference in percentile ranks (PRs) computed for GPP and for GSL. First, we computed the PR of each value i.e., the proportion of values in the input vector that are less than or equal to that value, for GPP and GSL using the "ecdf" function of the "stats" package in R[57]. Then we calculated the difference between PR_{GPP} and the PR_{GSL}. Values close to +1 indicate a large increase in GPP and a decrease in GSL, intermediate values indicate that GPP and GSL trends have the same direction and magnitude, and values close to -1 indicate a decrease in GPP and a large increase in GSL.

Diverging trends in plant phenology across European mountains in a warming world
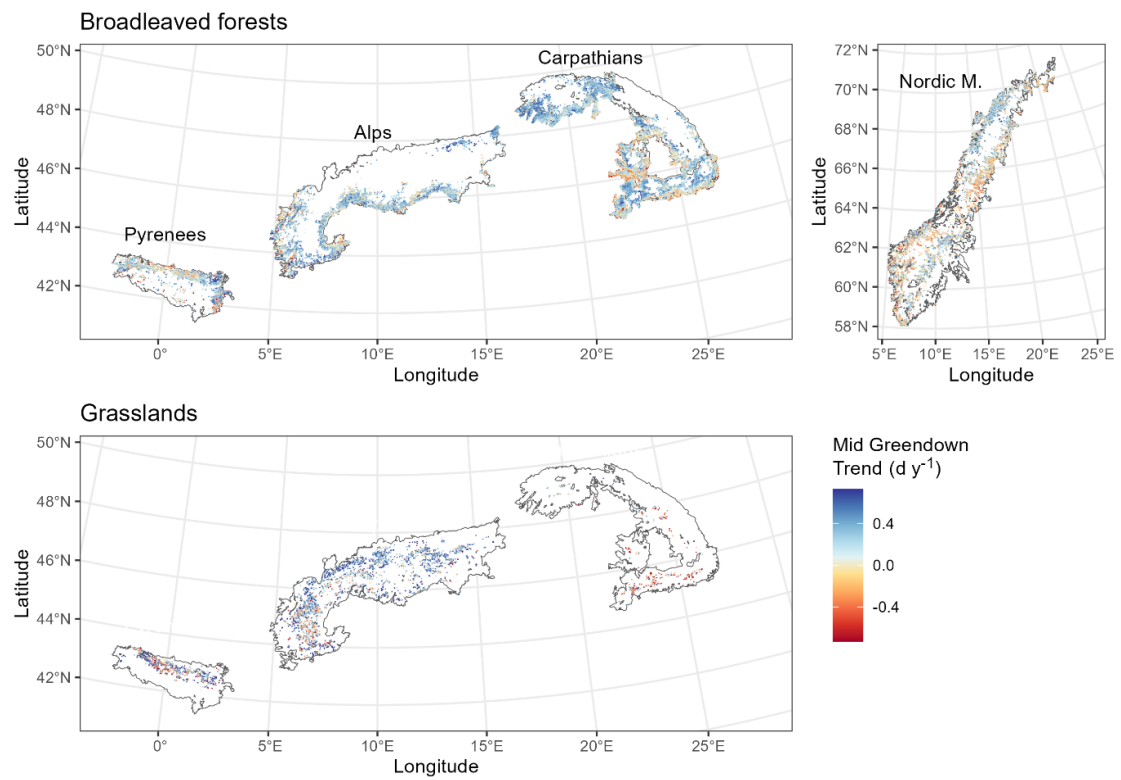Andreatta et al. (2024), *unpublished*

Fig. S1. Spatial distribution of trends in Mid Greendown in broadleaved forests and natural grasslands during 2001-2021 in the Alps, in the Carpathians, in the Nordic Mountains, and in the Pyrenees. Trends were estimated using the Theil-Sen estimator.
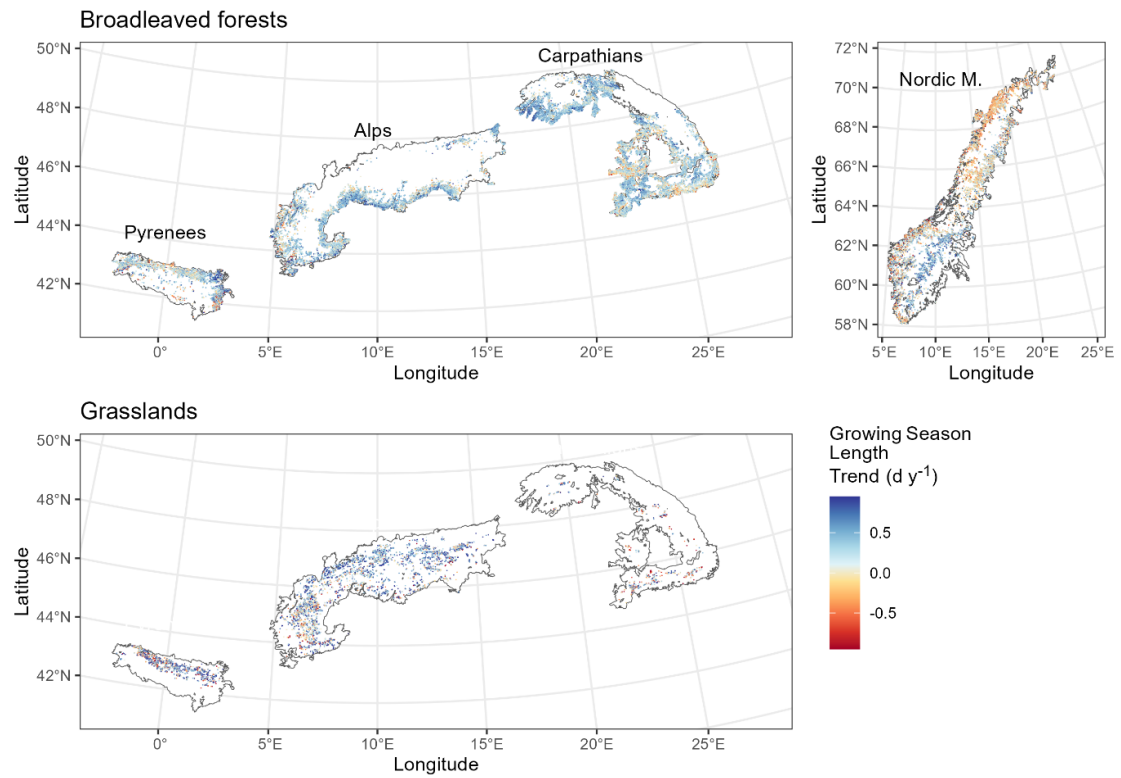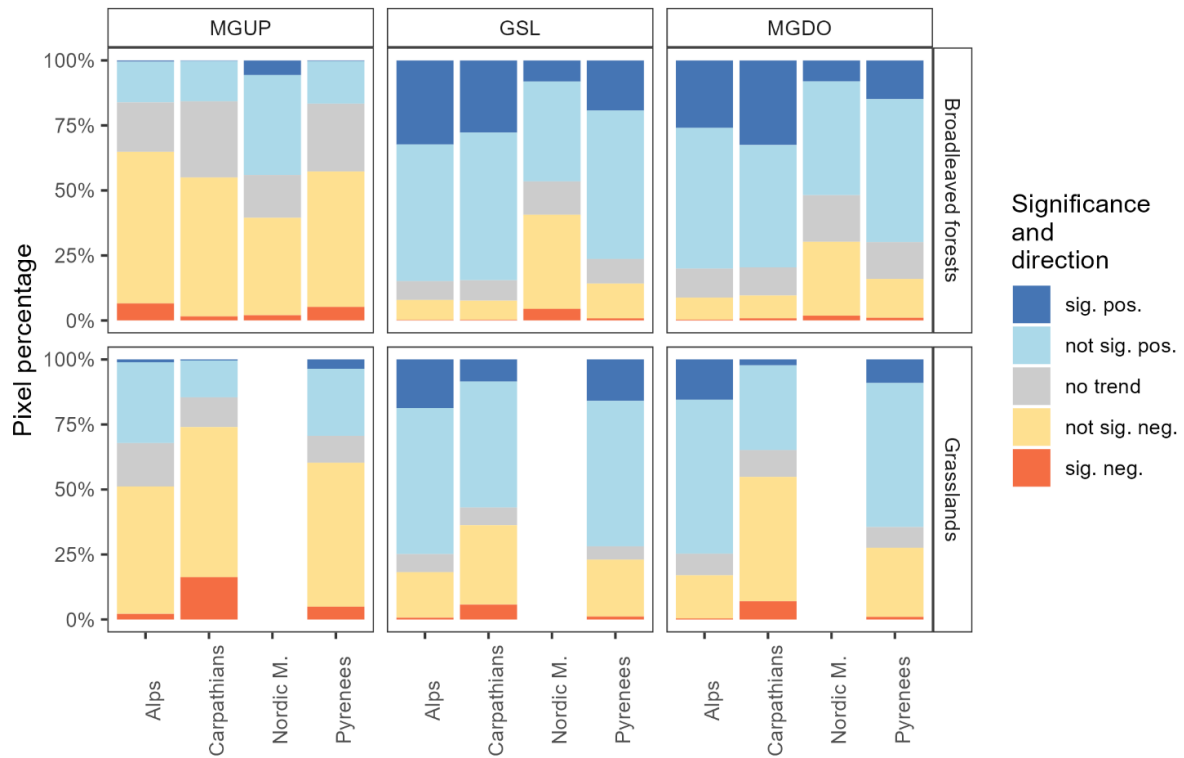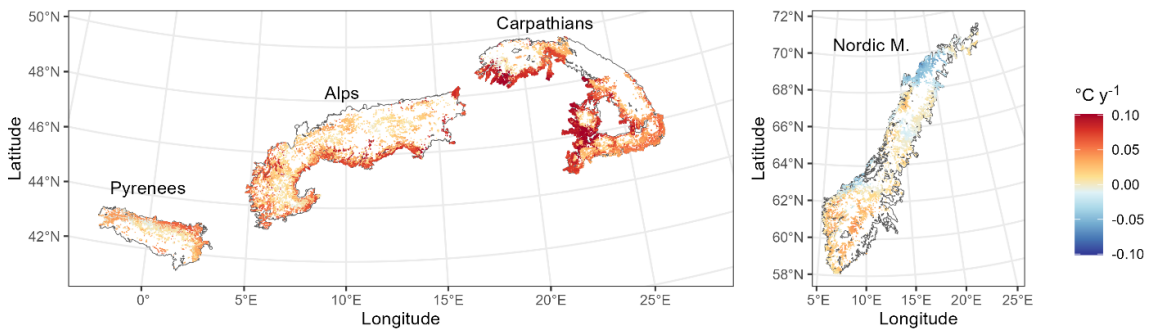
Fig. S2. Spatial distribution of trends in Growing Season length in broadleaved forests and natural grasslands during 2001-2021 in the Alps, in the Carpathians, in the Nordic Mountains, and in the Pyrenees. Trends were estimated using the Theil-Sen estimator.

Fig. S3. Statistical significance and direction of phenological trends in broadleaved forests and natural grasslands during 2001-2021 in the Alps, in the Carpathians, in the Nordic Mountains, and in the Pyrenees. Trends were estimated using the Theil-Sen estimator. Significance was evaluated by applying the Mann-Kendall nonparametric test, considering statistically significant probability value <0.1. Abbreviations are as follows: MGUP = Mid Greenup; GSL = Growing Season Length, MGDO = Mid Greendown.
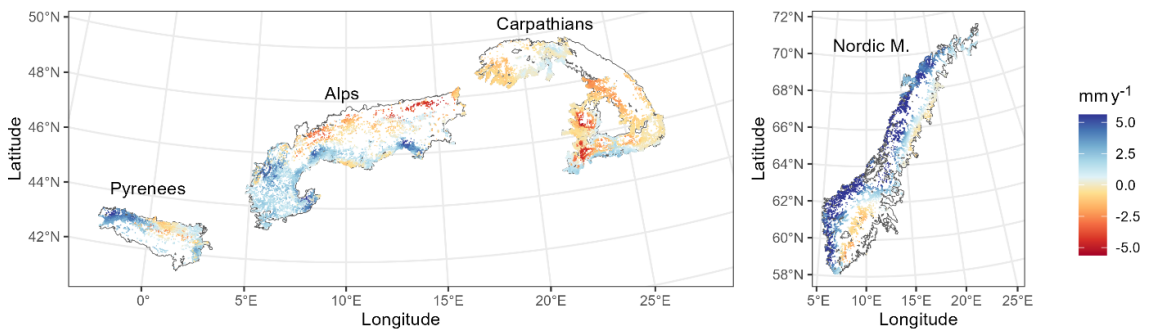
Climatic trends

a Trends in pre-season temperatures

b Trends in growing season temperatures
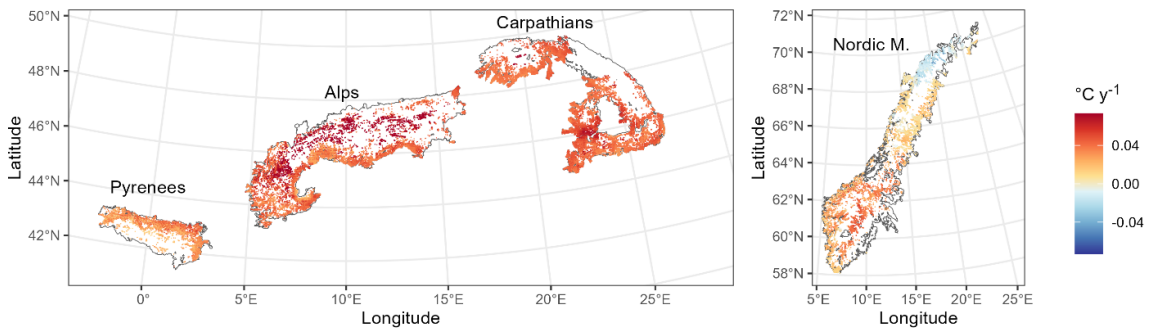
c Trends in pre-season precipitations

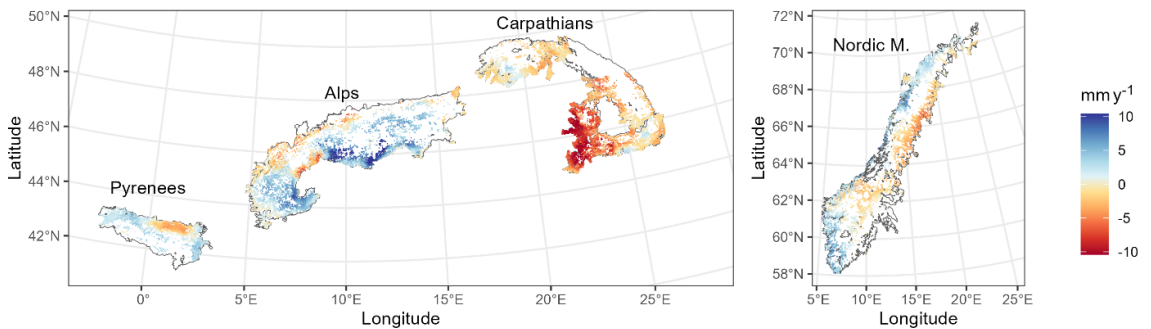### d Trends in growing season precipitations

Fig. S4. Spatial distribution of trends in temperatures and precipitations during 2001-2021 in the Alps, in the Carpathians, in the Nordic Mountains, and in the Pyrenees. Trends were estimated using the Theil-Sen estimator. The pre-season was defined as the average month of Mid Greenup for each pixel during the 21-year investigation, as well as the two preceding months. The growing season was defined as the months encompassing both the average month of Mid Greenup and Mid Greendown for each pixel during the 21-year investigation period".
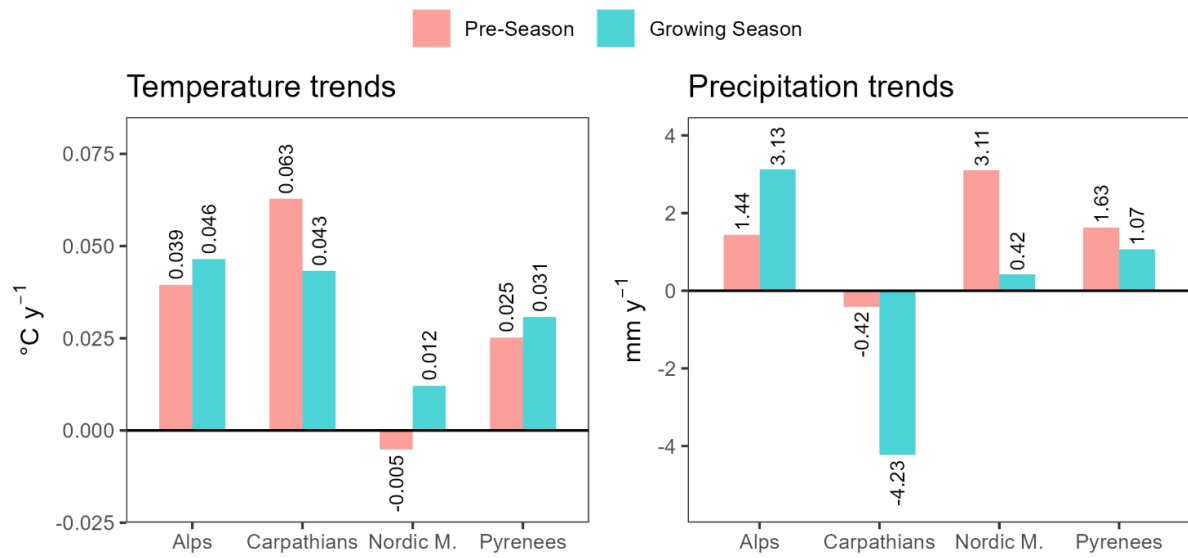
Fig. S5 Regional averages of climatic trends in temperature and in precipitation during 2001-2021. Colours indicate the period under consideration: the pre-season was defined as the average month of Mid Greenup for each pixel during the 21-year investigation, as well as the two preceding months. The growing season was defined as the months encompassing both the average month of Mid Greenup and Mid Greendown for each pixel during the 21-year investigation period".

Diverging trends in plant phenology across European mountains in a warming world
Andreatta et al. (2024), *unpublished*

a Relationship between climatic and phenological trends

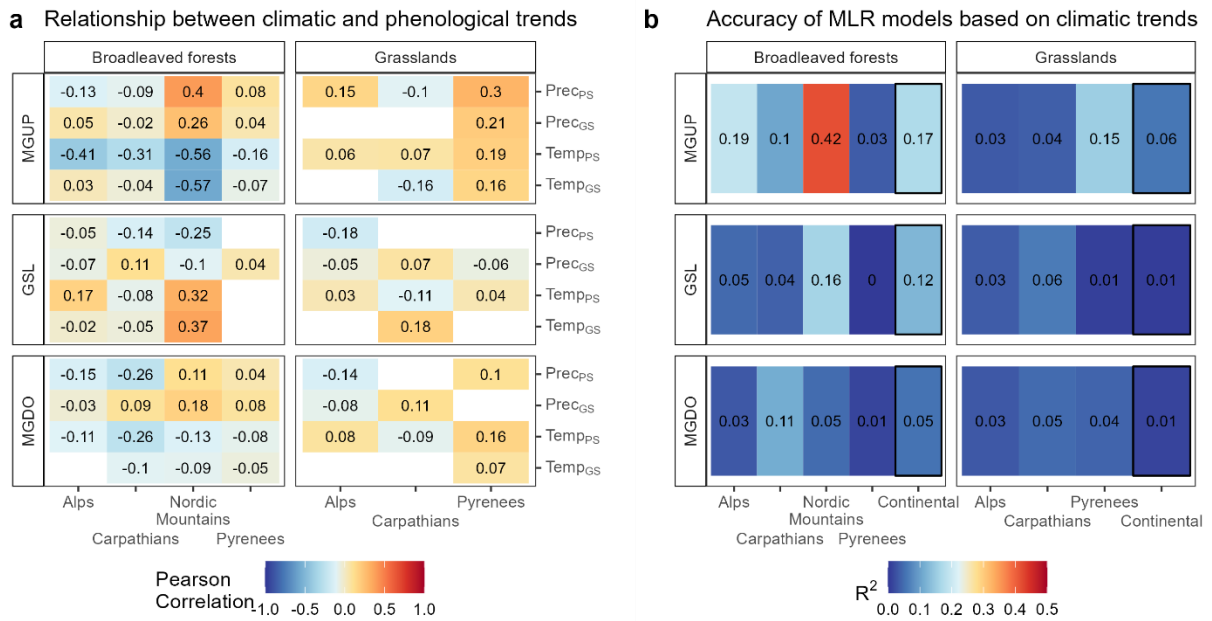**b** Accuracy of MLR models based on climatic trends

Fig. S6. Climatic drivers of phenological trends. Panel a: Pearson correlation between climatic and phenological trends. White cell background indicates non-significant ($p<0.05$) correlations. Abbreviations are as follows: MGUP, Trend in Mid Greenup; MGDO, Trend in Mid Greendown; GSL, Trend in Growing Season Length; Temp, trend in mean monthly temperatures during the pre-season (PS) and during the growing season (GS); Prec, trend in precipitations cumulated during the pre-season (PS) and during the growing season (GS). The pre-season was defined as the average month of Mid Greenup for each pixel during the 21-year investigation, as well as the two preceding months. The growing season was defined as the months encompassing both the average month of Mid Greenup and Mid Greendown for each pixel during the 21-year investigation period. Panel b: Accuracy (R^2) of Multiple Linear Regression models estimating trends in phenometrics based on trends in the climatic variables listed in panel a. Trends in the climatic variables explained little of the variability of phenological trends.
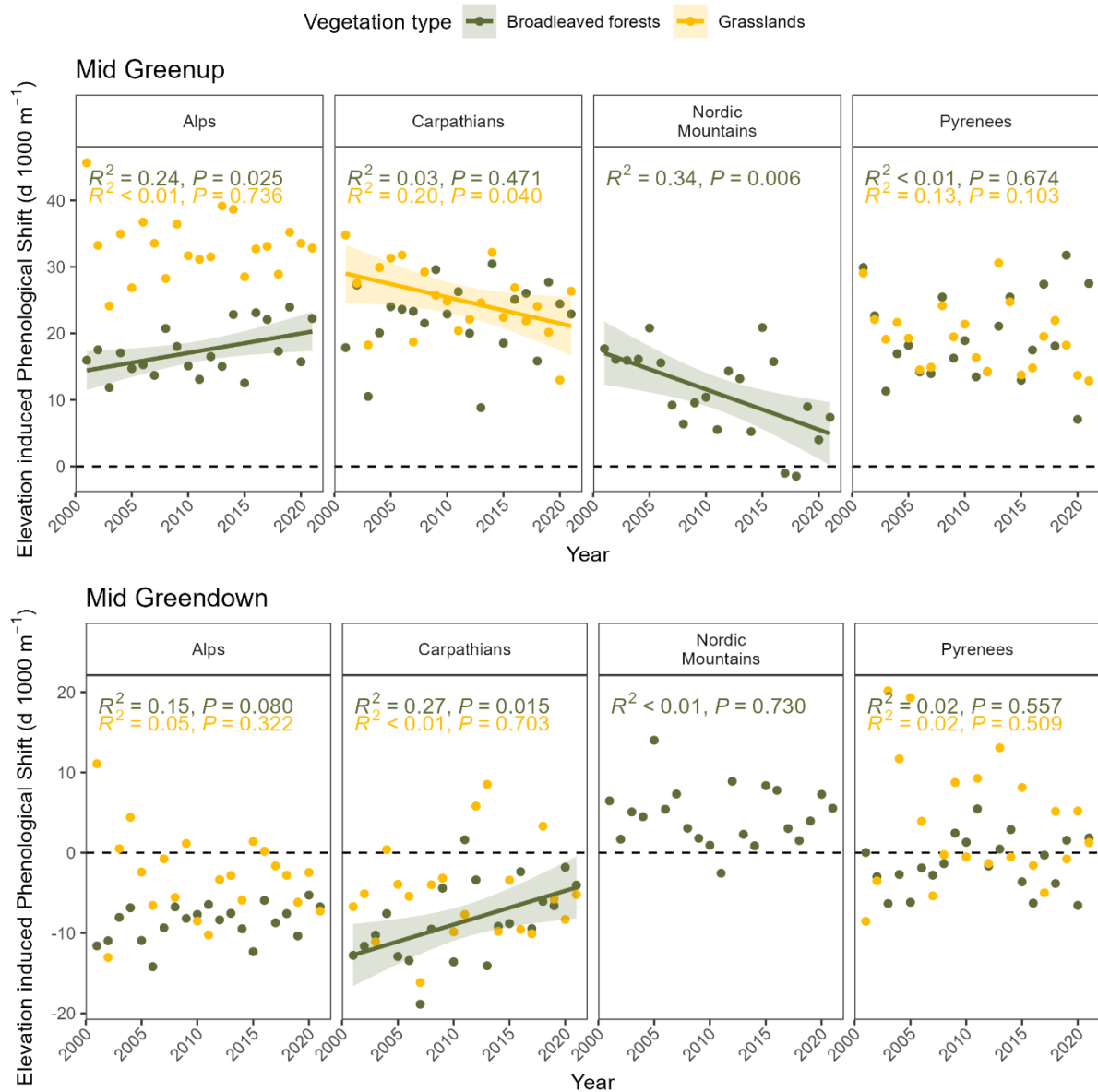
Fig. S7. Changes of the spring (upper panel) and autumn (lower panel) Elevation-induced Phenological Shift (EPS) for broadleaves forests and natural grasslands during 2001–2021 in the Alps, Carpathians, Nordic Mountains, and Pyrenees. R^2 and p-values of linear models are reported. Regression line and 95% confidence level interval of significant trends are displayed.
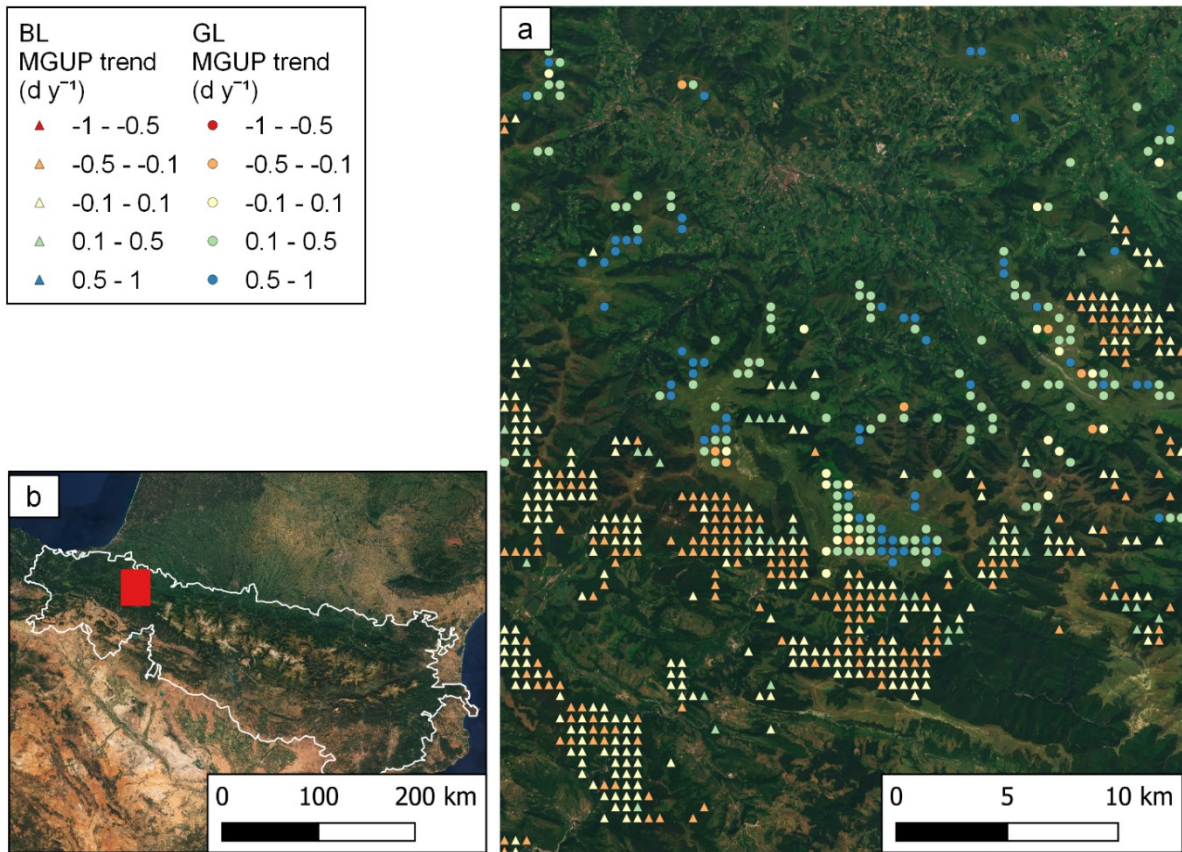
Fig. S8. Diverging Mid Greenup (MGUP) trend in the Pyrenean broadleaved forests (BL) and natural grasslands (GL) at low elevations(mean annual temperature between 9°C and 11°C). Panel a: detail of spatial distribution map of the MGUP trend. Panel b: locator map showing the whole Pyrenees (white line) and the extent of the map shown in panel a (red rectangle). The background image is a cloudless 2017 composite of Sentinel-2 images.
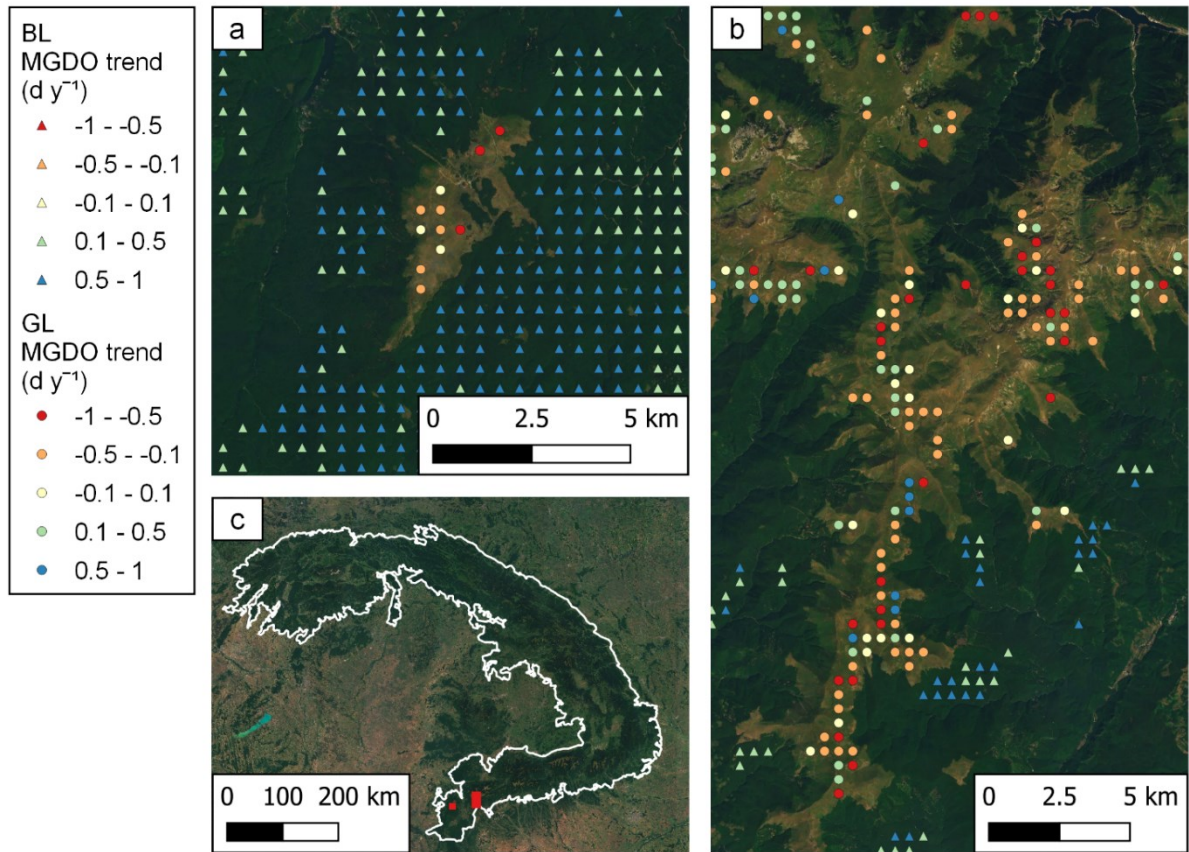
Fig. S9. Diverging Mid Greendown (MGDO) trend in the Carpathian broadleaved forests (BL) and natural grasslands (GL) at mid elevations (mean annual temperature between 4°C and 7°C). Panel a and b: details of the spatial distribution of the MGDO trend. Panel c: locator map showing the whole Carpathians (white line) and the extents of the maps shown in panel a and b (red rectangles). The background image is a cloudless 2017 composite of Sentinel-2 images.

Diverging trends in plant phenology across European mountains in a warming world
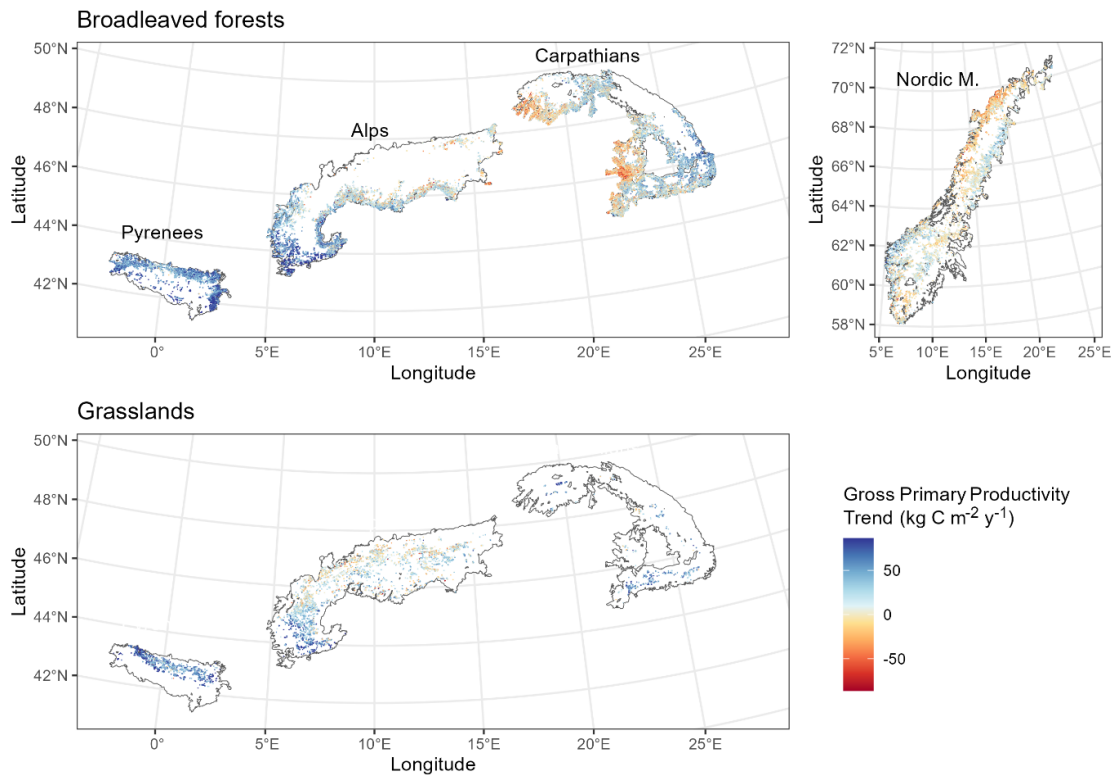Andreatta et al. (2024), *unpublished*

Fig. S10. Spatial distribution of trends in Gross Primary Productivity in broadleaved forests and natural grasslands during 2001-2021 in the Alps, in the Carpathians, in the Nordic Mountains, and in the Pyrenees. Trends were estimated using the Theil-Sen estimator.

Supplementary table

Tab S1. Regression table of mixed effect models separately defined for each phenometric, vegetation type (GL= natural grasslands, BL= broadleaved forests) and region. The phenometric was defined as a response variable, Year, Mean Annual Temperature (MAT) and their interaction as fixed effect, and pixel ID as a random intercept effect. The fourth column reports the models' conditional R^2; columns from five to seven report the coefficient estimates, columns from eight to ten report coefficient p-values.

Phen.	Veg	Reg	Cond. R^2	Estimates			p-value		
				Year	MAT	Year*MAT	Year	MAT	Year*MAT
MGUP	GL	Alps	0.59	-0.102	-4.786	0.012	<0.001	<0.001	<0.001
		Carpathians	0.62	-0.568	-6.671	0.075	<0.001	<0.001	<0.001
		Pyrenees	0.60	-0.497	-4.433	0.057	<0.001	<0.001	<0.001
	BL	Alps	0.57	0.284	-1.652	-0.040	<0.001	<0.001	<0.001
		Carpathians	0.58	0.178	-3.752	-0.028	<0.001	<0.001	<0.001
		Nordic M.	0.51	0.024	-4.150	-0.002	<0.001	<0.001	0.067
		Pyrenees	0.65	0.031	-2.722	-0.012	0.013	<0.001	<0.001
MGDO	GL	Alps	0.30	0.326	-0.097	0.008	<0.001	0.047	<0.001
		Carpathians	0.14	0.021	1.640	-0.033	0.563	<0.001	<0.001
		Pyrenees	0.30	0.036	-1.495	0.047	0.316	<0.001	<0.001
	BL	Alps	0.61	0.500	1.596	-0.027	<0.001	<0.001	<0.001
		Carpathians	0.42	0.909	2.172	-0.078	<0.001	<0.001	<0.001
		Nordic M.	0.43	0.088	0.994	-0.005	<0.001	<0.001	<0.001
		Pyrenees	0.48	0.212	0.500	-0.002	<0.001	<0.001	0.298

Diverging trends in plant phenology across European mountains in a warming world
Andreatta et al. (2024), *unpublished*